Research supported by the
National Science Foundation
under Grants ATM-9313716 and ATM-9422499.

THE FINE-SCALE CHARACTERISTICS OF THE 7-8 MAY 1995 SQUALL LINE AS REVEALED BY ELDORA

by

J. Adam Kankiewicz

Richard H. Johnson, PI

Colorado State University

DEPARTMENT OF ATMOSPHERIC SCIENCE

PAPER NO. 657

THE FINE-SCALE CHARACTERISTICS OF THE 7-8 MAY 1995 SQUALL LINE AS REVEALED BY ELDORA

by

J. Adam Kankiewicz

Department of Atmospheric Science
Colorado State University
Fort Collins, CO 80523

Summer 1998

Atmospheric Science Paper No. 657

ABSTRACT

THE FINE-SCALE CHARACTERISTICS OF THE 7–8 MAY 1995 SQUALL LINE AS REVEALED BY ELDORA

During the VORTEX-95 campaign, the *Electra* Doppler Radar (ELDORA) passed through the transition zone of a maturing squall line that formed over the Southern Plains late on 7 May 1995. A leading line of convection, a transition zone, and a developing trailing stratiform region of precipitation composed the precipitation structure of this squall line. Descending rear-to-front flow and ascending front-to-rear flow predominated in the line-perpendicular flow. In the line-parallel direction, there was strong southerly along-line flow advecting hydrometeors to the north end of the line. An along-line average of reduced-resolution data revealed a rearward tilted updraft within the convective line, behind which lay a secondary band containing a mesoscale updraft/downdraft couplet.

The fine-scale observations made by ELDORA have provided new insight into the inner structure of maturing linear squall lines. Horizontal flow was highly variable within the convective line, with strong evidence of acceleration of the mean flow (e.g., Bernoulli flow) around updraft cores. Flow rearward of the convective line was much less perturbed. Within the stratiform region, an along-line jet was observed near the 0°C level, possibly arising from a melting-induced stable layer.

In contrast to the coarse-resolution analysis, high-resolution data showed updrafts within the convective line to be erect with peak updraft velocities centered at increasing elevations behind the leading edge of the line. Also, these data showed the stratiform region to be comprised of many small-scale updrafts and downdrafts at all levels. Thus, the appearance of a tilted updraft signature in the convective line and a broad mesoscale updraft/downdraft couplet through the stratiform region arises from spatial filtering.

Further analysis of the vertical velocity field within this squall line revealed evidence for high-frequency gravity wave oscillations. General characteristics of these thermally-forced gravity waves included wavelengths of 5–10 km and amplitudes of 2–5 m s^{-1}. Additional evidence for these gravity waves came by the observed quadrature relationship between the vertical motion field and perturbations in the line-perpendicular flow. Though hinted at in previous studies, this study offers the first observational confirmation of gravity wave existence within the stratiform region of a squall line as predicted by recent two-dimensional modeling studies. The three-dimensional behavior of these waves is consistent with recent modeling studies of elevated heat sources in a sheared environment.

Contoured Frequency by Altitude Diagram (CFAD) analyses of the kinematic and precipitation fields confirmed this squall line was in the early stages of its existence. Additionally, mass-weighted CFADs confirmed that upward mass transport was dominated by moderate to strong updrafts (in contrast to recent draft statistics presented for Florida convection). Substantial mid-level downward mass transport was also noted, indicating that significant subsidence occurred close to the leading line of convection.

Joseph Adam Kankiewicz
Department of Atmospheric Science
Colorado State University
Fort Collins, Colorado 80523-1371
Summer 1998

ACKNOWLEDGEMENTS

I would like to thank my advisor, Dr. Richard H. Johnson for providing helpful guidance and advice on this research and Dr. Roger M. Wakimoto for providing the ELDORA data that made this research possible. I would like to thank the rest of my thesis committee, Dr. Steve Rutledge and Dr. Jorge Ramirez for their time and input.

The completion of this work would not have been possible without the support of many people. In particular, I want to thank Dr. Ching-Huang Liu for his enthusiastic responses to my many questions about the processing and interpretation of the ELDORA data. Dr. Rob Fovell provided many insightful comments and thoughtful discussions on the inner workings of a squall line from a modeling perspective. Paul Ciesielski, and Rick Taft provided countless hours of computer help. Jason Nachamkin, Jason Knievel, Dr. Pat Haertel, Matt Parker, and many others provided helpful comments towards this research.

This research has been supported by the National Science Foundation under Grants No. ATM-9313716 and No. ATM-9422499.

DEDICATION

To Mom, Dad, Chris, Cindy, Ben, Dave and Tommy.

Thanks for always being there.

CONTENTS

LIST OF FIGURES

LIST OF TABLES

Chapter 1

BACKGROUND AND MOTIVATION FOR RESEARCH

1.1 Background

1.1.1 Mesoscale convective systems

Zipser (1982) proposed the term "mesoscale convective system" (MCS) to refer to all organized precipitation systems on scales from 20 to 500 km that include vigorous convection during some part of their life-cycles. As one can imagine, Zipser's definition encompasses many different types of weather phenomena. One of the most commonly studied type of MCS is that with convective cells oriented linearly: the squall line. A squall line comprises a narrow line of deep convective cells that are often trailed by a much broader region of stratiform rain (e.g., Newton 1950; Fujita 1955; Pedgley 1962; Houze 1977; Houze et al. 1989; Biggerstaff and Houze 1991a).

A typical line-normal structure of a squall line is shown in Fig. 1.1. Three distinct precipitation regions are commonly observed in mature squall lines: the leading-line convection, the transition zone, and the trailing stratiform region. Two features generally dominate the mesoscale kinematic structure of an organized MCS: the ascending front-to-rear (FTR) flow, and the descending rear-to-front (RTF) flow. Although squall lines form in many shapes and sizes (e.g., Houze et al. 1990), two formations are typical: symmetric (Fig. 1.2a) and asymmetric (Fig. 1.2b). Loehrer and Johnson (1995) observed that these structures may not be distinct classifications, but separate stages of the evolution of some squall lines.

The leading-line convection associated with a mature squall line is typically characterized by a multicell thunderstorm regime. The formation of these cells is a discrete process that has been the focus of many modeling studies (e.g., Thorpe et al. 1982; Fovell and

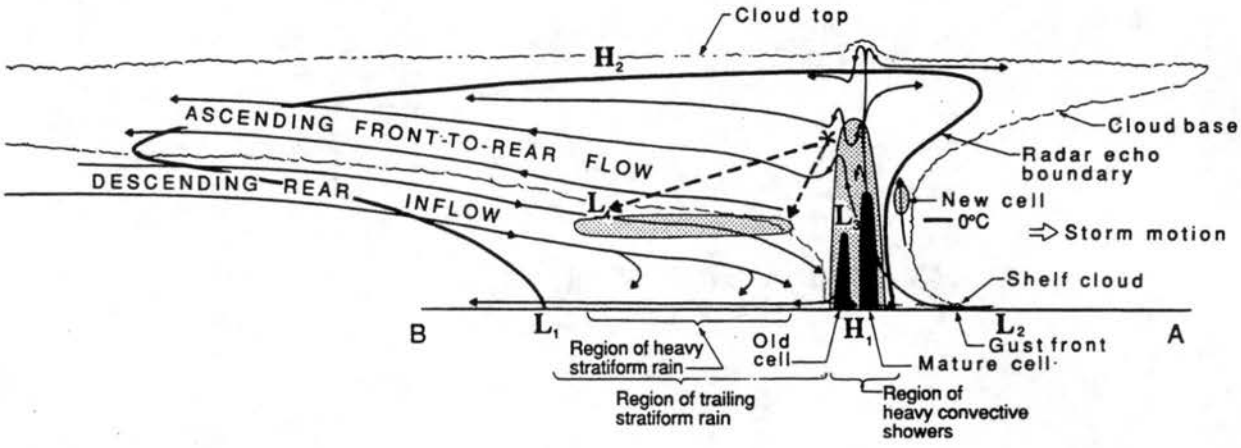

Figure 1.1: Conceptual model of a squall line with a trailing stratiform area viewed in a vertical cross section oriented perpendicular to the convective line (i.e. parallel to its motion) (from Houze et al. 1989).

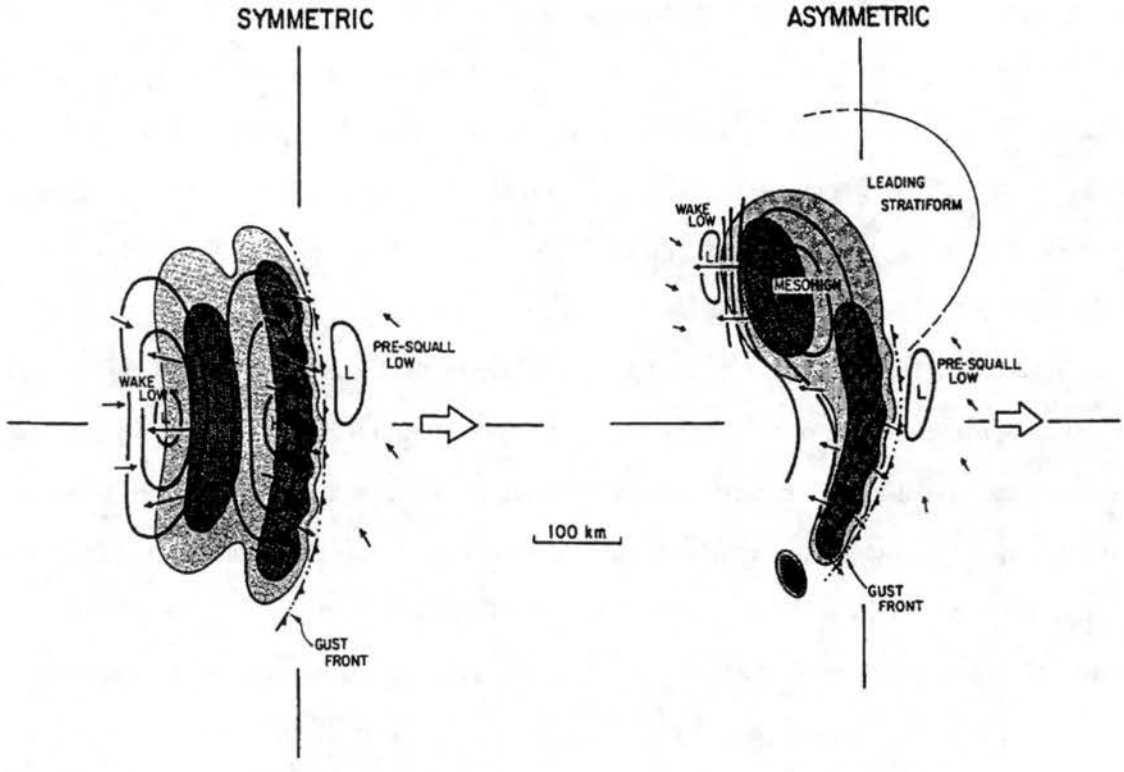

Figure 1.2: Conceptual model of the surface pressure, kinematic, and precipitation fields associated with the (a) symmetric and (b) asymmetric stages of the MCS life cycle. Radar reflectivity is adapted from Houze et al. (1990). Levels of shading denote increasing radar reflectivity; the darkest shading corresponds to convective cores. Pressure is in 1-mb increments. Small arrows represent the surface flow and large arrows represent storm motion (from Loehrer and Johnson 1995).

Ogura 1988; Rotunno et al. 1988; Yang and Houze 1995; Fovell and Tan 1998). New convective cells are generated with a period of $\sim$ 10–20 minutes above or near the quasi-steadily forced updraft associated with the leading edge of the gust front. As these newly formed cells mature, they are advected rearward relative to the gust front. In maturity, they produce intense precipitation, high vertical velocities, and high radar reflectivities. In time, these cells dissipate and eventually blend in with the trailing anvil associated with these squall lines.

Often observed to the rear of the leading-line convection is the transition zone (e.g., Ligda 1956; Smull and Houze 1985; Braun and Houze 1994), which is generally manifested as an area of weak reflectivity aloft and light precipitation at the surface. Many studies have documented deep regions of mesoscale descent coincident with the transition zone (Houze and Rappaport 1984; Srivastava at al. 1986; Smull and Houze 1987a; Roux 1988; Rutledge et al. 1988; Biggerstaff at al. 1991a,1993). Fallspeed sorting of ice particles generated by the leading-line convection is partially responsible for the formation of the transition zone. The heavier ice particles are detrained rapidly near the leading-line convection, while lighter ice particles are advected rearward by the FTR flow (e.g., Rutledge and Houze 1987; Smull and Houze 1987a). Biggerstaff and Houze (1993) showed that the mesoscale downdraft seemed to comprise two distinct parts: an upper level downdraft that appeared to be mechanically forced (partially by gravity waves near the tropopause and by subsidence from the leading-line convection) and a lower level downdraft that appeared to be microphysically forced (through sublimation, melting, and evaporation). Most likely, both of these mechanisms act in tandem to produce, and maintain, a squall line's transition zone.

Behind the transition zone is a region of enhanced precipitation at the surface often referred to as the trailing stratiform region. For the rest of this study the term "secondary band" will be used to describe the region of enhanced precipitation associated with the trailing stratiform region of a squall line.

Bands of enhanced surface precipitation are often located beneath radar "bright bands" (e.g., Austin and Bemis 1950; Battan 1973). As aggregates descend through the 0°C isotherm, melting rapidly coats aggregates with water that, along with increased aggregation

of these wet ice particles, produces the enhanced radar signature called a bright band. To generate the rates of precipitation observed within secondary bands, both ice particle advection and enhanced depositional growth within a mesoscale updraft are necessary (Rutledge and Houze 1987).

The vertical motion profile in the secondary band is fundamentally different from those in both the leading-line convection and the transition zone. Within a mature secondary band, broad mesoscale ascent lies within the middle and upper troposphere, while a region of unsaturated mesoscale descent is present in the lower troposphere (e.g., Zipser 1969,1977; Ogura and Liou 1980). Biggerstaff and Houze (1993) documented that the mesoscale downdraft is areally smaller than the mesoscale updraft and is largely determined by the precipitation associated with the secondary band.

Previous Doppler radar studies, however, have suggested that the vertical motion field within a trailing secondary band of precipitation may not be as homogeneous as a mesoscale updraft/downdraft concept may imply. Srivastava et al. (1986) observed significant horizontal variations in the vertical velocity within a trailing anvil. Rutledge et al. (1988) and Rutledge and MacGorman (1988) documented vertical motion variability within the the secondary band of the 10–11 June 1985 squall line. In the same 10-11 June squall line, multiple maxima in updrafts and downdrafts were observed by Matejka and Schuur (1991), and the peak in updrafts was located near the leading edge of the secondary band.

Yuter and Houze (1995b) used high resolution dual-Doppler radar data to document that the mesoscale updraft/downdraft couplet associated with the decaying secondary band of a Florida cumulonimbi ensemble actually comprised of many individual updrafts and downdrafts located at all levels of the secondary band. Volume averaging was necessary to reveal the typical mesoscale updraft/downdraft couplet.

On the larger scale, Ooyama (1971) showed that to properly assess the vertical profile of convective heating within the atmosphere, knowledge of vertical mass transport in convective systems is needed. Much research has gone into measuring vertical mass fluxes, and emphasis has been placed on obtaining net fluxes within convective systems (e.g., Heymsfield and Schotz 1985; Raymond et al. 1990). Yuter and Houze (1995c) showed that

vertical mass transport throughout the life of a Florida cumulonimbi ensemble predominately occurred via weak and moderate upward and downward velocities (approximately $-5 \text{ m s}^{-1} < w < 5 \text{ m s}^{-1}$).

1.1.2 Gravity waves and MCSs

Recent squall line modeling studies have shown that gravity waves generated by leading-line convection play an intricate roll in the formation and structure of a squall line. Figure 1.3 shows a squall line simulation from Alexander et al. (1995) and highlights the plethora of gravity waves generated by the leading line of convection. Within the stratosphere, vertically propagating gravity waves have been observed (Larsen et al. 1982; Sato 1993; Pfister et al. 1986, 1993). Gravity wave drag within the stratosphere has been shown to affect atmospheric simulations within general circulation models (GCMs) and weather forecasting models (e.g., Palmer et al. 1986; McFarlane 1987; Rind et al. 1988) and may even contribute to the forcing of the quasi-biennial oscillation (Takahashi and Bolville 1992).

In the troposphere, one observes the generation of gravity waves within the squall line simulation of Alexander et al. (Fig. 1.3). In the convective region of a squall line, buoyancy acts primarily as a destabilizing force. In the stratiform region, however, the role of buoyancy is switched to that of a restoring force, which allows the propagation of gravity waves generated by the latent heat absorption and release within the convective region of a squall line (Pandya and Durran 1996).

Several two-dimensional modeling studies have addressed the identification and interpretation of the effects of low-frequency gravity waves on the internal structures of squall lines (Schmidt and Cotton 1990; Cram et al. 1992; Mapes 1993). Pandya and Durran (1996) used a modeling study to suggest that the perturbations that form within a squall line (FTR, RTF flows and mesoscale ascent/descent) are a response to the gravity wave forcing tied to the low-frequency components of the latent heating and cooling associated with leading-line convection. Nachamkin (1998) tackled the issue of gravity wave/squall line interaction from a three-dimensional perspective and identified crucial low-frequency

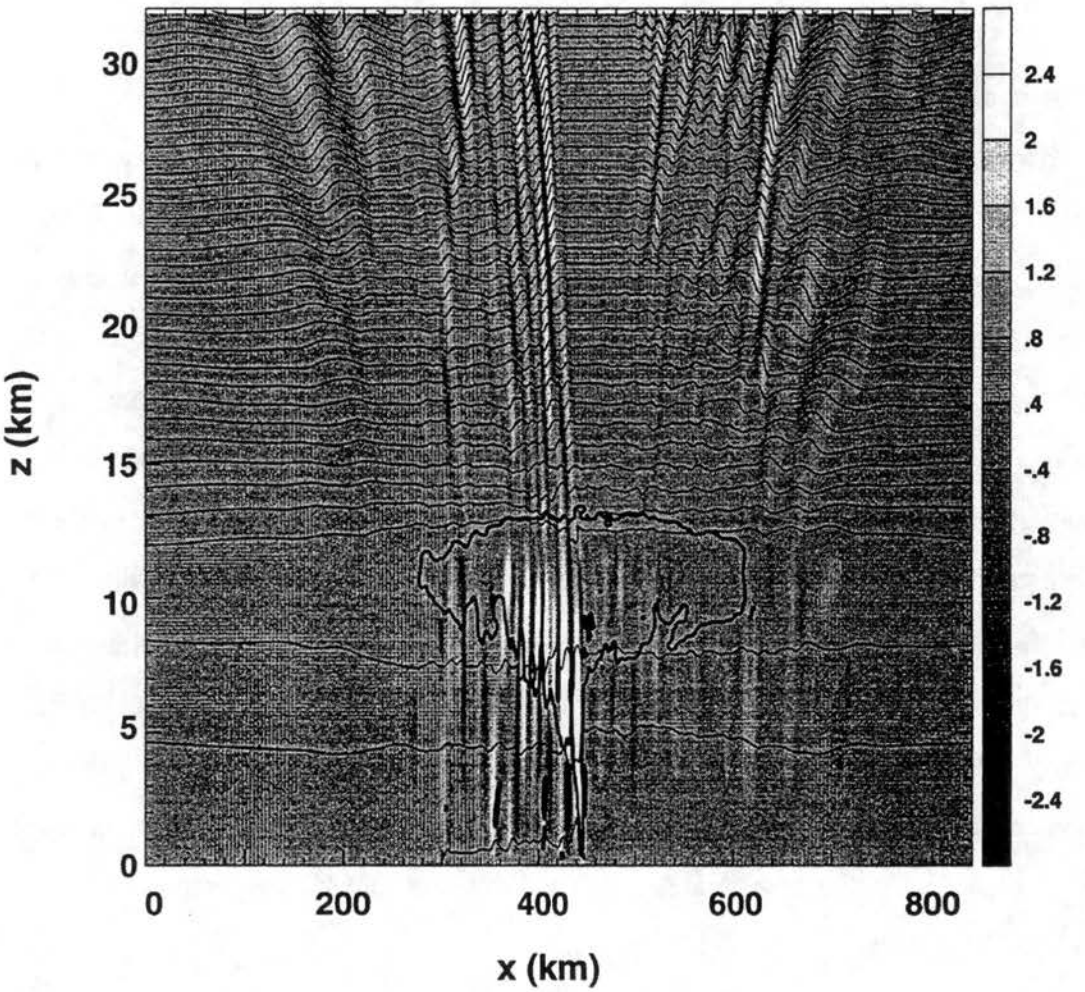

Figure 1.3: A squall line simulation at $t = 4$ hours. Shading represents contours of vertical velocity. Thin lines are isentropes (at 15-K intervals), and the thick line shows the cloud outline (cloud water mixing ratio $= 1 \times 10^{-4}$ g g^{-1}). The tropopause is at 12–13 km (from Alexander et al. 1995).

gravity wave modes that were associated with the formation and maintenance of an eastern Colorado MCS.

The occurrence of high-frequency gravity waves has been noted within squall line simulations (e.g., Pandya and Durran; Fovell and Tan 1998). Yang and Houze (1995a) suggest that the multi-cell generation mechanism exhibited by leading-line convection can be physically interpreted by means of the gravity waves generated by convection. Recent dual-Doppler studies (Smull and Houze 1987b; Keenan and Rutledge 1993; Bluestein et al. 1993) have hinted at the possibility of high-frequency gravity wave oscillations occurring within squall lines.

1.2 Research goals

Previous dual-Doppler observations of linear squall lines have been mostly limited to the mature and decaying phases of their life-cycles (e.g., Smull and Houze 1987; Biggerstaff and Houze 1991a; Schuur et al. 1991).

During the 1995 field phase of VORTEX (Verification of the Origins of Rotations in Tornadoes Experiment), the NCAR *ELectra* DOppler RAdar (ELDORA) happened to fly both in front of and along the transition zone of a maturing linear squall line on 8 May 1995, and it recorded high spatial resolution dual-Doppler data over a substantial portion of the system.

This study will focus on the fine-scale structure of a newly formed secondary band trailing a vigorous region of leading-line convection. Emphasis will be placed on the precipitation and kinematic structures inherent to this squall line. For the first time, observational evidence for high-frequency gravity wave oscillations within the secondary band of a squall line has been obtained from a Doppler radar having sufficient horizontal resolution to unambiguously determine their properties. These findings are a primary focus of this study. In addition, the vertical mass transport within the convective line and secondary band will be examined to provide further insight into precipitation processes.

Sources of data and methods of analysis are presented in Chapter 2, then an overview of the 7–8 May squall line is the focus of Chapter 3. Horizontal, vertical, and composite

cross sections will be used to interpret the high-resolution ELDORA data in Chapter 4. In Chapter 5, statistical methods of analysis will be applied to the convective-line and secondary band volumes to reveal their precipitation, kinematic, and vertical mass flux characteristics.

Chapter 2

DATA AND METHODS OF ANALYSIS

Figure 2.1: The *Electra* in flight. The ELDORA can be seen aft of the tail.

2.1 ELDORA

Unlike ground based Doppler radars, which are fixed and must wait for meteorological phenomena to move within scanning distance of them, airborne Doppler platforms offer the ability to observe and document transient meteorological phenomena over extended periods of time. To further our knowledge of convective phenomena, the National Center for Atmospheric Research (NCAR) and the Centre de Recherche en Physique de l'Environment Terrestre et Planetaire (CRPE) in Paris, France collaborated to develop a unique airborne Doppler radar platform. The result of this collaboration is the *Electra* DOppler RAdar (ELDORA) (Fig. 2.1).

ELDORA consists of two X-band ($\sim$ 3.15 cm wavelength) radars that provide continuous sampling along the flight track. One antenna points $\sim$18.5° forward of a plane normal to the aircraft axis, and the other antenna points $\sim$18.5° aft (Fig. 2.2a). This scan pattern allows for collection of fore- and aft-pointing Doppler data while the aircraft flies

in a straight line, thus enabling calculation of two-dimensional wind fields within the storm volume (Fig. 2.2b). For further information on the technical nature of ELDORA refer to Hildebrand et al. (1994, 1996). Radar parameters used by ELDORA for collection of these data are shown in Table 1.

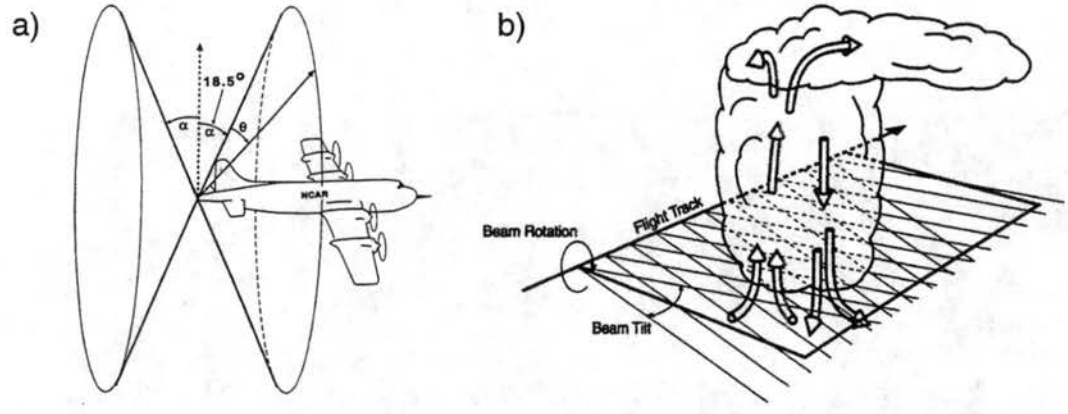

Figure 2.2: ELDORA scanning and sampling techniques. (a) Scan technique showing the dual radar beams, tilted fore and aft of the plane normal to the fuselage. The antennas and radome rotate as a unit about on axis parallel to the longitudinal axis of the aircraft. (b) The flight track past a hypothetical storm is shown. Data taken from the fore and aft beams to form an analysis of the velocity and radar reflectivity on planes through the storm. The radial velocities at beam intersections are used to derive the two-dimensional wind field on the analysis plane (from Hildebrand et al. 1996).

Table 2.1: ELDORA convective scanning Mode

Antenna rotation rate (deg s^{-1})	133
Number of samples (per frequency)	24
PRF (Hz)	2500/2000
Number of range gates	385
Gate length (m)	150
Sweep angle resolution (deg)	1.44
Along track resolution (m)	324
Maximum range (km)	60
Individual unambiguous velocities ($\pm$m s^{-1})	19.7/15.7
Maximum unambiguous velocities ($\pm$m s^{-1})	78.7

ELDORA was flown for the first time during TOGA-COARE (Tropical Ocean Global Atmosphere Coupled Ocean-Atmosphere Response Experiment; Webster and Lukas 1992)

and then again in 1995 during VORTEX (Rasmussen et al. 1994), from which the data for this research originate.

2.2 Data

2.2.1 ELDORA Data

The reflectivity and Doppler velocity data used in this study were edited with the NCAR RDSS (Oye and Carbone 1981) and SOLO (Oye et al. 1995) software packages to remove ground clutter and second-trip echo contamination. Using a Cressman filter (Cressman 1959), the edited data were then interpolated onto a Cartesian grid with horizontal and vertical grid spacing of 400 and 500 m, respectively. This grid was chosen to be consistent with the ELDORA parameters shown in Table 1. Well-bounded holes present in the horizontal wind fields were patched, and the data were then synthesized using CEDRIC (Custom Editing and Display of Reduced Information in Cartesian space; Mohr et al. 1986).

The determination of a hydrometeor fallspeed/reflectivity relationship (Z-v_t) was based on the work of Joss and Waldvogel (1970) with a correction included for the effects of air density (Foote and du Toit 1969). This method provides a reasonable relationship between the fallspeeds of ice and water. Several sensitivity tests were run on the Z-v_t relationship using other formulations (e.g., Biggerstaff and Houze 1991a) and very minor changes in the vertical motion field were noticed and did not change the conclusions.

Because of concerns that the motions of the aircraft could contaminate the Doppler data, a three-step Leise filter (Leise 1982) was applied to the Doppler velocity data. This significantly damped the signal of wavelengths up to 4.8 km and removed those wavelengths below 3.2 km.

Vertical velocities were then derived from the anelastic continuity equation applied to the divergence field. The variational technique in the vertical integration scheme was used here. This method iteratively calculates a solution that minimizes the error in a vertical column in the grid. Lower and upper level boundary conditions were set to zero. The emphasis of this study will be on regions closer than 50 km to the radar where the radar

coverage is excellent. Several tests were also run using different upper boundary conditions with the results being virtually identical to those presented in this paper.

The variationally adjusted vertical motion field was then used to re-derive the horizontal wind field that minimized the mean difference between the horizontal and vertical convergence within each level. This "corrected" horizontal wind field was then used in the final analysis.

Storm motion for this squall line was determined from isochrone analysis of the leading line convection (e.g., Gamache and Houze 1982; Biggerstaff and Houze 1991a) from 0000 UTC to 0200 UTC 8 May 1995. An average motion of 12.2 m s^{-1} from a direction of 300° was computed and then removed from the horizontal dual-Doppler derived wind field to yield storm-relative winds. A rotation of 30° east of north was applied to the data to give a system-relative reference frame (for viewing purposes).

All ELDORA data used in this study have an applied time-space advection of 17.3 m s^{-1} from 190°, which corresponds to the observed convective cells' motions. Data from the transition zone passage was advected to a central time of 0100 UTC.

2.2.2 Surface Data

Oklahoma Mesonetwork data (Brock et al. 1995) are used to document the evolution of the squall line as it progressed through Oklahoma. Both time series and surface composites of mesonetwork data are used in this paper to help document the squall line.

2.2.3 Rawinsonde Data

Rawinsonde data are used from two sites: Purcell, OK (PUR) and Oklahoma City, OK (OUN). Rawinsondes were released at 2346 UTC 7 May (PUR) and 2304 UTC 7 May (OUN), ahead of the squall line in both cases. No sondes were released in, or behind this squall line from either of these two sites.

2.2.4 Profiler Data

NOAA Wind Profiler Demonstration Network (WPDN) 404-MHz (Ralph et al. 1995) data from Purcell, OK are used in this study to provide additional insight into the vertical structure of the wind during the squall line passage through the region.

2.2.5 NEXRAD Data

National Weather service radar data used in this paper are from the WSR-88D radars (Crum et al. 1993) at Ft. Worth, TX (KFWS), Frederick, OK (KFDR), Oklahoma City, OK (KTLX), and Amarillo, TX (KAMA). These radars operate at a 10 cm wavelength with a 0.95° beamwidth and 1 km and 0.25 km gate lengths for reflectivity and velocity, respectively. Level II data (all raw products) were archived at KFWS, KAMA, and KTLX, while only Level IV (derived products) were archived at KFDR.

Composite NEXRAD regional radar images (processed by Kavouras, Inc.) are used to document the evolution of the 7–8 May 1995 squall line before, during, and after the *Electra* fly-by. These images are composites from the individual 0.5° NEXRAD reflectivity base scans and use the strongest reflectivity values for a given grid point. The horizontal resolution of these images is 2×2 km.

VAD (Velocity-Azimuth Display) (Browning and Wexler 1968) wind profiles are presented from KFDR WSR-88D. The radius of the VAD cylinder used here is 29.2 km.

2.2.6 Lightning data

Cloud-to-ground lightning data are from the National Lightning Detection Network [NLDN; see Orville et al. (1987) for a description of the network], and are used to document the evolution of the squall line.

2.2.7 Satellite Data

Satellite imagery used in this paper are from the Geostationary Operational Environmental Satellite, GOES-8. Channel 1 – visible wavelength (0.52 to 0.72 μm at a 0.57×1.00 km sub-point resolution) imagery is used to document the initiation and early evolution of the squall line.

Chapter 3

ENVIRONMENTAL AND SQUALL LINE OVERVIEW

3.1 Synoptic conditions on 7-8 May 1995

The synoptic environment was dominated by a deep upper-tropospheric low centered to the west of the Rocky Mountains at 0000 UTC 8 May 1995 as shown by the 300-mb analysis (Fig. 3.1). An upper-tropospheric jet streak was rotating around this low; the streak's left exit region was located near northern Texas and western Oklahoma. Upper-level diffluence over the Southern Plains provided an environment favorable for the large scale convection that was occurring at the time.

At 500-mb (Fig. 3.2) dry southwesterly flow was present over north central Texas and central Oklahoma, while at 850-mb (Fig. 3.3), a tongue of relatively warm, moist air was being advected northward through eastern Texas and Oklahoma ahead of the frontal trough. This combination provided additional support for deep convection. Weak cold air advection behind the frontal trough can be seen over New Mexico.

At the surface (Fig. 3.4) NCEP (National Centers for Environmental Prediction) had analyzed a surface cold front across the panhandle of Texas. However, a surface dryline may be a more appropriate characterization of this surface convergence zone. Dry southwesterly flow was present to the west of this dryline, while strong southerly and southeasterly flow from the Gulf of Mexico lay to the east. Surface dewpoints were near 70°F with dry-bulb temperatures in the upper 70s (°F) in the region ahead of the squall line. The squall line was noted by NCEP over western Oklahoma and had an orientation of south-southwest to north-northeast through southwestern Oklahoma.

The Oklahoma pre-squall thermodynamic structure is documented by the 0000 UTC 8 May 1995 soundings from Oklahoma City (OUN) and Purcell (PUR) (located over south-

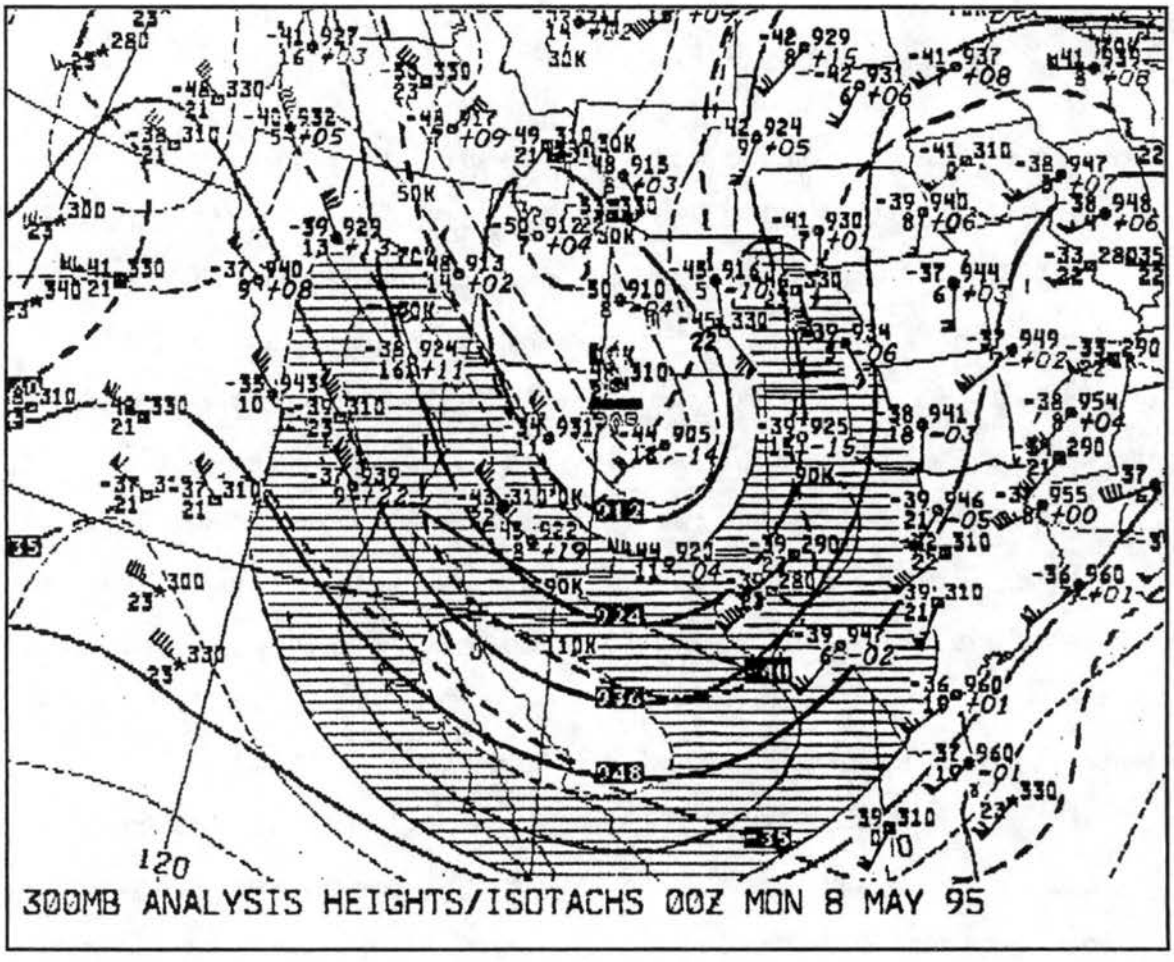

Figure 3.1: 0000 UTC 8 May 1995 NCEP 300-mb analysis

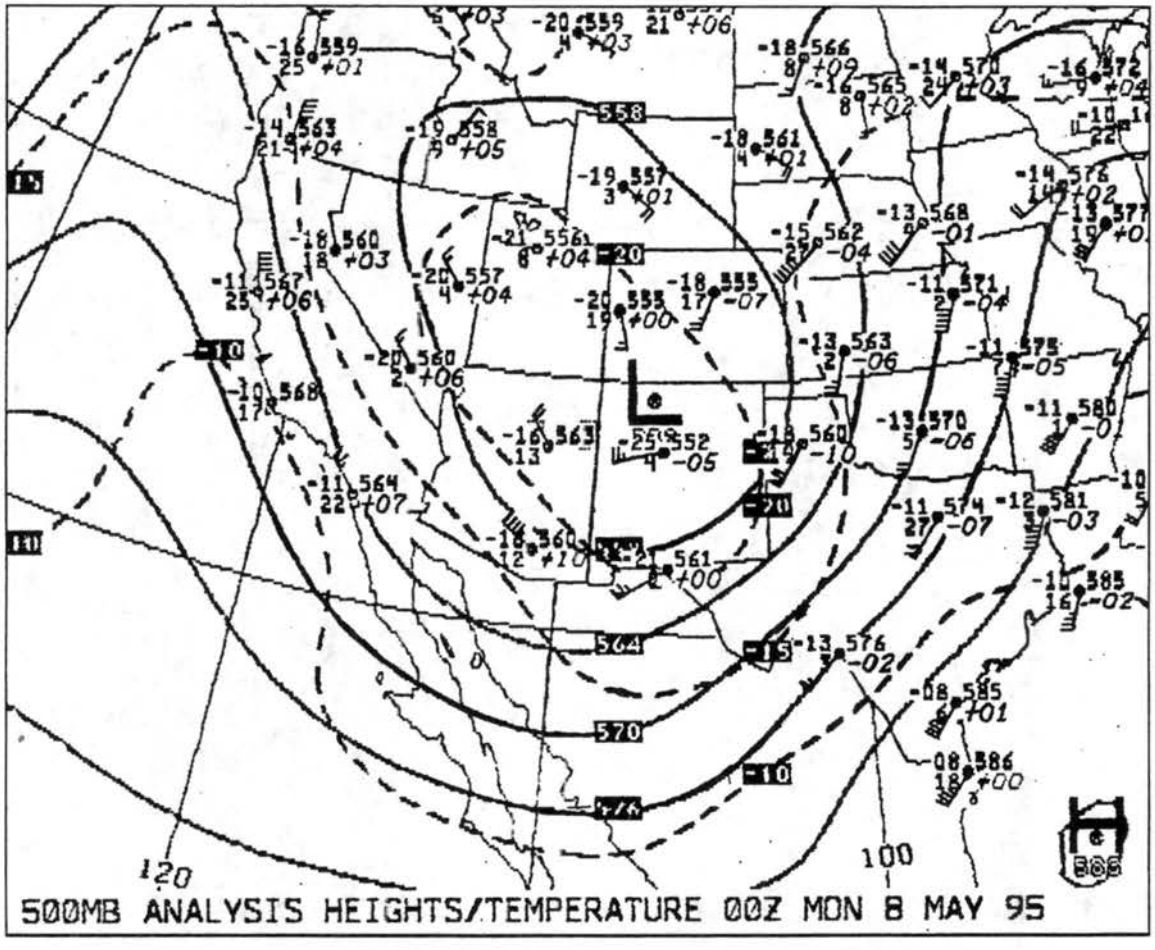

Figure 3.2: 0000 UTC 8 May 1995 NCEP 500-mb analysis

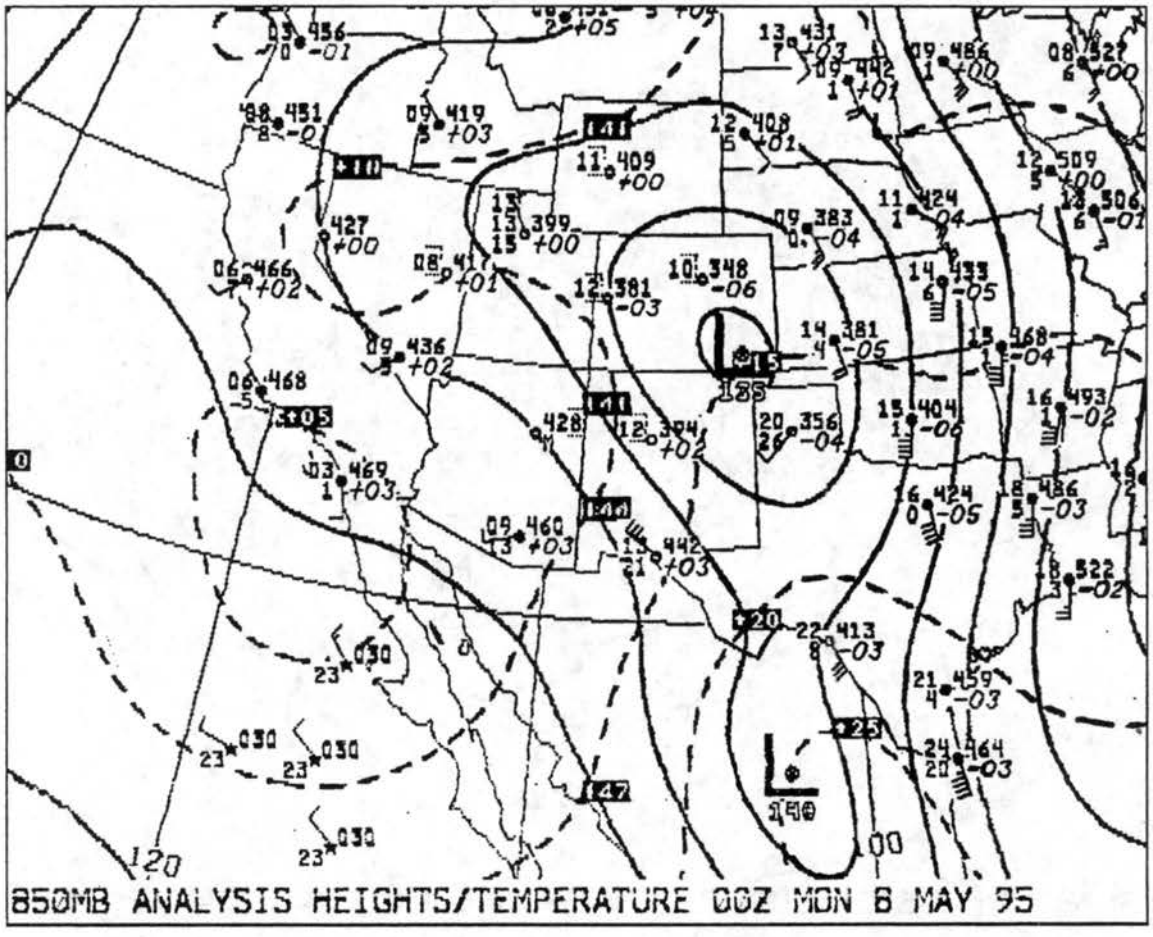

Figure 3.3: 0000 UTC 8 May 1995 NCEP 850-mb analysis

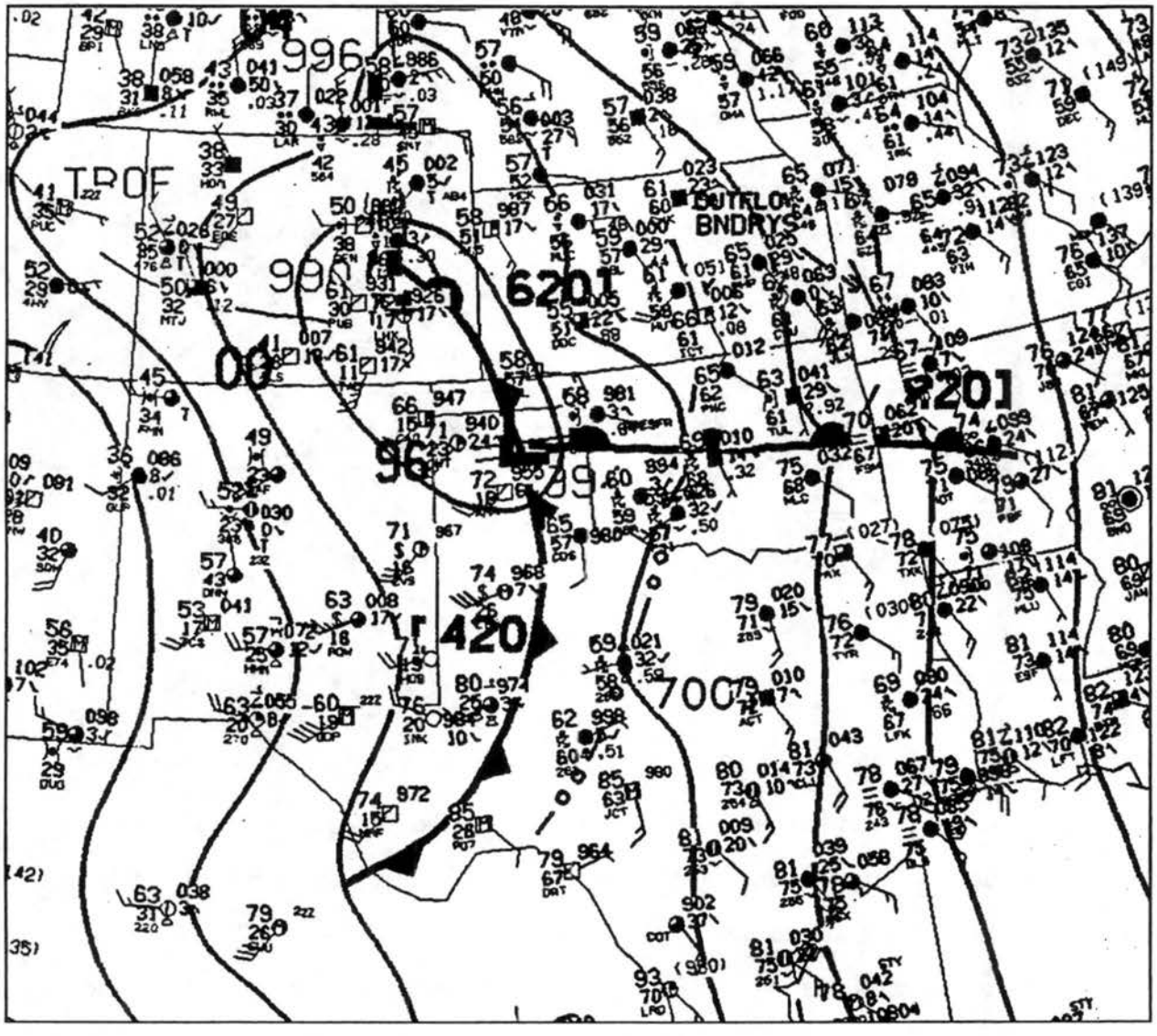

Figure 3.4: 0000 UTC 8 May 1995 NCEP surface analysis

central Oklahoma) shown in Fig. 3.5. Air was moist below 700-mb and dry above 500-mb in both soundings. Convective available potential energy (CAPE) ranged from ~1500 (OUN) to ~1700 (PUR) $m^2\ s^{-2}$. Strong line-perpendicular shear was observed through the lowest levels, while substantial line-parallel shear occurred aloft.

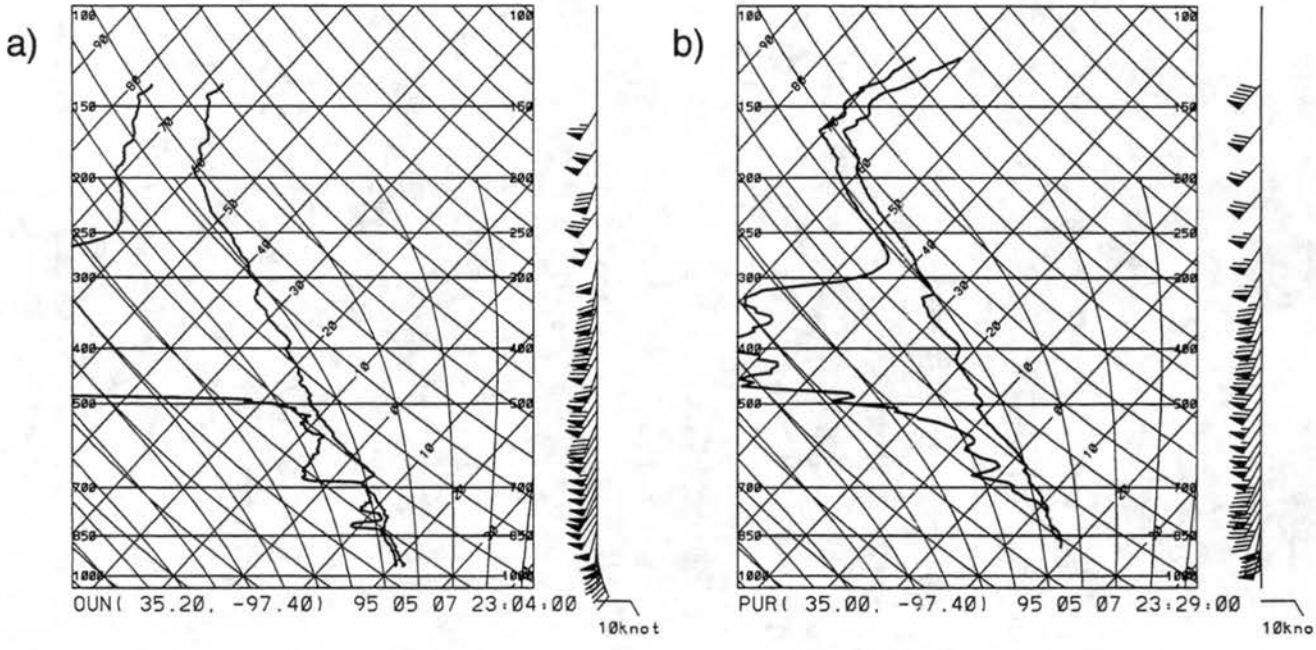

Figure 3.5: 0000 UTC (a) Oklahoma City and (b) Purcell soundings.

Figure 3.6 shows the vertical profile of the winds from Purcell, Oklahoma for 7–8 May. The squall line passed Purcell at ~0040 UTC 8 May. Ahead of the squall line, southerly flow was observed up to ~2 km, then the winds veered to southwesterly at middle and upper levels of the troposphere. Immediately behind the squall line, flow was southwesterly below 4–6 km and strongly southerly above. The wind profiles at upper levels resemble those observed in other squall lines (e.g., Augustine and Zipser 1987), indicating an anticyclone perturbation to the flow by the mesohigh aloft (Maddox et al. 1980). At lower levels, there is an indication of the development of a rear-inflow jet (Smull and Houze 1987b) in this early stage of the squall line evolution.

An overview of the NEXRAD and mesonet data at 0100 UTC 8 May is shown in Fig. 3.7. One can clearly see the linear extent of the squall line through southwestern Oklahoma

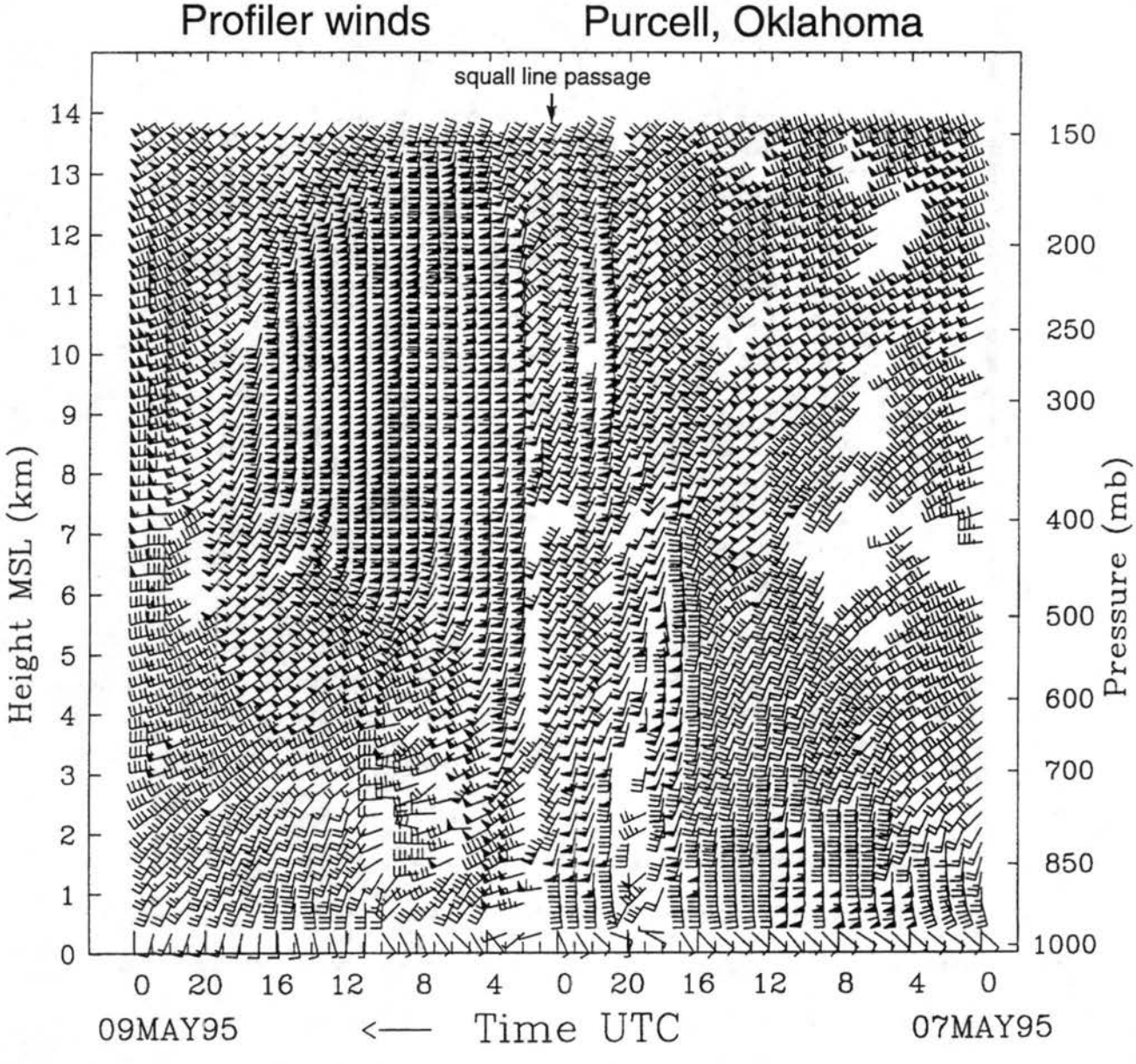

Figure 3.6: Time-height cross section of hourly averaged horizontal winds observed by the Purcell, Oklahoma, profiler on 7-8 May 1995 (half barb = 2.5 m s^{-1}; barb = 5 m s^{-1}; flag = 25 m s^{-1}).

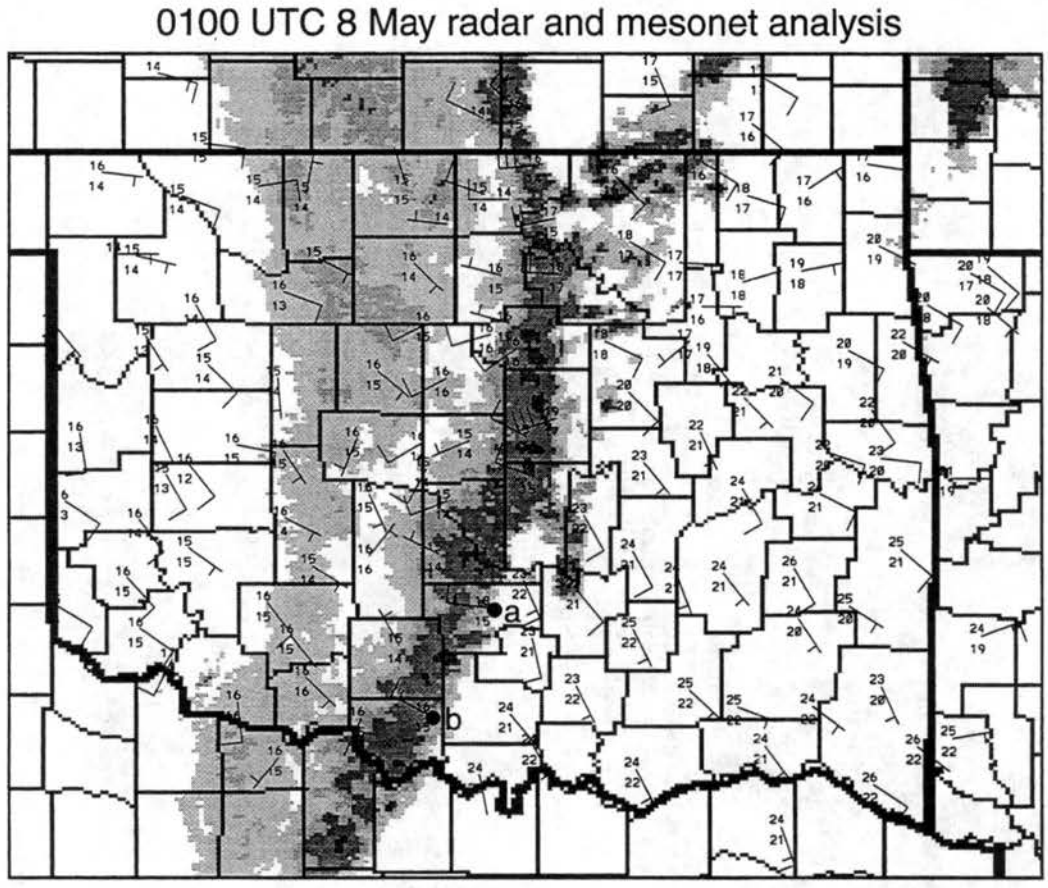

Figure 3.7: 0100 UTC 8 May 1995 Base-scan reflectivity and surface observations. Plotted are: surface winds (half barb = 2.5 m s^{-1}; barb = 5 m s^{-1}), temperature and dewpoint temperature (°C). Reflectivity values are shaded darker every 5 dBZ starting at 25 dBZ. The mesonet sites denoted by (a) and (b) are the locations of the two mesonet sites corresponding to (a) Figs. 3.8 and (b) 3.9.

at this time. The wind speed, wind direction, temperature, dewpoint and precipitation rate measured at two Oklahoma mesonetwork surface stations are shown in Figs. 3.8 and 3.9. These two stations are located 70 km apart in southwestern Oklahoma (positions noted on Fig. 3.7). Associated with the leading edge of the squall line passage were a 7°C temperature drop, a 5 mb pressure elevation and bursts of heavy rainfall from convective cells. A slight increase in precipitation associated with the secondary band region is noted between 0200 and 0300 UTC. Final passage of the squall line is denoted around 0500 UTC by rising temperatures and a decrease in the secondary band precipitation. The linear nature of this line (over southwestern Oklahoma) is documented by the similar characteristics observed at these two surface mesonetwork stations.

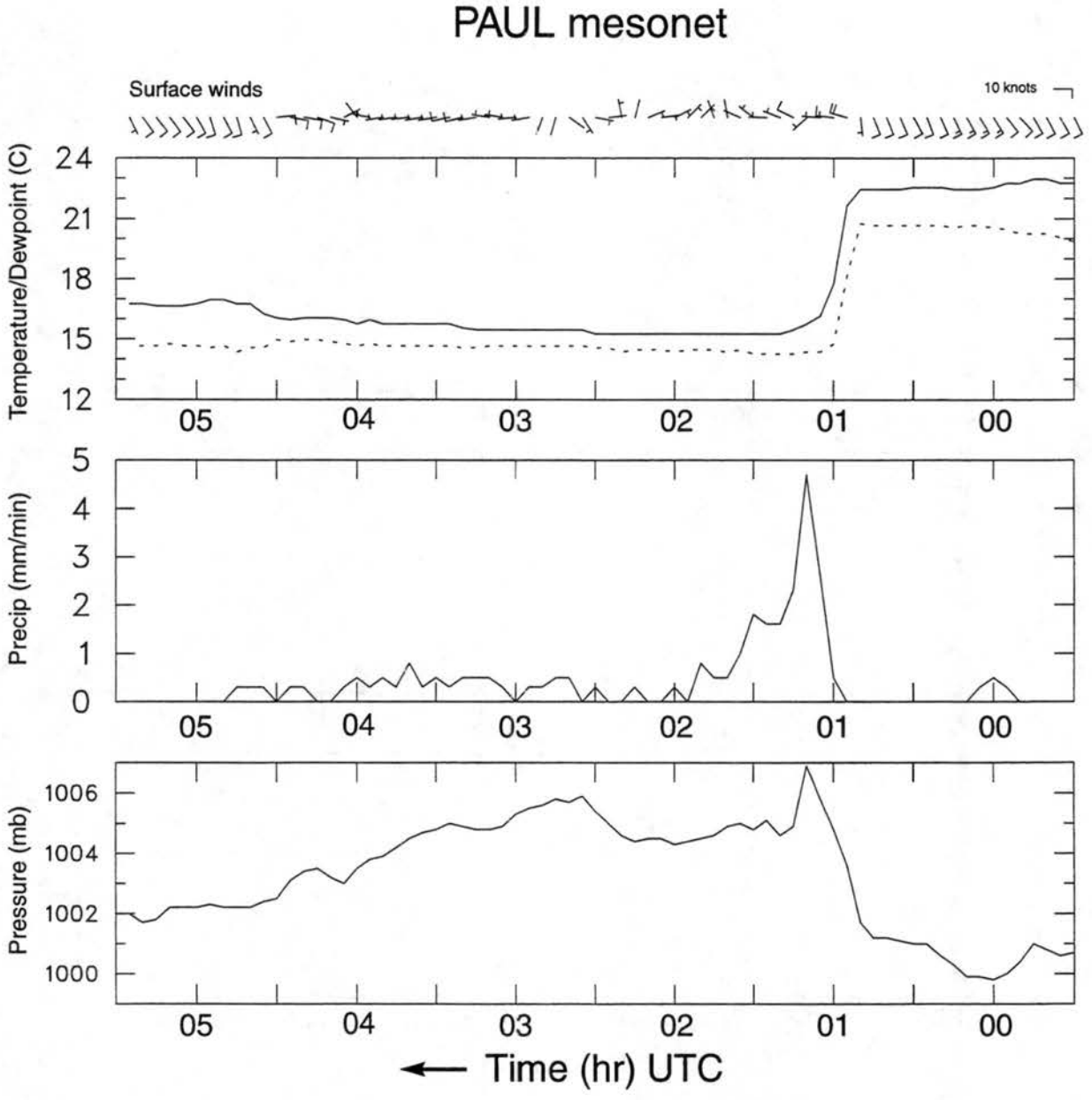

Figure 3.8: Five-minute surface observations from the PAUL,Oklahoma mesonet site. Plotted are: pressure (mb), precipitation rate (mm min^{-1}), temperature (°C), dewpoint temperature (°C), and winds (knots).

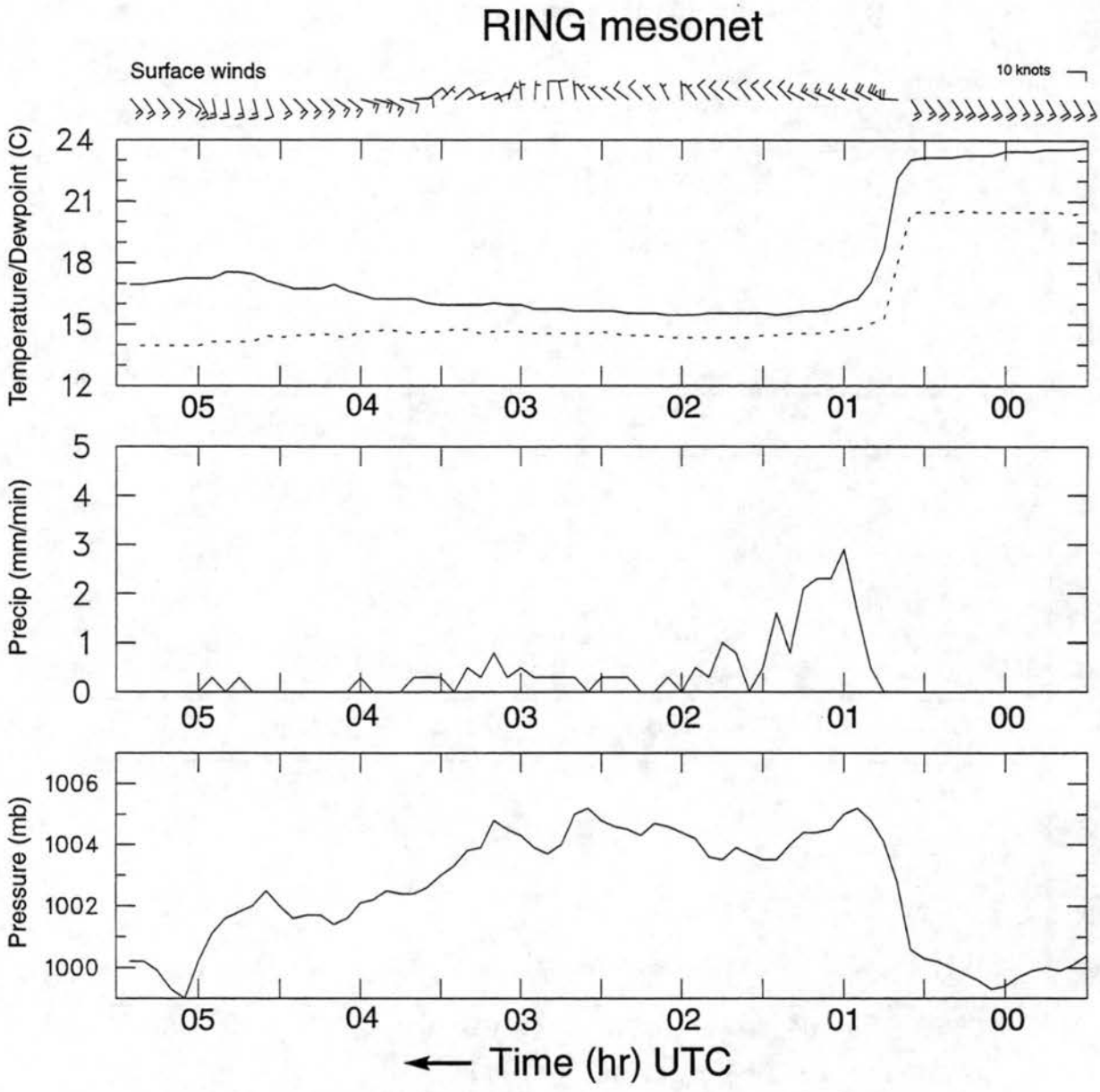

Figure 3.9: Five-minute surface observations from the RING,Oklahoma mesonet site. Plotted are: pressure (mb), precipitation rate (mm min^{-1}), temperature (°C), dewpoint temperature (°C), and winds (knots).

3.2 The convective history of 7–8 May 1995

Pre-dawn thunderstorms moved out of eastern New Mexico into the panhandles of Texas and Oklahoma and eventually merged with some thunderstorms that had formed to the east of the dryline. By 1500 UTC these storms had become organized and formed the first of two squall lines that were to propagate through Oklahoma on this day. This first squall line propagated to the northeast and eventually dissipated as it moved out of Oklahoma into Missouri.

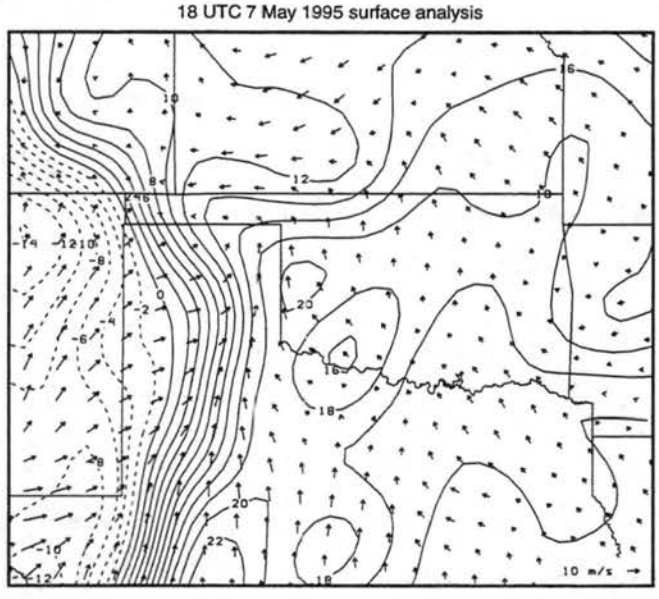

Figure 3.10: RUC (Rapid Update Cycle) analyzed surface dew-point temperature (°C) contoured every 2°C, and surface winds (m s^{-1}) at 1800 UTC 7 May 1995. Negative dew-point temperature contours are dashed.

Convection associated with the second squall line to form on 7 May (of interest in this study) initiated around 1800 UTC 7 May over the panhandle of Texas. Figure 3.10 shows the surface analysis at 1800 UTC. The most pronounced feature is a north-south oriented dryline that extends from the panhandle of Texas southward toward the Big Bend. The early initiation of the majority of this squall line was similar to the "broken line" initiation mechanism described by Bluestein and Jain (1985) while new convective elements along the southern edge of this squall line formed through "back-building." Because the main focus of VORTEX was to study tornadic thunderstorms, this squall line was observed only by

VORTEX chase teams around 2100 UTC when a LEWP (Line Echo Wave Pattern) formed (Lee and Wakimoto 1997).

The squall line was dominated by supercell thunderstorms for the first five hours of its lifetime (Lee and Wakimoto 1997). Between 0000 and 0200 UTC 8 May, the squall line took on the more classic leading line/trailing stratiform structure with primarily multicell elements at the leading edge. By late evening a continuous line of convection spanned almost 1500 km from southern Texas through central Missouri.

3.3 Satellite overview

High resolution GOES-8 Visible imagery is shown for the initiation and early evolution of this squall line (Fig. 3.11). At 1815 UTC (Fig. 3.11a) the squall line was comprised of a series of supercells over the panhandle of Texas extending through western Kansas. The convection associated with the MCS that developed earlier in the day can be seen over north-central Texas and central Oklahoma.

By 2015 UTC (Fig. 3.11b) the squall line had become continuous, with an upper-tropospheric anvil shield beginning to form at this time. The 2215 UTC image (Fig. 3.12a) shows that an extensive trailing anvil had formed over the northern portion of the line. A large pre-squall-line supercell located over central Texas had developed and its extensive anvil blow off streamed northwestward ahead of the squall line's leading anvil. The southern part of squall line had no trailing anvil present because the upper level winds sheared the cell anvils north-northeast of the line. By 2315 UTC (Fig. 3.12b), an extensive trailing anvil had formed over the southern part of the squall line. This last visible image documents this squall line's anvil structure about one hour before the ELDORA first intercepted the line.

3.4 NEXRAD and lightning overview

Base-scan NEXRAD composite radar images are presented for times corresponding to 1800, 2000, 2200 UTC 7 May, and 0000, 0200, 0350 UTC 8 May 1995. Corresponding cloud-to-ground lightning locations for a 30 min period (centered on the NEXRAD composite time) are also presented.

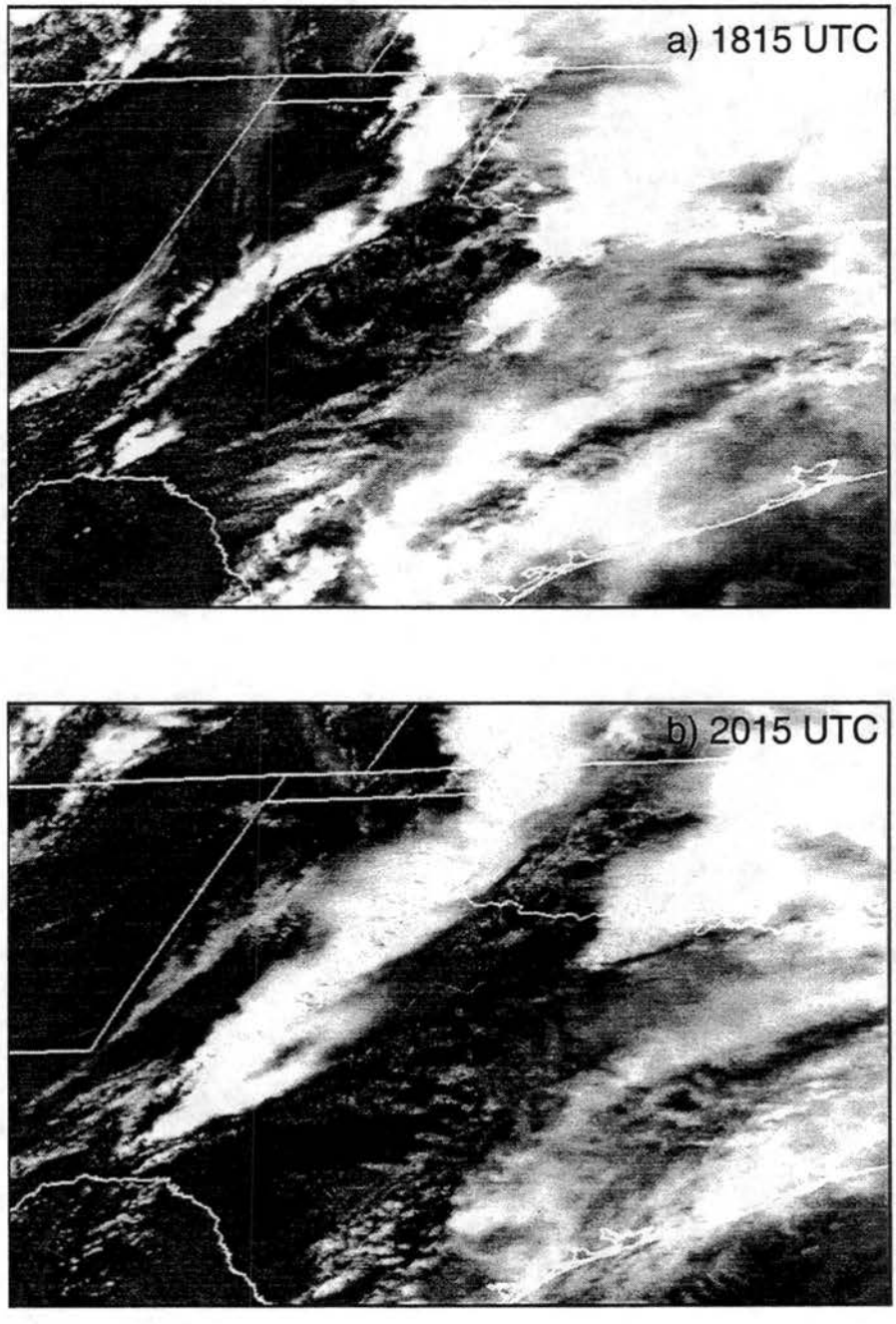

Figure 3.11: GOES-8 high-resolution visible imagery at (a) 1815 UTC (b) 2015 UTC 7 May 1995.

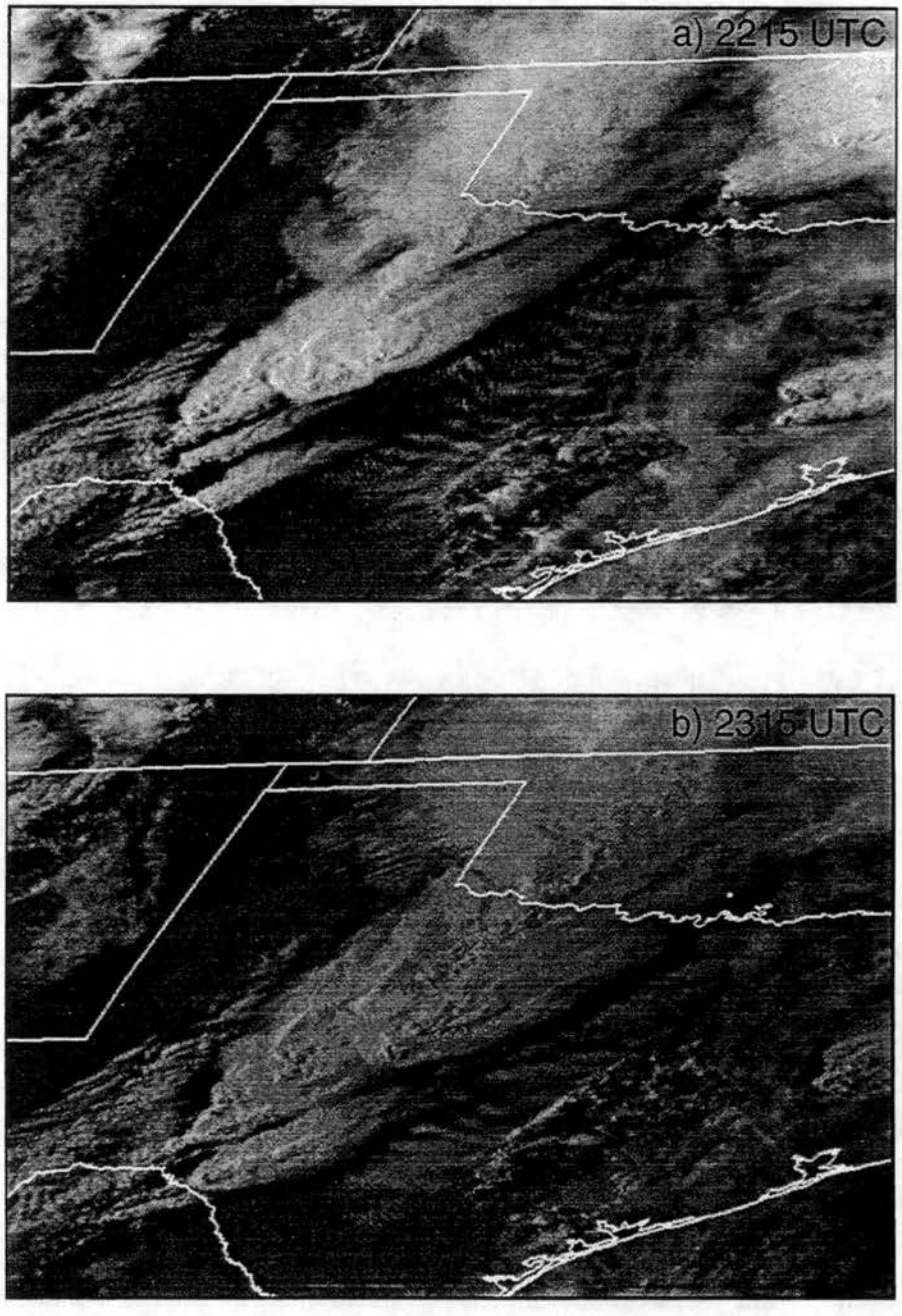

Figure 3.12: GOES-8 high-resolution visible imagery at (a) 2015 UTC (b) 2315 UTC 7 May 1995.

Convective initiation associated with the dry line is shown in Fig. 3.13a. New cumulonimbus initiation continued through 2000 UTC (Fig. 3.14a) and by 2200 UTC (Fig. 3.15a) the squall line had become a continuous line of convection. Many reports of hail (to 6 cm), strong winds (to 40 m s^{-1}) and radar reflectivities exceeding 60 dBZ were associated with the early stages of this squall line. Cloud-to-ground lightning patterns observed during the initiation and early stages of the squall line (Figs. 3.13b, 3.14b, 3.15b) were dominated by positive flashes consistent with previous studies documenting severe convection (e.g. Stolzenburg 1994). The LEWP mentioned earlier is present at both 2200 and 0000 UTC over western Oklahoma. To the south of the LEWP, the line is linear and stays this way for the rest of its life cycle. The 0000 UTC 8 May analysis (Fig. 3.16a) shows secondary bands of enhanced precipitation over the northern part of the squall line; the southern end does not show any signs of secondary enhanced precipitation. Ahead of the squall line lay some pre-squall convection. By 0200 UTC 8 May (Fig. 3.17a), this line exhibited secondary extensive bands of precipitation over the entire line. The line continued to widen through 0350 UTC (Fig. 3.18a) with several large plumes of enhanced secondary band precipitation observed to the rear of the leading-line convection.

Cloud-to-ground lightning patterns observed during the maturation phase of the squall line (Figs. 3.16b, 3.17b, 3.18b) show a transition to a "bipolar" lightning configuration (e.g. Rutledge and MacGorman 1988) with predominately negative flashes within the leading–line convection and positive flashes co–located within the enhanced secondary band precipitation consistent with previously observed mature squall lines (e.g. Rutledge et al. 1990).

Figure 3.19 shows a NEXRAD national radar summary at 0430 UTC when the line was most expansive. Secondary bands of precipitation were almost continuous in the line north of the Texas/Oklahoma border. South of this border, the squall line had only patchy secondary bands of precipitation. This is consistent with the upper-tropospheric flow documented by soundings (Fig. 3.5) and satellite imagery (Fig. 3.12) that shows shearing of the anvil condensate in a direction along the line that would not be favorable for the formation of secondary bands of precipitation at its southern end.

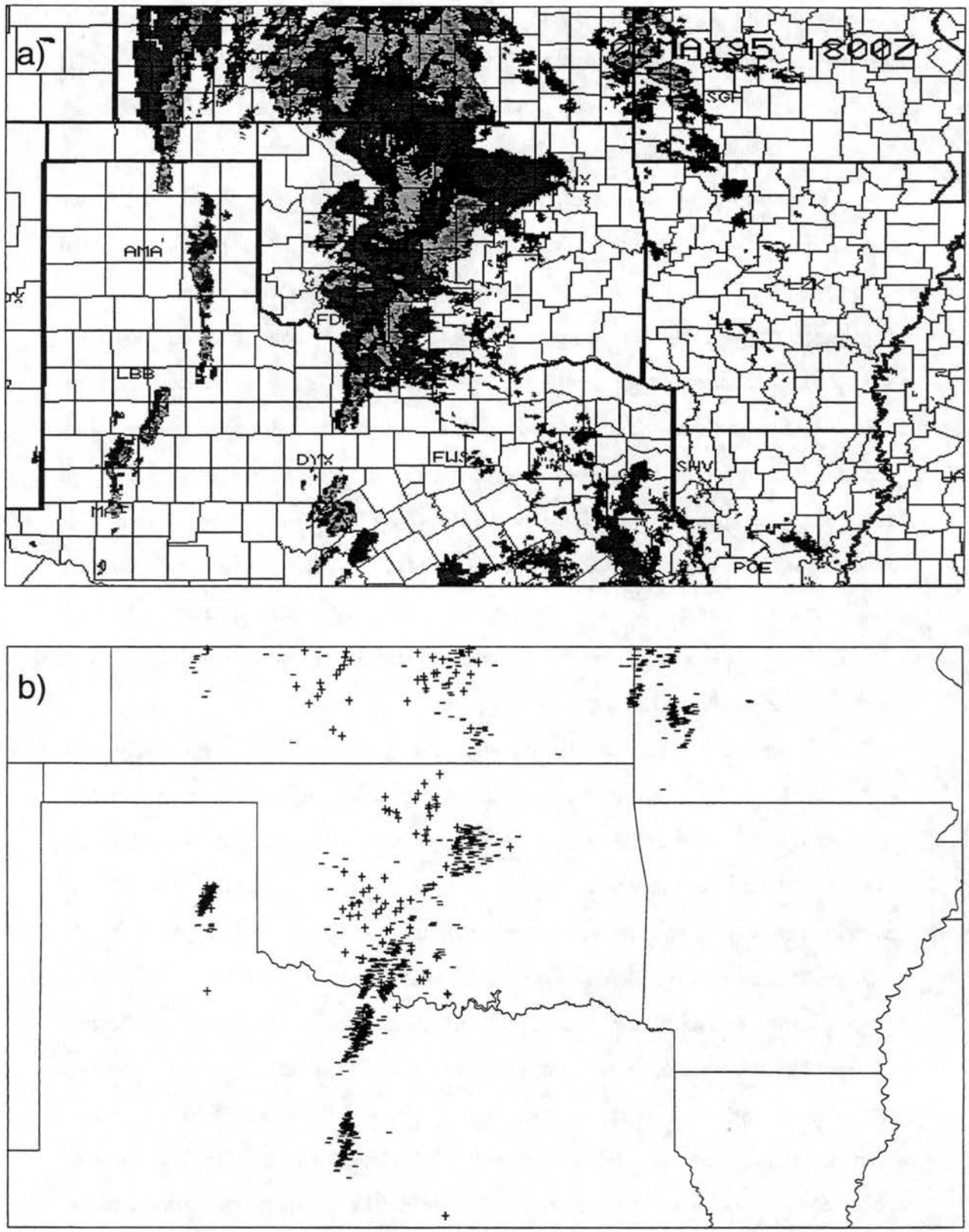

Figure 3.13: Regional NEXRAD composite summary (a) at 1800 UTC 7 MAY 1995, and (b) cloud-to-ground lightning locations over a 30 min period centered on 1800 UTC. Negative (-) and plus (+) signs denote locations of negative and positive cloud-to-ground lightning flashes, respectively.

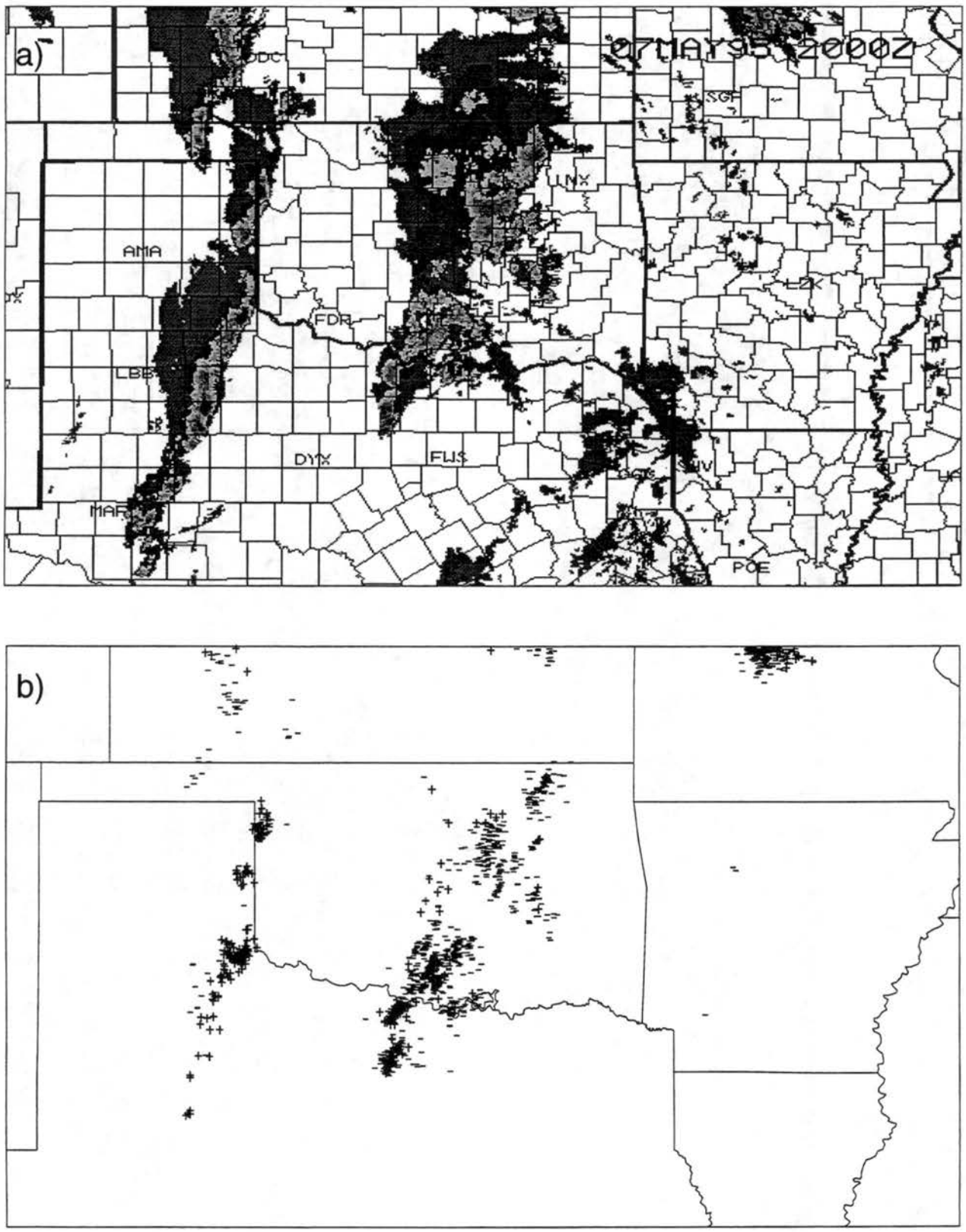

Figure 3.14: As in Fig. 3.13 except for 2000 UTC 7 May 1995.

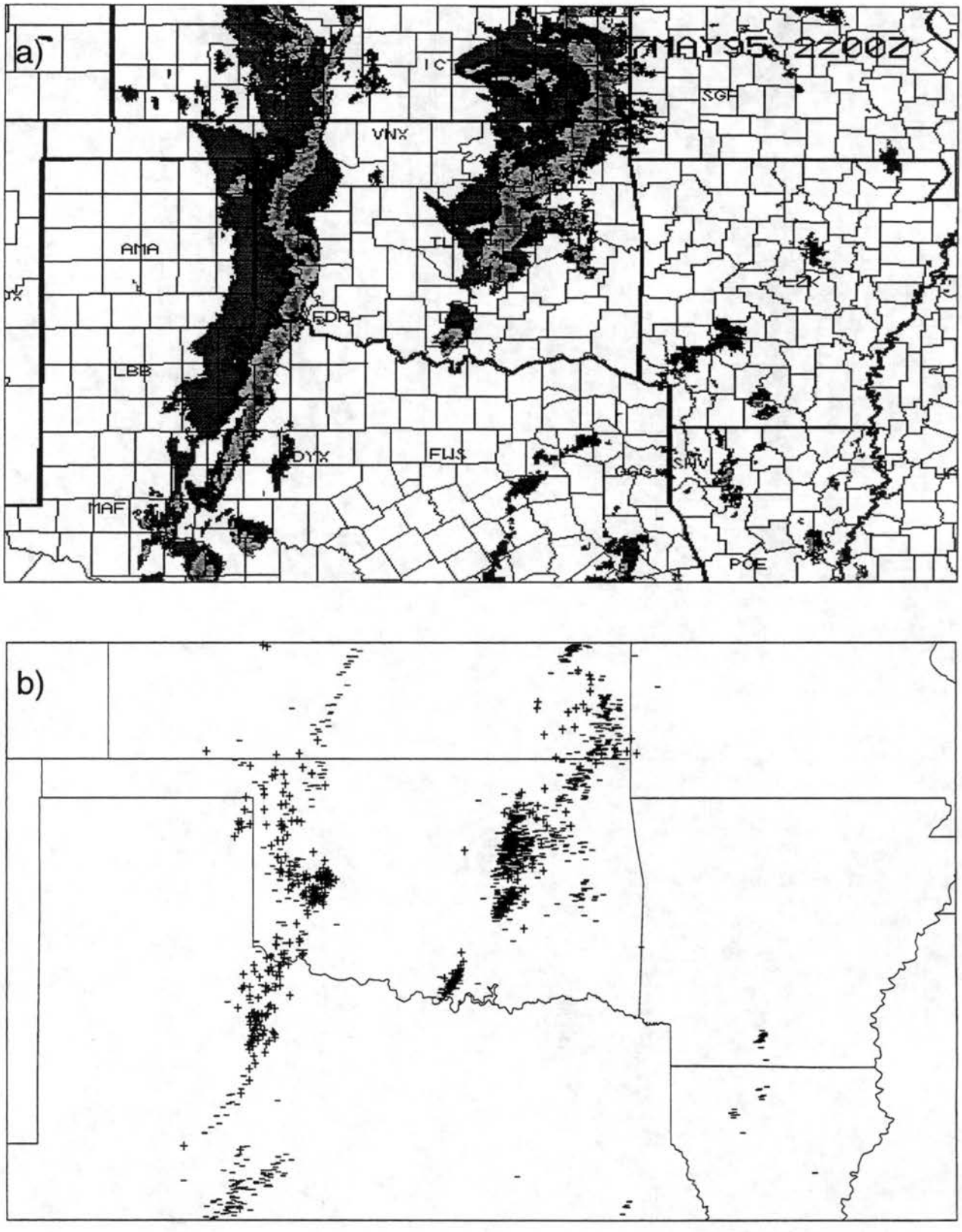

Figure 3.15: As in Fig. 3.13 except for 2200 UTC 7 May 1995.

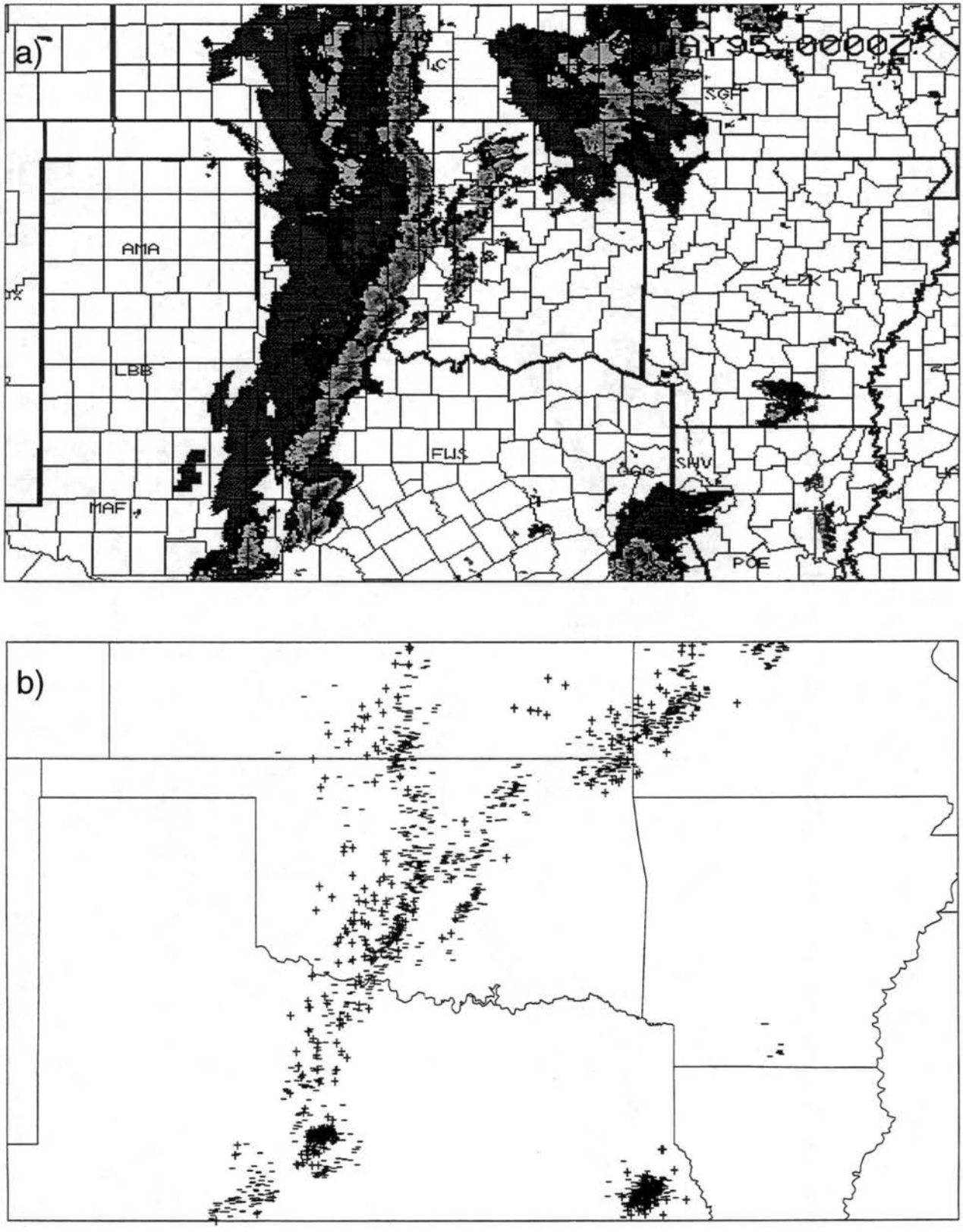

Figure 3.16: As in Fig. 3.13 except for 0000 UTC 8 May 1995.

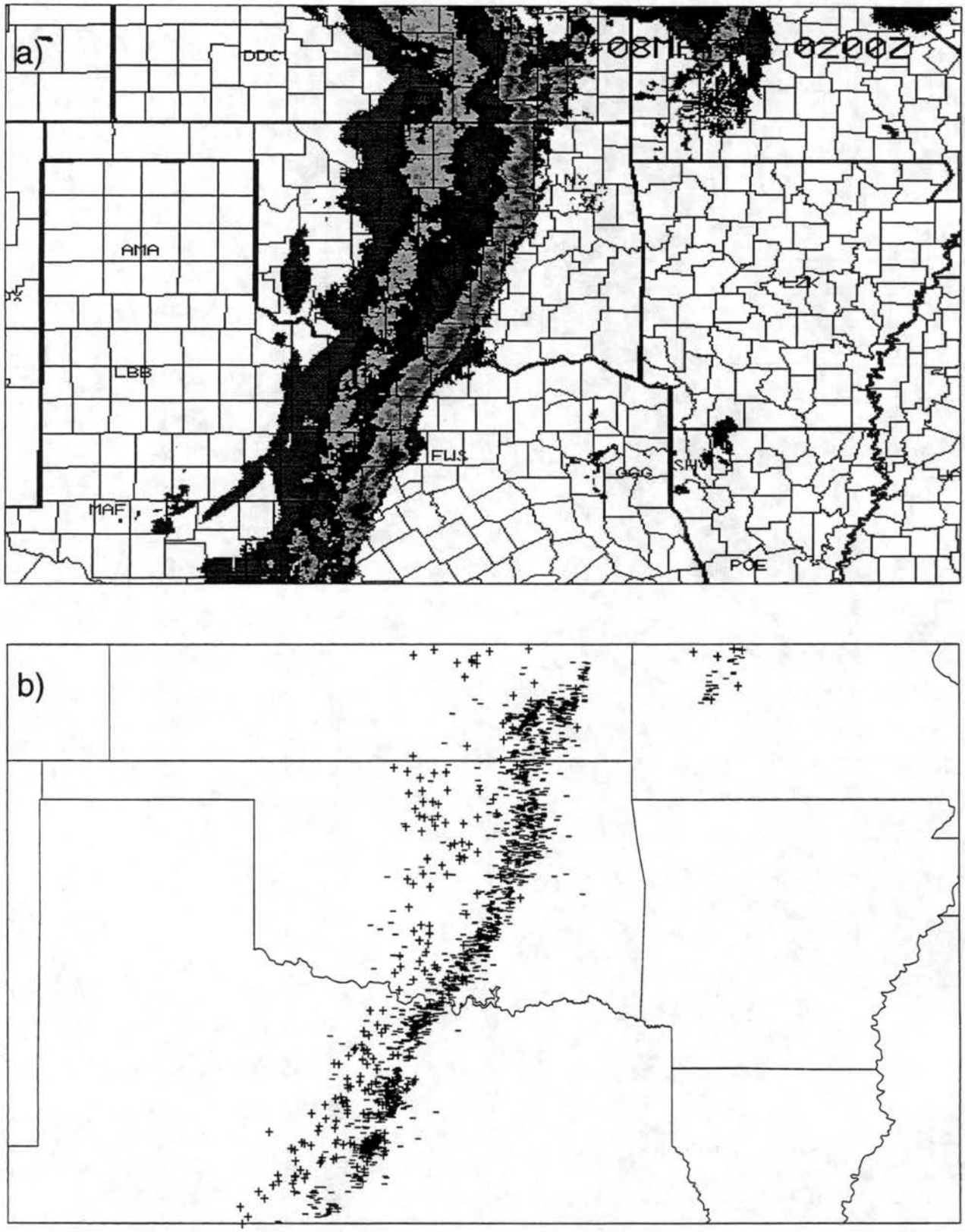

Figure 3.17: As in Fig. 3.13 except for 0200 UTC 8 May 1995.

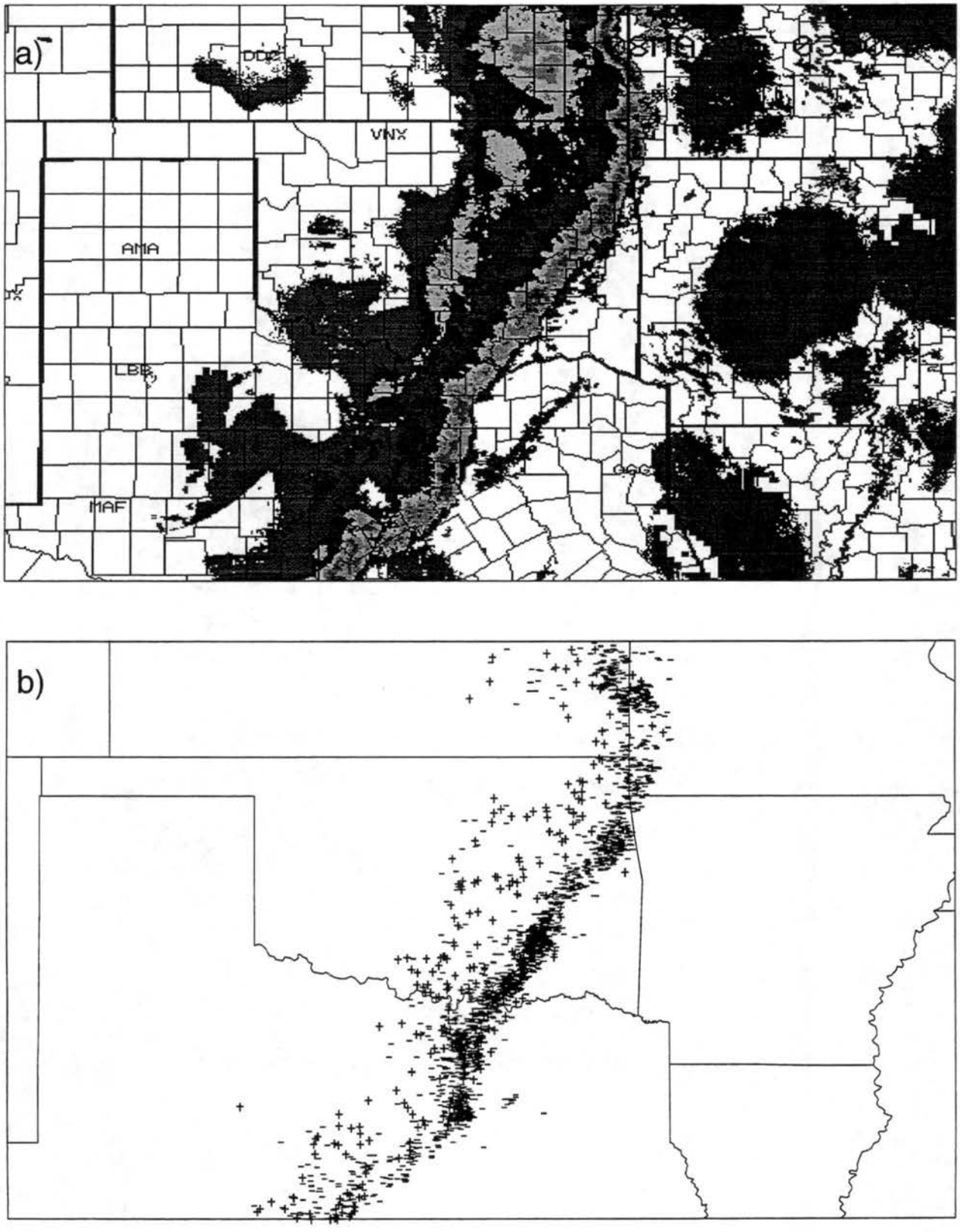

Figure 3.18: As in Fig. 3.13 except for 0350 UTC 8 May 1995.

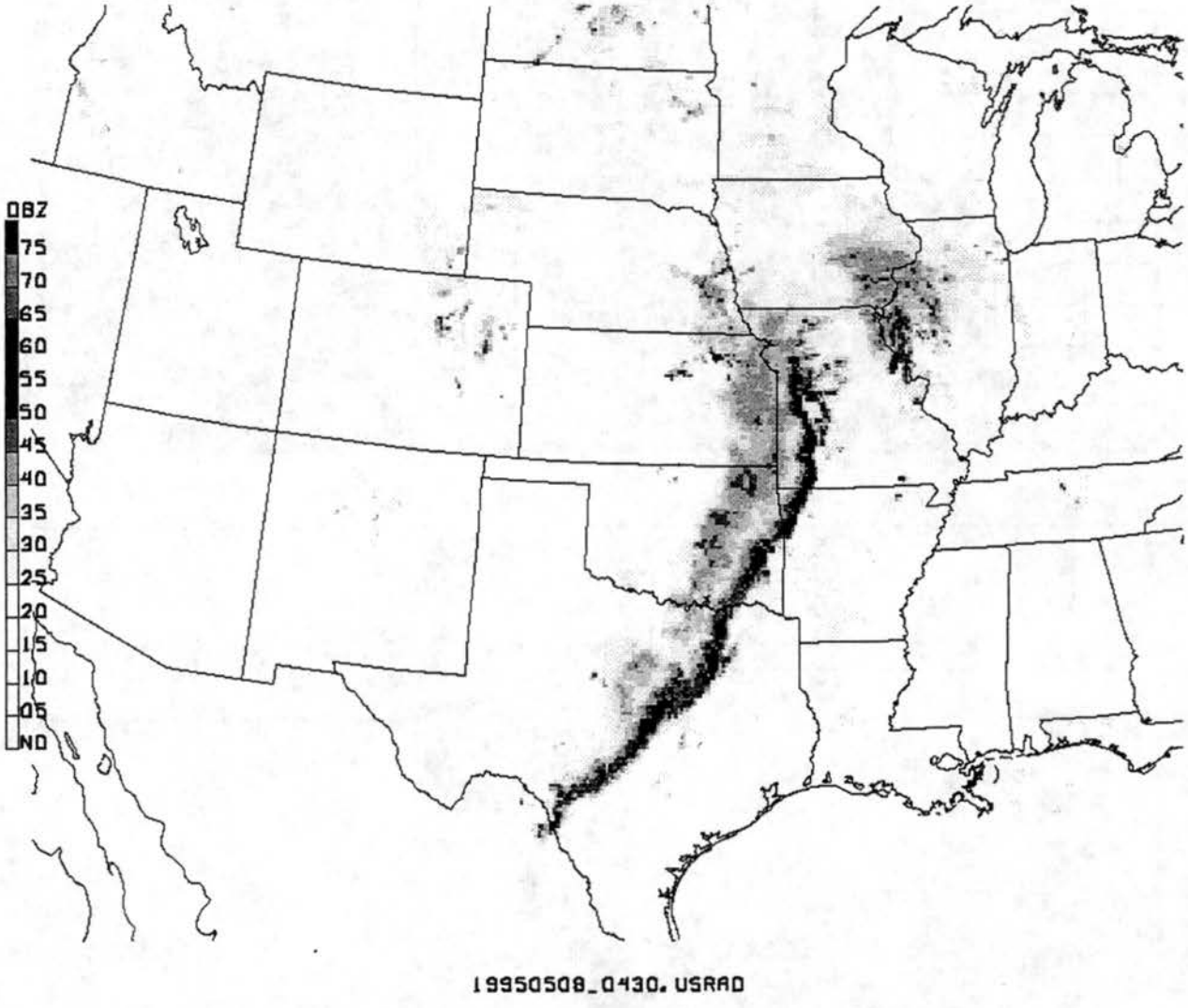

Figure 3.19: 0430 UTC 8 May 1995 NEXRAD national radar summary.

Chapter 4

GRAVITY WAVES, JETS AND OTHER FINE-SCALE FEATURES

To visualize the mean reflectivity and kinematic characteristics of this squall line, and to facilitate comparison with previous squall line studies, composited mean cross sections will be examined. Individual line-perpendicular cross sections of the high-resolution ELDORA data are then provided to highlight specific fine-scale features within this squall line. Later in this Chapter, horizontal and line-parallel cross sections will be presented to give insight into the line's fine-scale three-dimensional structure. Figure 4.1 shows a horizontal reflectivity cross section ($Z = 2.5$ km) at 0100 UTC identifying the track of the *Electra* and locations of representative vertical cross sections and domains of horizontal cross sections analyzed throughout this Chapter.

A larger view of the squall line at this time can be seen from the 0100 UTC Fredrick, Oklahoma base-scan NEXRAD reflectivity data (Fig. 4.2). Observed are the leading-line convection followed by a weak area of secondary band precipitation.

4.1 MEAN reduced-resolution cross sections

To summarize the mean two-dimensional structure of this squall line, along-line averaged profiles of the reflectivity and kinematic fields are presented. Line-averaged cross sections (from $Y = -10$ to 70 km of the squall line) of reduced-resolution ELDORA data are presented in Fig. 4.3.

The reason for presenting a reduced-resolution view is twofold: 1) the limitations of the software analysis package (CEDRIC) did not allow for processing of all the high-resolution data at once; and 2) to help facilitate comparisons with previous lower-resolution dual-Doppler squall line analyses.

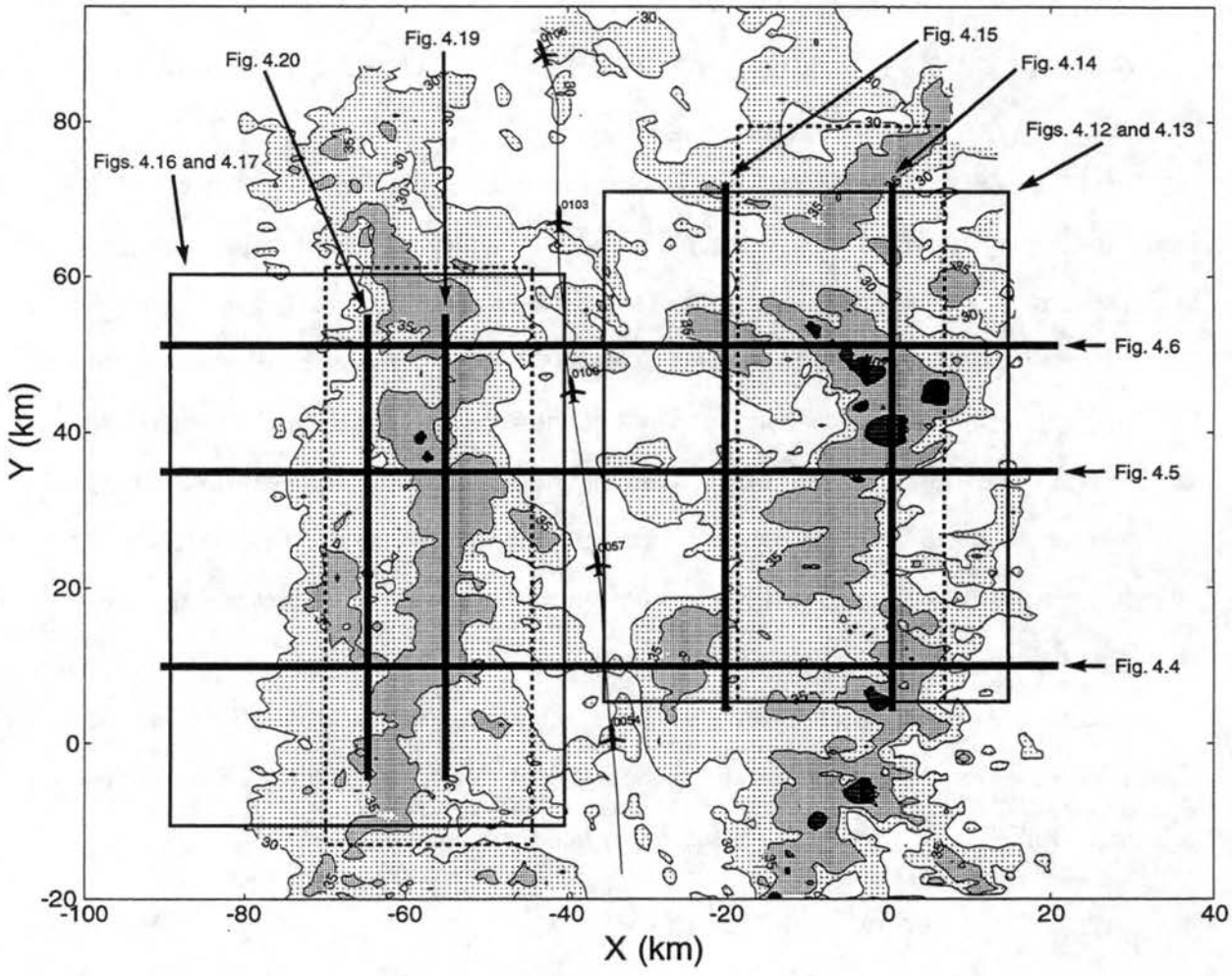

Figure 4.1: The 0100 UTC reflectivity field at 2.5 km (near the level of the bright band) with the locations of vertical cross sections (thick solid lines), areas of detailed analysis (solid-lined rectangles) and regions used for the volume statistics analysis in Chapter 5 (dashed-lined rectangles). Light, medium and dark shading correspond to reflectivity values greater than 30, 35 and 40 dBZ, respectively. *Electra* flight path and times (UTC) are indicated by the airplane silhouettes.

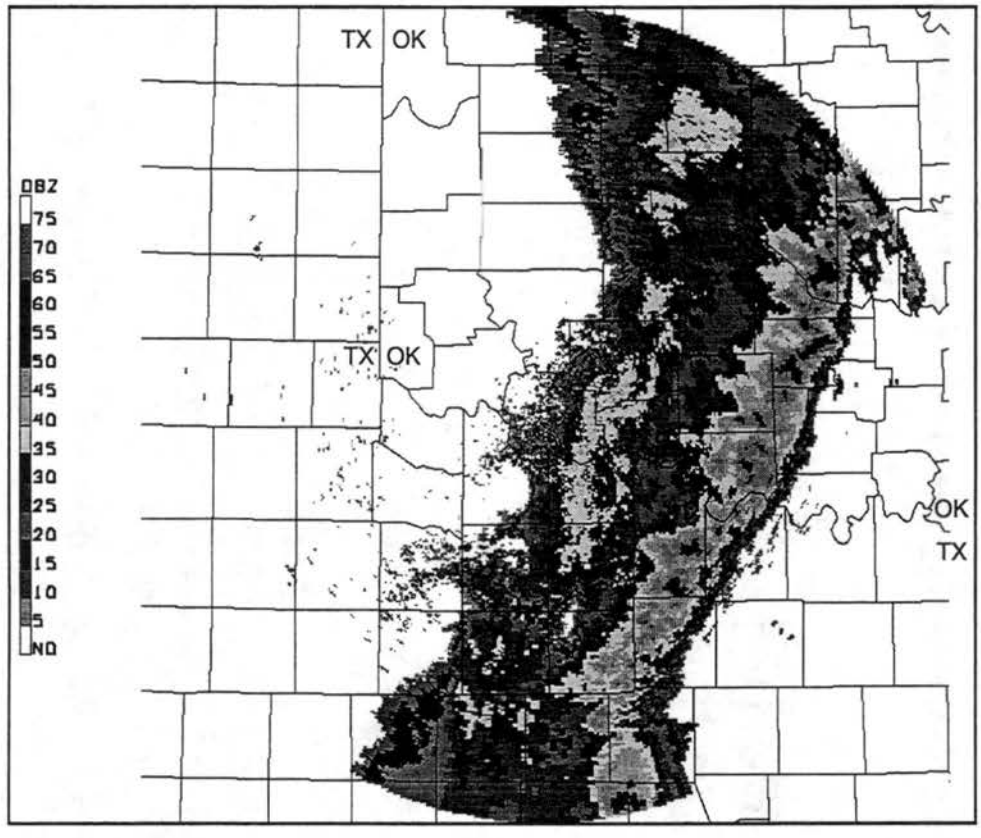

Figure 4.2: 0100 UTC 8 May 1995 base-scan KFDR NEXRAD reflectivity image

Grid spacing for these data are 0.6 km in the horizontal and 0.5 km in the vertical, and resolvable wavelengths are now > 4.8 km. These are comparable to the wavelengths of motion resolved for the 10–11 June 1985 squall line (e.g., Biggerstaff and Houze 1991a, 1993). Due to the scanning limit of ELDORA, coverage through to the leading edge of the squall line is not depicted in these cross sections. From careful comparison with NEXRAD data (not shown), it was determined that these data extend to within $\sim$10 km of the leading edge of this squall line.

Shown in Fig. 4.3a is the mean reflectivity field present over this 80 km long region of the squall line. Clearly defined are the convective-line, transition zone and secondary band regions of this squall line. The elevated cell structure observed near $X = 5$ km comes from sampling a few of the elevated new cells forming near the leading edge of this line. Decaying convective cells, with precipitation cores at lower levels, are represented by the large reflectivity maximum ($\geq$35 dBZ) centered near $X = -5$ km. Precipitation fallout

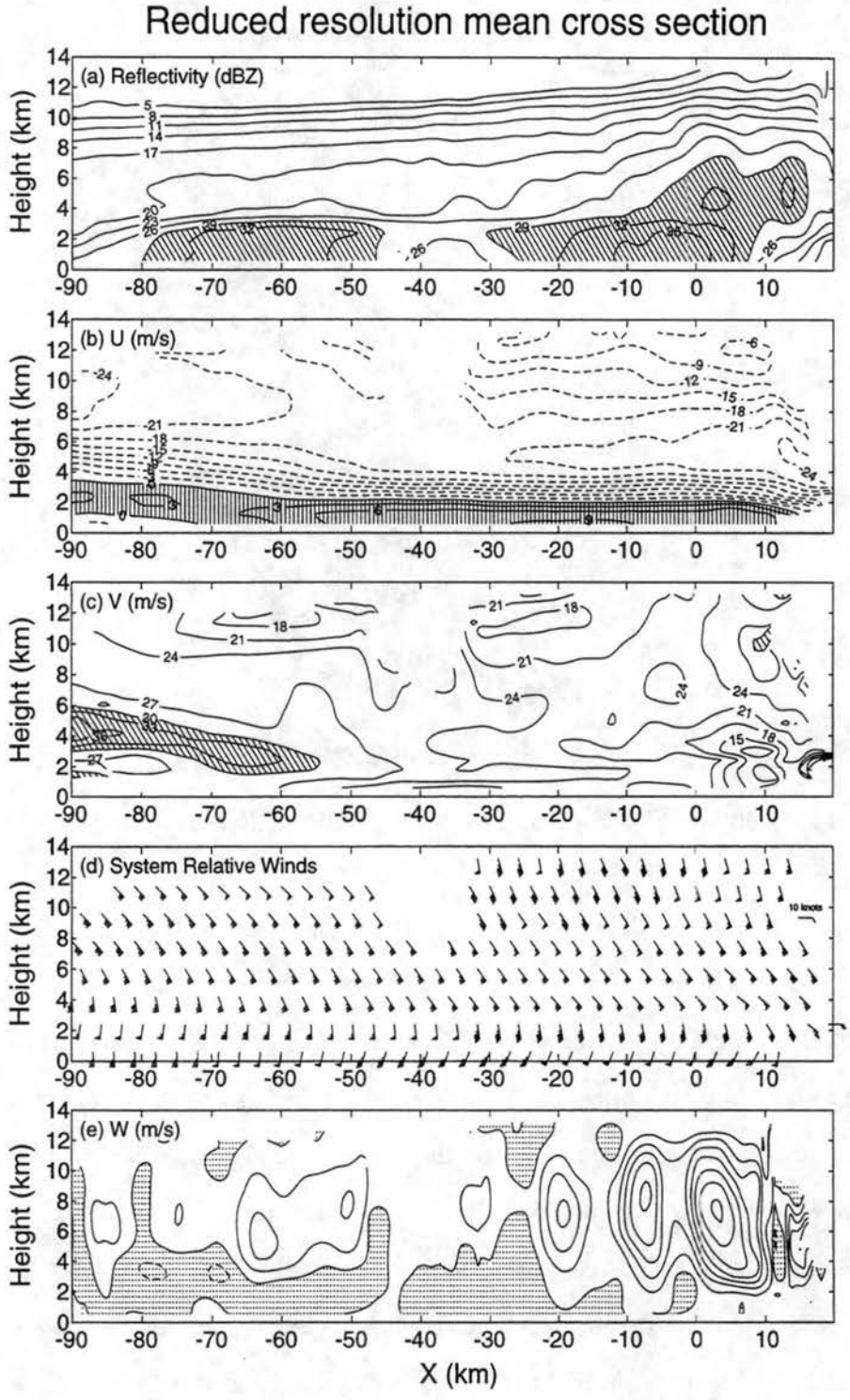

Figure 4.3: MEAN reduced resolution cross section over 80 km of the squall line from $Y = -10$ to 70 km depicting (a) reflectivity (dBZ) contoured every 3 dBZ, (b) U (system-relative) contoured every 3 m s^{-1}, (c) V (system-relative) contoured every 3 m s^{-1}, (d) horizontal winds in wind profiler format, and (e) vertical velocity contoured every 0.5 m s^{-1}. In (a), hatching indicates reflectivity >29 dBZ. In (b), negative contours are dashed, vertical hatching indicates positive (RTF) flow. In (c), hatching indicates V flow >30 m s^{-1}. In (e), negative vertical motions are shaded.

from decaying convective cells is observed by way of the decreasing slope in reflectivity from $X = 0$ to -20 km. This precipitation structure is very similar to the 22 May 1976 squall line investigated by Smull and Houze (1987a) (hereafter referred to as SH).

To the rear of the convective line, a gentle downward slope to the mid and upper-troposphere reflectivity field is observed. Ice particles lofted within convective updrafts are advected rearward by system-relative winds and gradually settle out under the influence of gravity (e.g., Gamache and Houze 1982; Rutledge and Houze 1987).

The transition zone appears as a low-level reflectivity minimum from $X = -25$ km to -45 km, and is a region of separation between the leading line convection and the trailing secondary band precipitation. Low-level reflectivity minimum have been documented in previous squall line studies (e.g., Ligda 1956; Smull and Houze 1985; Rutledge et al. 1988; Biggerstaff and Houze 1991a).

The secondary band's precipitation region is located between $X = -45$ and -80 km. Enhanced precipitation below a weak bright band can be seen between $X = -54$ and -74 km.

Line-perpendicular and line-parallel components of the system-relative horizontal flow will be referred to as the U and V-components, respectively, of the horizontal flow. In the U field (Fig. 4.3b) a rear-to-front (RTF) flow is observed below 3 km along the back edge, and descends to below 2 km within the secondary band region. Also observed is an increase in magnitude of the RTF flow as it approaches the leading-line convective region. This RTF flow profile is very similar one that Klimowski (1994) observed during the formation of a North Dakota squall line. Klimowski found that the RTF flow expanded rearward as the squall line continued to mature. Because there is only one pass by ELDORA on this squall line, it is not possible to comment on the issues of formation and evolution of the RTF flow.

To the rear of the squall line, the RTF flow generally weakens in magnitude. RTF flow up to 8 m s^{-1} through the secondary band region of this squall line is observed. This would classify this squall line as a weak rear-inflow case according to Smull and Houze (1987b). However, analysis of the composited NEXRAD base-scan reflectivity data (not shown) show the secondary band to moving more slowly than the 12.2 m s^{-1} convective

line ($\sim$9 m s^{-1} from 300°). Thus, from the secondary band's reference frame, the RTF flow would be $\sim$3 m s^{-1} faster than that shown in these cross sections, which would then categorize this squall line as one with a strong rear inflow according to Smull and Houze (1987b).

Front-to-rear (FTR) flow is observed through the mid and upper levels of the squall line. Within the convective-line, the strongest FTR flow is located near the leading edge of the squall line (at $Z = 5$ km), consistent with previous observational (e.g., LeMone 1983; SH; Biggerstaff and Houze 1991a) and modeling (e.g., Fovell and Ogura 1988) studies. Rearward, enhanced FTR flow at upper levels above the secondary band region can be seen.

Probably the most striking kinematic feature of this squall line is the magnitude of V (Fig. 4.3c). Within the convective line, V is observed to increase with height similar to that observed by Kessinger et al. (1987). Rearward, V is observed to be in the form of a jet-like feature located within, and to the rear of, the secondary band region. Most symmetric squall lines that have been studied (e.g., 22 May 1976, 10–11 June 1985) have had V-component velocities that were generally weaker in magnitude than the U-component. The extent to which the strong V-component interacted with this squall line's evolution and structure is unknown at this time; however, the unusually strong V may have contributed to the exceptional north-south extent of the squall line (Fig. 3.16).

System-relative components of horizontal winds are presented in a wind profiler-type format in Fig. 4.3d. This documents nicely how much larger in magnitude V is, compared to U, throughout this squall line.

The mean cross section of vertical velocity (Fig. 4.3e) shows updrafts associated with the leading-line convection as having have a rearward tilt with height (as seen near $X =$ 5 km). This structure is very similar to the slantwise upward flow that has been observed in previous lower-resolution dual-Doppler analyses of squall lines (e.g., SH; Biggerstaff and Houze 1991a, 1993; Bluestein et al. 1993). Low-level precipitation driven downdrafts are observed between $X = 0$ and -20 km, while regions of upper-level descent are observed at the rear edge of the convective line region (near $X = -25$ km).

Within the secondary band a region of mesoscale descent underlying a region of mesoscale ascent is observed, consistent with the broad pattern shown in Fig. 1.1. The enhanced updraft observed near the leading edge of the secondary band (near $X = 50$ km) is consistent with that documented by Matejka and Schuur (1991).

4.2 Line-perpendicular cross sections

To highlight the fine-scale features observed by ELDORA, individual line-perpendicular cross sections of high-resolution data are now presented.

4.2.1 Reflectivity

Cross sections of reflectivity (Figs. 4.4a, 4.5a and 4.6a) show a sequence of cells in various stages of evolution within the convective-line region. Mature cells are located near $X = 0$ km (Figs. 4.4a and 4.5a), while a decaying set of cells are shown near $X = -5$ and -20 km in Fig. 4.6a. Reflectivity maxima associated with newer cells can be seen near $X =$ 15 km in Figs. 4.4a and 4.5a, though it should be noted that attenuation of the radar beams has underestimated some of the low-level reflectivity at these distances. Large convective cells are observed to be vertical in structure through their mature phases (e.g., near $X = 0$ km in Figs. 4.4a and 4.5a), and then become somewhat disorganized during their decaying phases (e.g., $X = -20$ km in Fig. 4.6a). A broad spreading of the precipitation associated with decaying cells is noted rearward of deep convection (e.g., near $X = -20$ km in Figs. 4.4a and 4.6b). Enhancement of reflectivity near the melting level ($\sim$3 km), likely due to ice fallout from decaying convection, is also noted through this region.

The transition zone shows up in these cross sections as a region of decreased reflectivity located below 3 km (e.g., centered near $X = -40$ in Figs. 4a, 5a and 6a). Figures 4.4a and 4.6a show a decrease in 20 dBZ reflectivity contour between $X = -40$ and -30 km. Though not observed in Fig. 4.5a, these minima are worth noting as they could be an indication of regions of mesoscale descent that have been documented in previous transition zone studies (e.g., Biggerstaff and Houze 1991a, 1993; Braun and Houze 1994). SH documented similar mid-tropospheric minima in reflectivity correlated with the transition zone. Due to the high

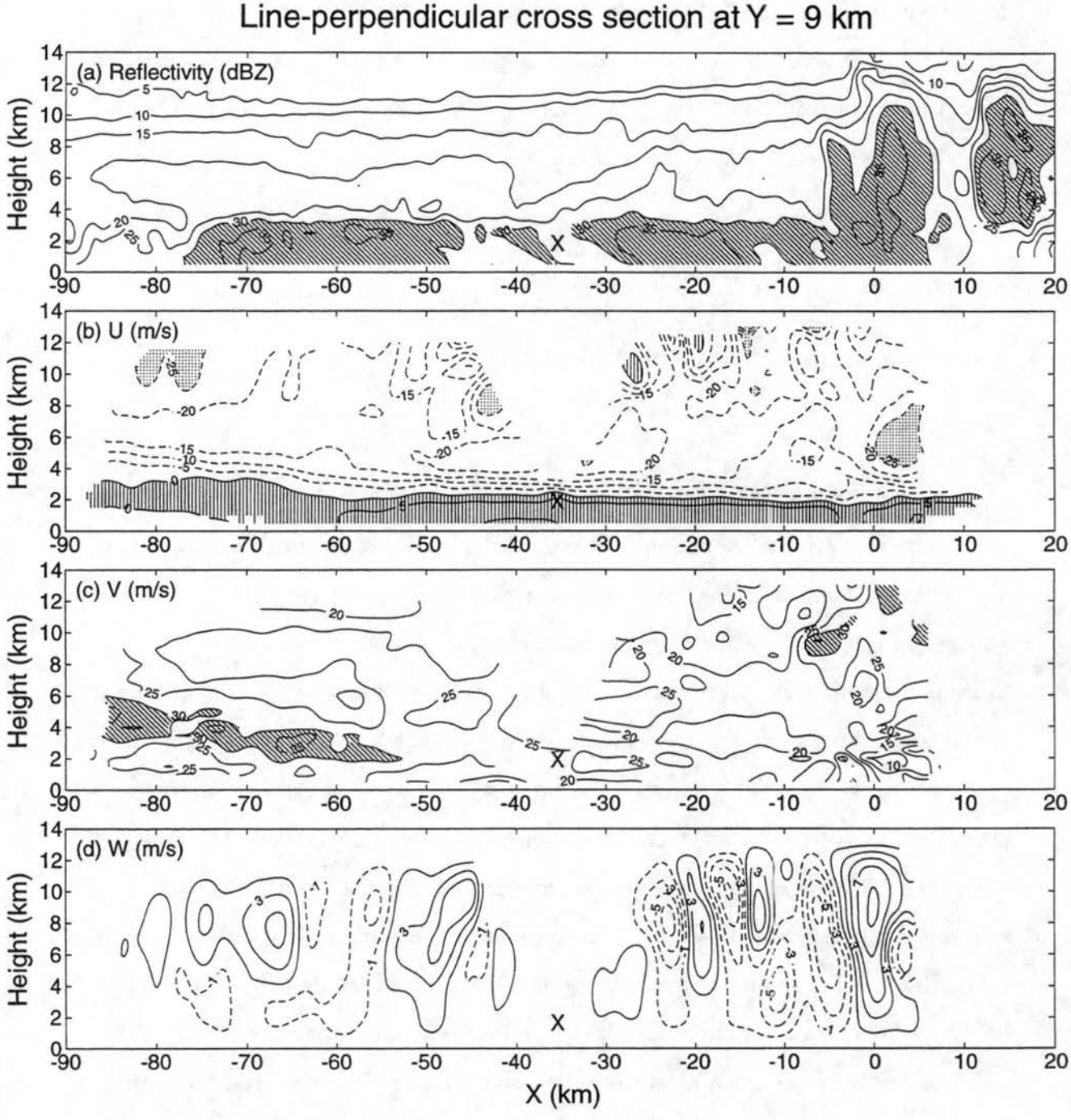

Figure 4.4: Line-perpendicular cross section along $Y = 9$ km showing (a) reflectivity (dBZ) contoured every 5 dBZ, (b) U contoured every 5 m s^{-1}, (c) V contoured every 5 m s^{-1}, and (d) vertical velocity contoured every 2 m s^{-1}. In (a), light hatching indicate reflectivity >30 dBZ and dark hatching indicate reflectivity >40 dBZ. In (b), negative contours are dashed, vertical hatching indicates positive (RTF) flow and shading indicates negative (FTR) flow <-30 m s^{-1}. In (c), negative contours are dashed and hatching indicates flow >30 m s^{-1}. In (d), negative contours are dashed and the zero contour is omitted. The position of the it Electra is indicated by the X.

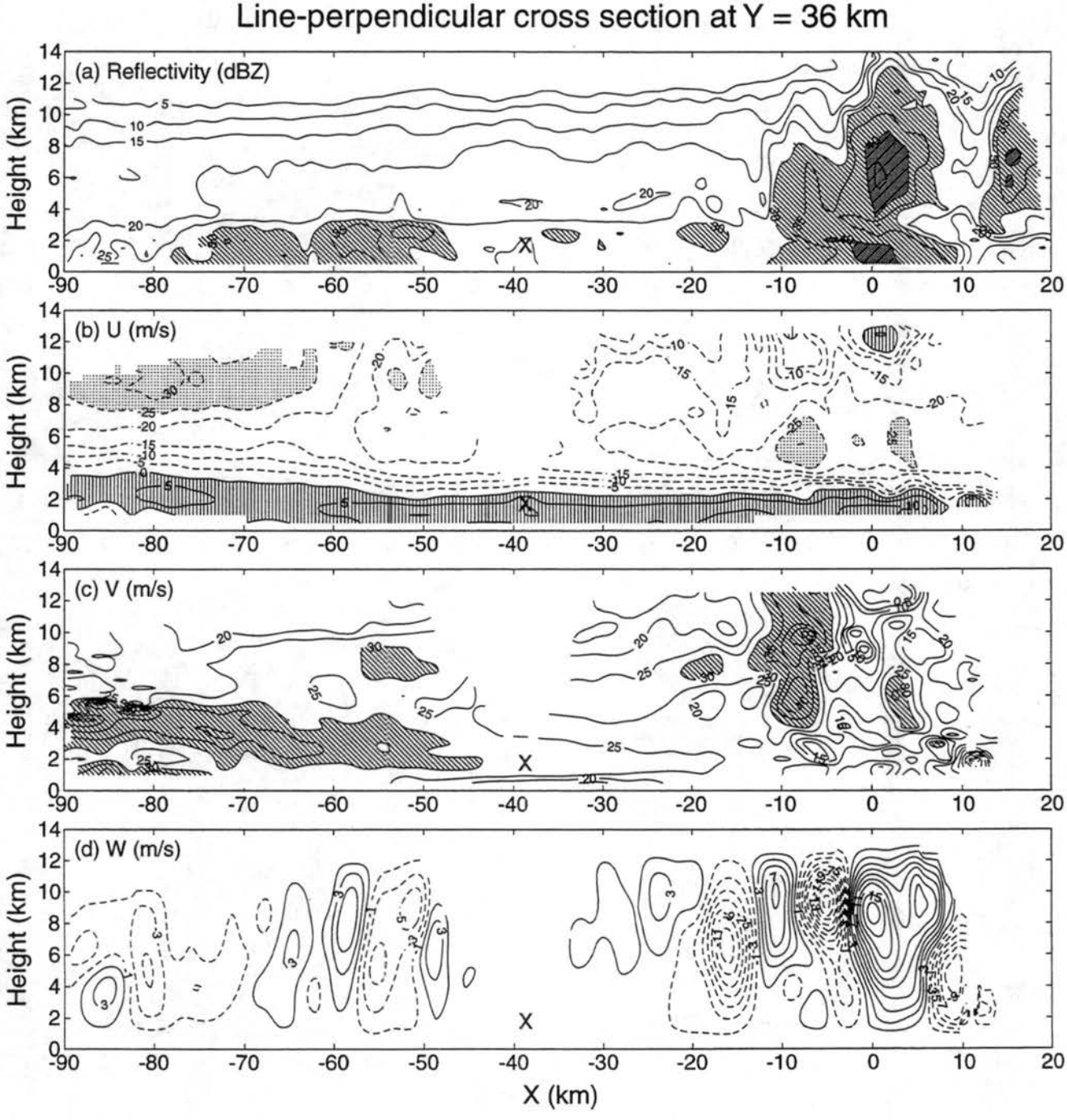

Figure 4.5: As in Fig. 4.4 except along $Y = 36$ km.

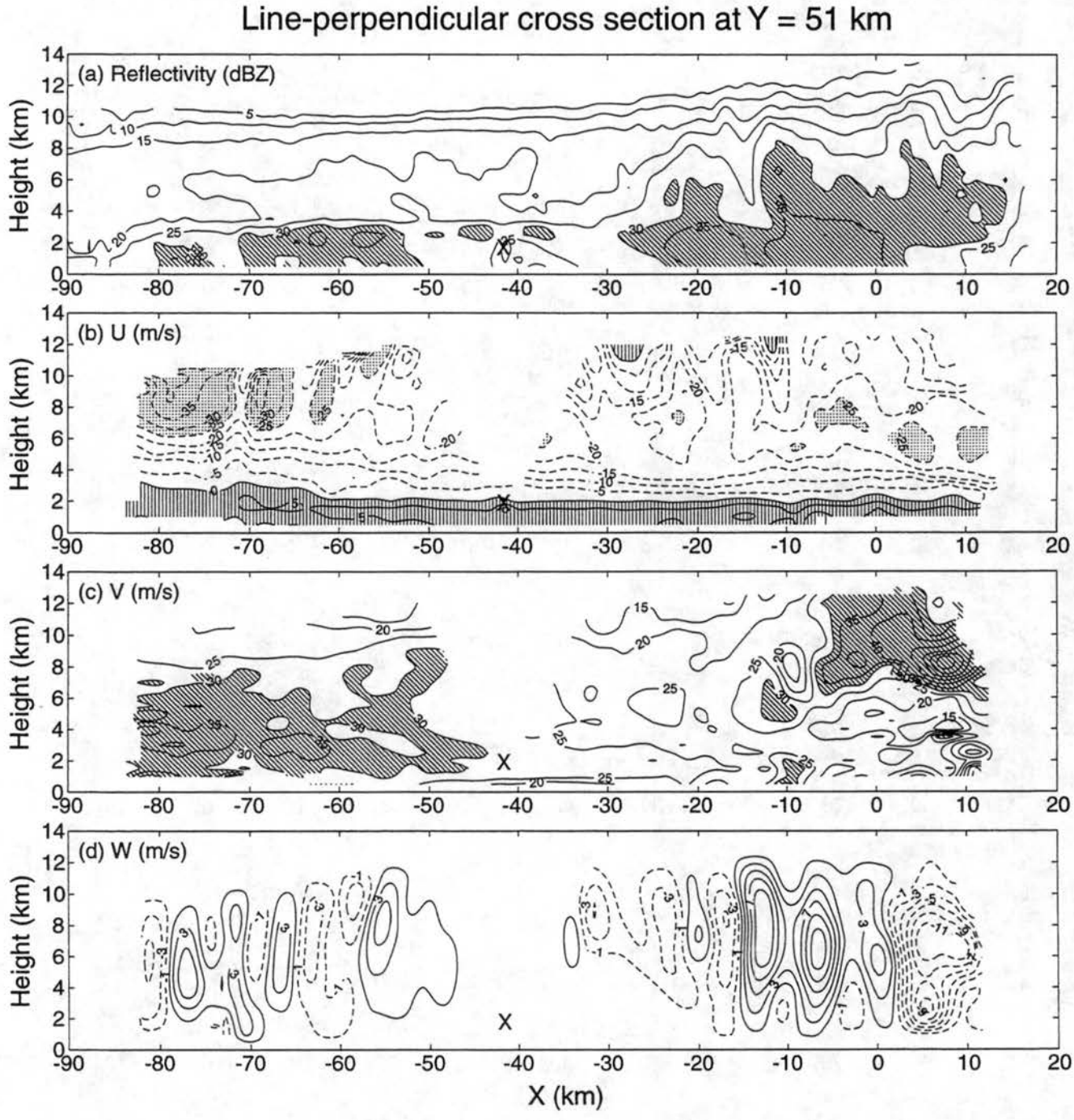

Figure 4.6: As in Fig. 4.4 except along $Y = 51$ km.

elevation angles of the radar through this region, reliable synthesis of the kinematic wind fields is not feasible. Therefore it is not possible to comment directly on the kinematic structure associated with these mid-level reflectivity minima.

To the rear of the transition zone is the secondary band of enhanced reflectivity centered near $X = -60$ km. These cross sections depict a much less homogeneous secondary band structure than shown in the mean cross section of reflectivity (Fig. 4.3a). Areas of enhanced reflectivity (up to 44 dBZ) associated with the bright band are observed intermittently throughout the secondary band region near $Z = 2.5$ km. The lack of a continuous bright band indicates that this secondary band structure is much less mature than that observed by other researchers documenting squall lines (e.g., Smull and Houze 1985; Rutledge et al. 1988).

Below the bright band are located regions of enhanced precipitation often referred to as "fallstreaks" (e.g., Battan 1973; Yuter and Houze 1997). These fallstreaks are observed throughout the secondary band region (e.g., at $X = -70$ km in Fig. 4.4a), and are often co-located under regions of enhanced reflectivity associated with the bright band (e.g., near $X = -55$ km in Fig. 4.5a). One explanation for these fallstreaks is precipitation induced from decaying convective cells being advected into the secondary band region. A possible decaying convective cell-generated fallstreak can be seen near $X = -40$ km in Fig. 4.4a. Throughout the squall line, these fallstreaks can be seen bending with the low-level windshear (i.e. sloping downward toward the convective line).

4.2.2 The U-component flow

Within the low-level RTF flow, there are areas of enhanced flow observed near convective cells (e.g., at $X = 0$ in Fig. 4.5b). These flow features are likely due to downdraft-related outflow at lower levels which can enhance or weaken (depending on direction of the outflow) the RTF flow.

Also documented here are upper-tropospheric regions of RTF flow in the convective-line region (e.g., at $X = 0$ km in Fig. 4.5b). These features are the result of strong upper-level divergence that occurs at the tops of the convective updrafts. Localized maxima of upper-

tropospheric FTR flow are noted to correspond to the downwind side of the convective-scale updrafts. Heymsfield and Schotz (1985) documented similar upper-tropospheric features near deep convection.

Enhanced regions of low and mid-level FTR flow are generally co-located near convectively active cells (e.g., at $X = 5$ km in Figs. 4.4a and 4.4b), consistent with SH. LeMone (1983) documented a similar juxtaposition between U and convective-scale updrafts observed in a line of tropical cumulonimbi. LeMone demonstrated this relation to be the result of hydrostatically induced low-pressure perturbations accelerating air parcels rearward. The negative pressure perturbations were observed to form beneath warm rearward sloping updraft cores.

Throughout the secondary band U field there are localized regions of enhanced RTF flow present (e.g., at 2 km near $X = -80$ km in Fig. 4.5b). Aloft, one also observes maxima in the FTR flow centered near $Z = 9$ km. These enhanced FTR features (and their possible association with lower-level RTF flow features observed here) will be discussed further in Section 4.3 of this Chapter.

4.2.3 The V-component flow

In the convective-line region, a widely variable V flow is observed. Localized regions of enhanced V are present at mid-levels of the convective-line region (e.g., Fig. 4.5c at $X = -10$ km). These maxima in V (in some locations >50 m s^{-1}) are located near vigorous convective cells through the mid and upper troposphere.

Newton (1966) documented areas of enhanced flow around high reflectivity cores of thunderstorms that formed in a strongly sheared environment. Perturbations up to ~25 m s^{-1} in the horizontal winds at mid and upper-levels of the troposphere were noted. Newton observed that these flow perturbations were similar to patterns of velocity around cylindrically-shaped obstacles in wind tunnels. He speculated that similar Bernoulli-type accelerations could be occurring here with the updrafts acting as cylinders in the flow. Bluestein et al. (1993) observed similar accelerations in the system-relative flow, near high-

reflectivity cores, at upper-levels of the troposphere in the convective region of a squall line.

Rotunno and Klemp (1982) proposed that the interaction of the vertical wind shear and updraft cores could lead to perturbation pressure patterns in which the resultant pressure gradient lay oriented parallel to the vertical shear vector. Although not shown here, preliminary analysis of the retrieved perturbation pressure field reveals pressure gradients within the vicinity of updraft cores oriented orthogonal to the mid-level vertical wind shear. A pressure perturbation orientation such as this suggests that the Rotunno and Klemp mechanism probably does not explain the observed accelerations of the winds at mid and upper-levels within this squall line.

Through the secondary band region, the overall variability in the along-line flow decreases. A jet-like maximum in V is located near $Z = 3$ km at the leading edge of the secondary band region, and is observed to increase in magnitude, while ascending in altitude, towards the rear of the secondary band. Significant erosion of the reflectivity field is observed to be correlated with the jet-like maxima in V (between $X = -70$ and -80 km in Figs. 4.4a, 4.5a and 4.6a), suggesting advection of drier air and/or weaker reflectivities from the south may be contributing to this feature.

Within the secondary band, melting of ice particles falling from the upper-level cloud produces cooling below the 0° isotherm (e.g., Leary and Houze 1979). This resultant "melting" layer can extend down over 1 km in depth (Stewart 1984) as melting ice particles continue to cool the air below. Harrold and Browning (1967) and Atlas et al. (1969) documented mesoscale fluctuations in winds co-located with the melting layer. Atlas et al. (1969) attributed these enhanced winds to pressure perturbations induced by melting. These perturbations in the wind were noted to be in the direction of the general wind flow associated with the melting layer. Szeto et al. (1988a,b) used a two-dimensional hydrostatic model to verify that cooling by melting and evaporation within stratiform precipitation can induce significant mesoscale perturbations in the wind fields. Throughout the secondary band region (between $X = -60$ and -70 km) there are localized maxima in V (e.g., Figs. 4.4c, 4.5c and 4.6c) that are apparently co-located with the melting layer (located below $\sim$3 km).

It is possible that this jet-like feature is being enhanced within the melting layer associated with the secondary band. Blackadar (1957) noted that the maxima in the low-level jet tended to be located near the top of the boundary layer inversion. A similar correlation is noted here between the area of enhanced flow and the region of enhanced reflectivity (indicating the approximate top of the melting-induced inversion layer) within the secondary band region. What causes this jet-like feature to slope upwards towards the rear is unclear at this time.

4.2.4 Vertical Motion

Updrafts of a variety of magnitudes are observed at various elevations throughout the the convective line. Closer inspection of the convective-line region reveals that updrafts associated with younger convective cells tend to be centered at mid-levels closer to the leading-line edge, while updrafts associated with mature cells are often centered at higher elevations farther to the rear. This ascending pattern of updrafts is consistent with that observed by Yuter and Houze (1995c). The updrafts through the convective-line are also documented to be upright in orientation. Lower-spatial-resolution compositing of these individual updrafts, located at ascending heights within the convective line, and downdrafts led to the coarsely resolved rearward-tilted updraft structure observed in Fig. 4.3e. It is possible that previously observed rearward-tilted updraft structures (e.g., Roux 1988; Biggerstaff and Houze 1991a; 1993) could have been due to the lower-resolution radar sampling of the convective-line draft structure.

The strength of the compensation downdrafts within the convective line is impressive. Near $X = -5$ km in Fig. 4.5d there is a downdraft that extends down through the upper and mid-troposphere. The highest magnitude associated with this downdraft (up to 17 m s^{-1}) is located near $Z = 10$ km. A careful analysis of horizontal wind data shows this downdraft to be forced by upper-level divergence/convergence associated with air emerging from convective updrafts. These emerging plumes of air interact with other convective outflows and slower moving ambient air to provide convergence which, when in the presence of the stable tropopause layer, results in forced descending motion (Heymsfield and Schotz

1985; Knupp 1987; SH; Biggerstaff and Houze 1993; Braun and Houze 1994). Near $Z = 3$ km this downdraft has another maxima (up to 4 m s^{-1}), apparently induced by evaporation and precipitation drag associated with the mature convective cell precipitation present here. These lower-tropospheric precipitation driven downdrafts appear throughout the convective-line (e.g., $X = -3$ and -10 km in Fig. 4.6d).

There are also regions of deep descending motion that make their way down through the entire troposphere (e.g., at $X = -16$ km in Fig. 4.5d). These features appear to be dynamically forced through the upper- and midtroposphere, and are co-located with areas of decreased reflectivity at lower levels. This could be an indication that cooling induced by sublimation and evaporation is supporting these downdrafts through the mid and lower-troposphere (Brown 1979). Though observed at much smaller horizontal scales in this squall line, these downdrafts match the general structure that Biggerstaff and Houze (1993) documented within the region of mesoscale descent associated with the transition zone of the 10–11 June 1985 squall line.

The secondary band region also shows wide variability in the vertical motion field, but with weaker magnitudes than that observed in the convective line. No obvious meso-scale updraft/downdraft couplet is observed in any part of the secondary band region as noted in the mean cross section of vertical motion (Fig. 4.3e). Instead many small-scale updraft/downdraft couplets are observed throughout this region. Yuter and Houze (1995a) documented similar results while analyzing high-resolution radar data taken through the stratiform decay associated with a line of Florida cumulonimbi.

Johnson and Kriete (1982) documented the existence of neutral to weakly conditionally unstable (to ice adiabatic ascent) regions in stratiform anvils of tropical MCSs. They termed the process Cooperative Instability Mechanism (CIM) by which cloud processes (such as melting and evaporation at low-levels and condensation, and freezing at upper-levels) can drive cloud circulations that can lead to feed-back mechanisms which could enhance cloud growth. This process would lead to convective-scale ($\sim$5 to 10 km) updrafts and downdrafts due to the conditional instability. However, because there were no soundings launched within

the secondary band region, one can only speculate about a process such as CIM is at work within this squall line.

Rearward advection of decaying convective cells and processes such as CIM could account for the vertical motion structure observed within the secondary band. However, as additional cross sections (not shown) were examined, a periodic nature to the vertical motion field became apparent. In addition, there is a pattern of updraft and downdraft couplets observed throughout the secondary band (e.g., near $X = -58$ km in Fig. 4.5d). The coupling and periodicity noted in the vertical motion field are possible gravity wave signatures. Evidence for these gravity wave oscillations is examined in the next section.

4.3 MEAN high-resolution cross sections

To summarize a portion of the high-resolution view of this squall line, the mean two-dimensional structure of this squall line, along-line averaged profiles of the reflectivity and kinematic fields are presented. Figure 4.7 documents the line-normal view averaged over 30 km of the line from $Y = 5$ km to $Y = 35$ km on the horizontal plot of the line (Fig. 4.1). Due to the software limitations of CEDRIC, only 30 km of the high-resolution ELDORA data can be averaged. Most of the variability observed within the individual cross sections (Figs. 4.4, 4.5 and 4.6) has been filtered out by this averaging process (but not to the extent that filtering was done within the mean reduced-resolution cross sections).

Mean high-resolution cross sections of reflectivity (Fig. 4.7a), U (Fig. 4.7b), and V (Fig. 4.7c) have the same general features that were observed in the mean reduced-resolution cross sections (Figs. 4.3a-c).

Figure 4.8 shows the KFDR, Oklahoma Velocity-Azimuth Display (VAD) (Browning and Wexler 1968) derived U (Fig. 4.8a) and V-components (Fig. 4.8b) of the system-relative horizontal flow. A space-time conversion (Fujita 1955) and rotation have been applied to these data to match that of the squall line reference frame (as documented in Chapter 2). The comparison to the region observed by ELDORA would be between $X = 0$ km and -100 km in Fig. 4.8. Though these data are only valid through $\sim$8 km of the lower and middle troposphere, they provide independent confirmation of the horizontal flow features observed

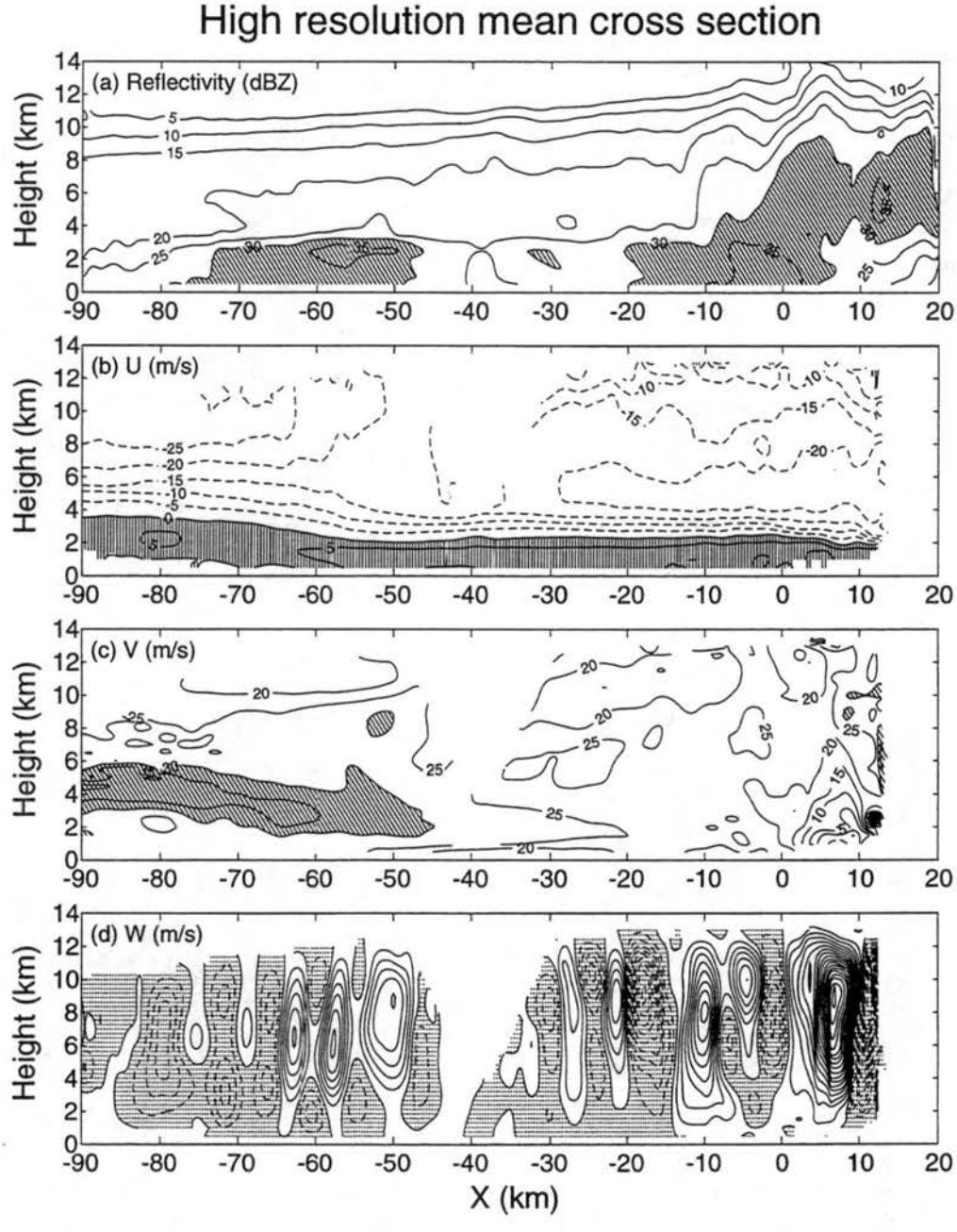

Figure 4.7: MEAN high-resolution cross section over 30 km of the squall line from $Y = 5$ to 35 km showing (a) reflectivity (dBZ) contoured every 5 dBZ, (b) U contoured every 5 m s^{-1}, (c) V contoured every 5 m s^{-1}, and (d) vertical velocity contoured every 0.5 m s^{-1}. In (a), hatching indicates reflectivity >30 dBZ. In (b), negative contours are dashed, vertical hatching indicates positive (RTF) flow. In (c), negative contours are dashed and hatching indicates flow >30 m s^{-1}. In (d), negative contours are dashed and shaded regions indicate negative vertical velocities.

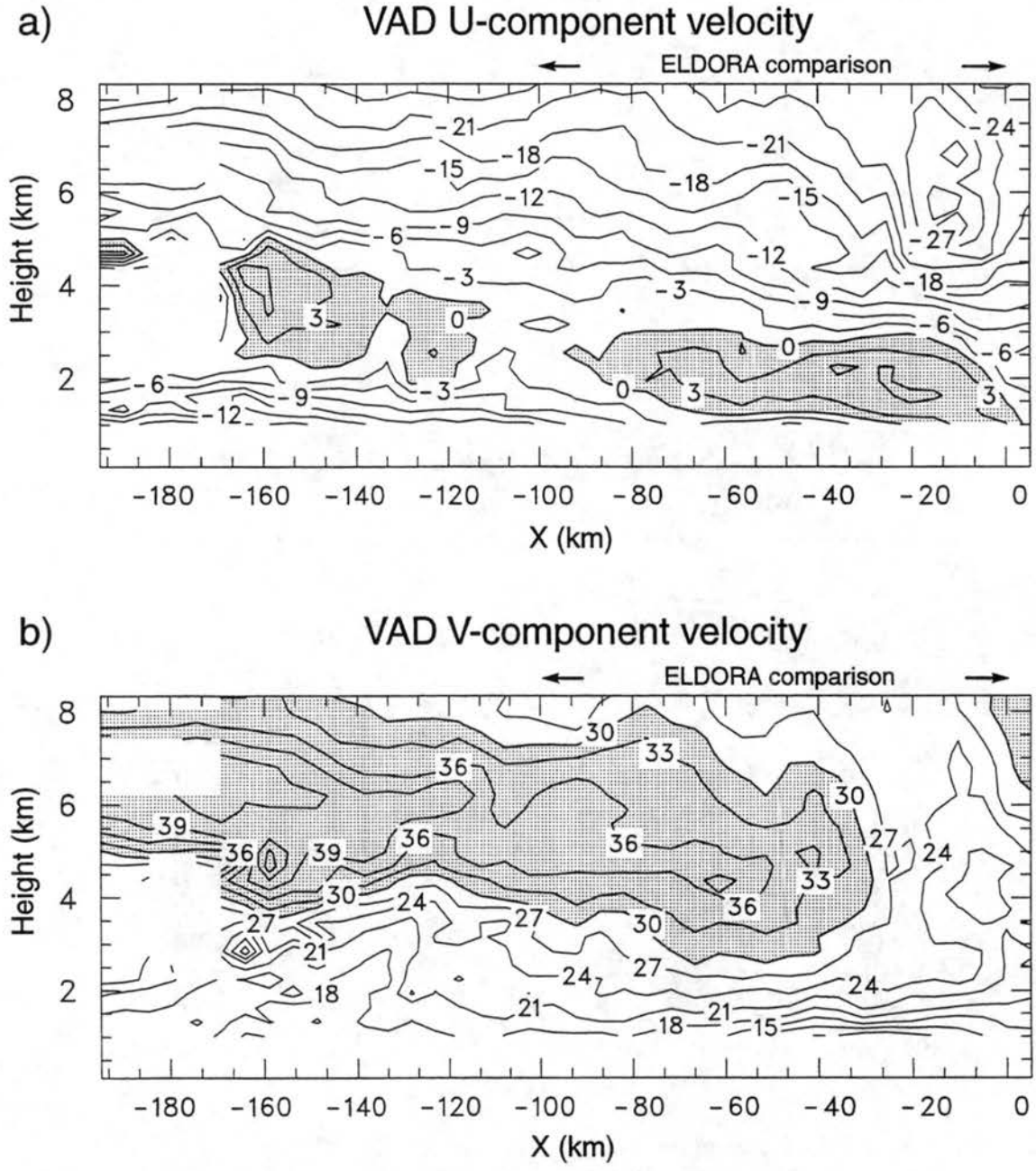

Figure 4.8: KFDR VAD derived components of system relative winds. (a) U-component velocity (shaded region denotes RTF flow). (b) V-component velocity (shaded region denotes $V > 30$ m s^{-1}).

by ELDORA. VAD observed U-component features (Fig. 4.8a) include a descending RTF flow (with a maximum of $\sim$7 m s^{-1} near $X = -30$ km) and an ascending FTR flow with a maxima of ~ -30 m s^{-1} near $Z = 6$ km. A general weakening of the RTF flow is noted near $X = -100$ km. These observed VAD U flow features match well with the general ELDORA U observations (e.g., Fig. 4.7b).

Figure 4.8b shows the VAD derived V-component flow features. A minima is located in the VAD V-component near $X = -10$ km and a jet-like feature is observed centered near $Z = 4$ km at $X \leq -40$ km. The jet-like feature has a maximum magnitude of $\sim$30 m s^{-1}; which corresponds well with the line-averaged V–component velocity shown in Fig. 4.7c. It must be noted here that these VAD derived components of the horizontal flow fields are a time-series of observations from a single point. These observations of $X < -100$ are from over an hour after the time of the dual-Doppler synthesis. The possible evolution of such features observed in the VAD data (such as this jet-like feature in V) must be considered in any comparison with the ELDORA data. With this time-dependence in mind, one observes the jet-like feature to increase in strength and increase in elevation. One might speculate that this jet-like feature is connected with the larger synoptic circulation associated with the upper-level low west of the squall line (Chapter 3).

The line-averaged vertical motions (Fig. 4.7e) depict a very discrete, periodic structure to the vertical motion field (contoured every 0.5 m s^{-1}) that is evident well into the secondary band region of this squall line. Though averaging over only 30 km of this squall line has influenced this structure, this profile of vertical motion strongly resembles that of a gravity wave signature which have been documented in recent modeling studies (e.g., Alexander et al. 1994; Yang and Houze 1995; Pandya and Durran 1996; Fovell and Tan 1998).

Figure 4.9 depicts the time-averaged vertical velocity field from Pandya and Durran's (1996) simulation of a squall line. One notices prominent modulation of the vertical velocity field near $X = -140$ km in Fig. 4.9a. Closer to the leading line, the time-averaging process has revealed a broad region of mesoscale ascent overlying a region of mesoscale descent. Pandya and Durran attribute this periodic nature of the vertical velocity field to the generation of high-frequency gravity waves induced by the thermal forcing within the

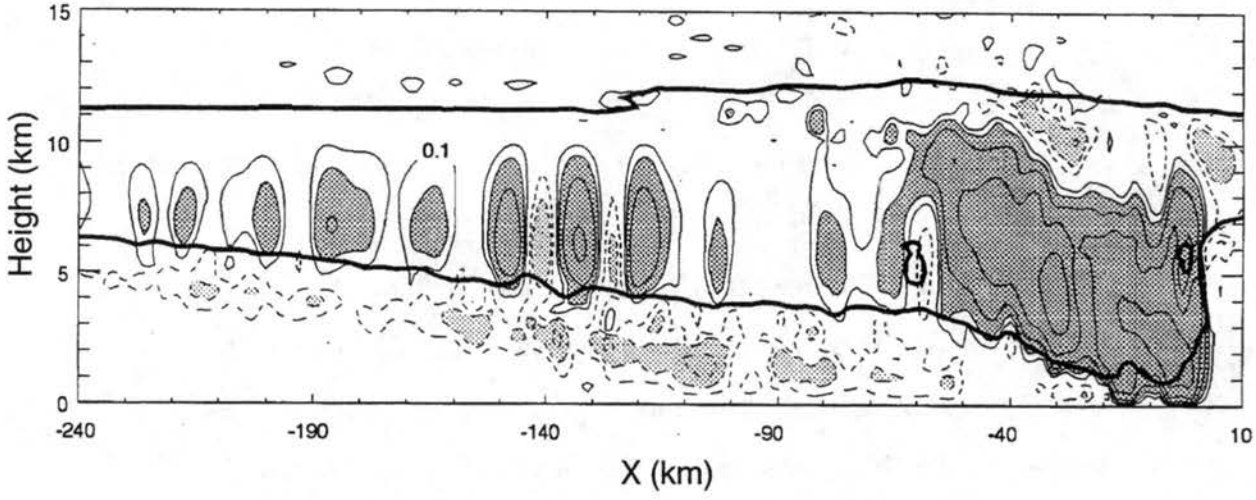

Figure 4.9: Figure of time-averaged vertical velocity contoured every 0.2 m s^{-1}. Dark contour represents the cloud outline. (from Pandya and Durran 1996)

convective line. One might conclude that to notice such a signal in the vertical velocity field, after a two-hour time-averaging procedure, that the instantaneous cross sections must have shown significant variability in the vertical motion field. There were no instantaneous cross sections of vertical velocity presented by Pandya and Durran in their work.

Figure 4.10 shows two cross sections from a two-dimensional ice-free squall line simulation by Robert Fovell (personal communication) employing the fully compressible ARPS (Advanced Regional Prediction System, Xue et al. 1995) model. This simulation uses the D = 2.5 shear profile (see Fovell and Daily 1995; Fovell and Tan 1998) using ARPS (as in Fovell and Tan 1998) only with much higher resolution. A grid spacing of $\Delta x = 250$ m is used with a domain of 500 km in width employed for the model region. Only a small portion of the domain is depicted in these cross sections. Reliable wavelengths resolved by this model simulation are $\geq$2 km.

Figure 4.10a is a snapshot of the vertical velocity field and potential temperature perturbations present at $t = 4.5$ hours into the simulation. Emphasized here are the periodic gravity wave features observed propagating rearward (as updraft/downdraft couplets) from the leading-line convection (e.g., near $X = 182$ km). The phase relationship that these gravity wave features possess with the perturbation potential temperature field is also doc-

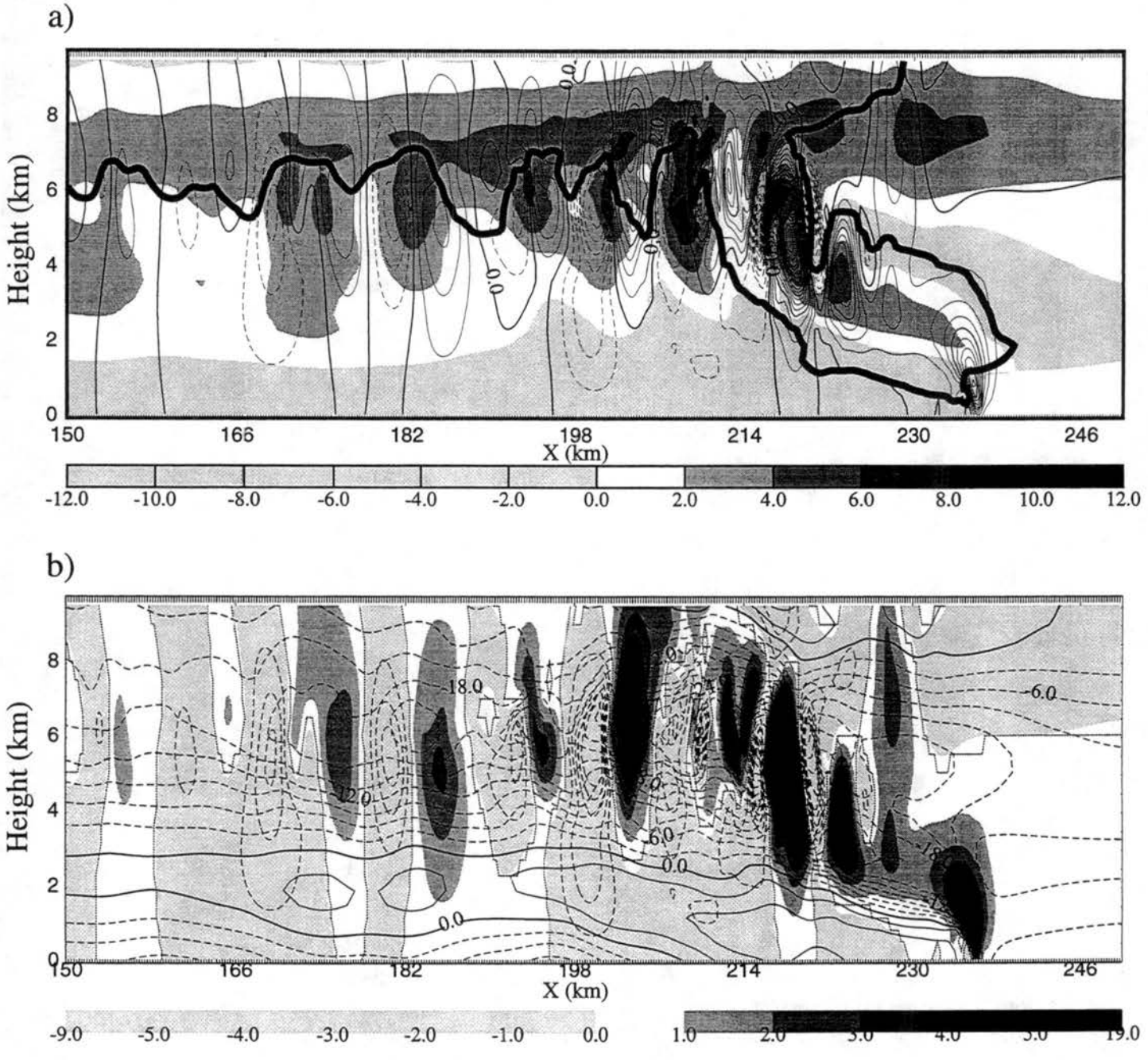

Figure 4.10: Figures of a 2D ice-free simulation of a squall line at $t = 4.5$ hours into the simulation. (a) The vertical velocity contoured (every 1 m s^{-1} interval) with the potential temperature perturbations shaded. (b) The system-relative U–component velocity is contoured (every 3 m s^{-1} interval) with the vertical velocity field shaded. In (a), negative potential temperature perturbations are light-shaded and and downdraft contours are dashed. In (b), negative contours are dashed.

umented here. In this relationship, maxima in potential temperature perturbations (defined as the deviation from the initial value) are centered one-quarter wavelength ahead of (to the left of) the updrafts at all levels (e.g., near $X = 182$ km). This phase relationship has been termed "quadrature." A quadrature phase relationship can also be observed between the vertical velocity field and perturbations in the line-perpendicular flow in Fig. 4.10b. The updrafts are located behind (one-quarter wavelength) a horizontal maxima in U (below) and a minima in U (above) (e.g., near $X = 182$ km).

To better illustrate the vertical motion and U quadrature relationship, a schematic of a gravity wave from Ralph et al. (1993) is shown in Fig. 4.11, which highlights the wave-induced horizontal motions and vertical motions (arrows). By mentally superimposing a low-level RTF flow and a mid and upper-level FTR flow onto the perturbation flow in Fig. 4.11, one can see that the quadrature relation observed in Fig. 4.10b is indeed valid.

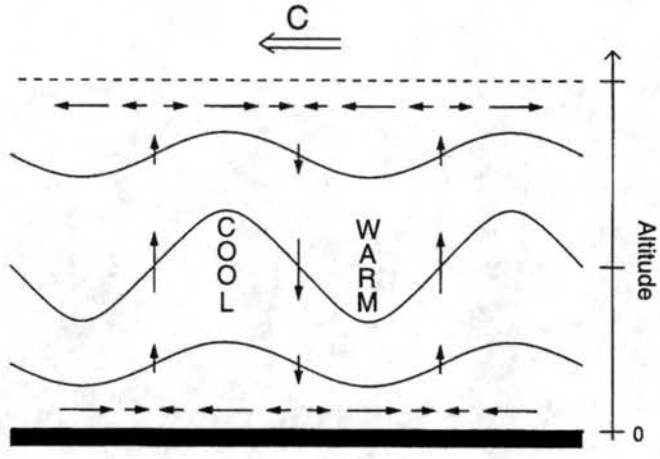

Figure 4.11: Schematic representation of a ducted mesoscale gravity wave showing wave-induced vertical and horizontal motions (arrows), streamlines or isentropes (solid lines), and the direction of wave motion (labeled C). Regions of cool and warm air created by the vertical displacements are also shown (adapted from Ralph et al. 1993).

Within the 7–8 May squall line, there exists low and upper-level perturbations within the secondary band's U field. As noted earlier, one sees similar minima and maxima perturbations in the U field. Figures 4.5b and 4.6b have maxima (below) and minima (above) in U present between $X = -70$ and -80 km. A periodic structure to the vertical motion field is also observed throughout this squall line (as exemplified by Fig. 4.7d).

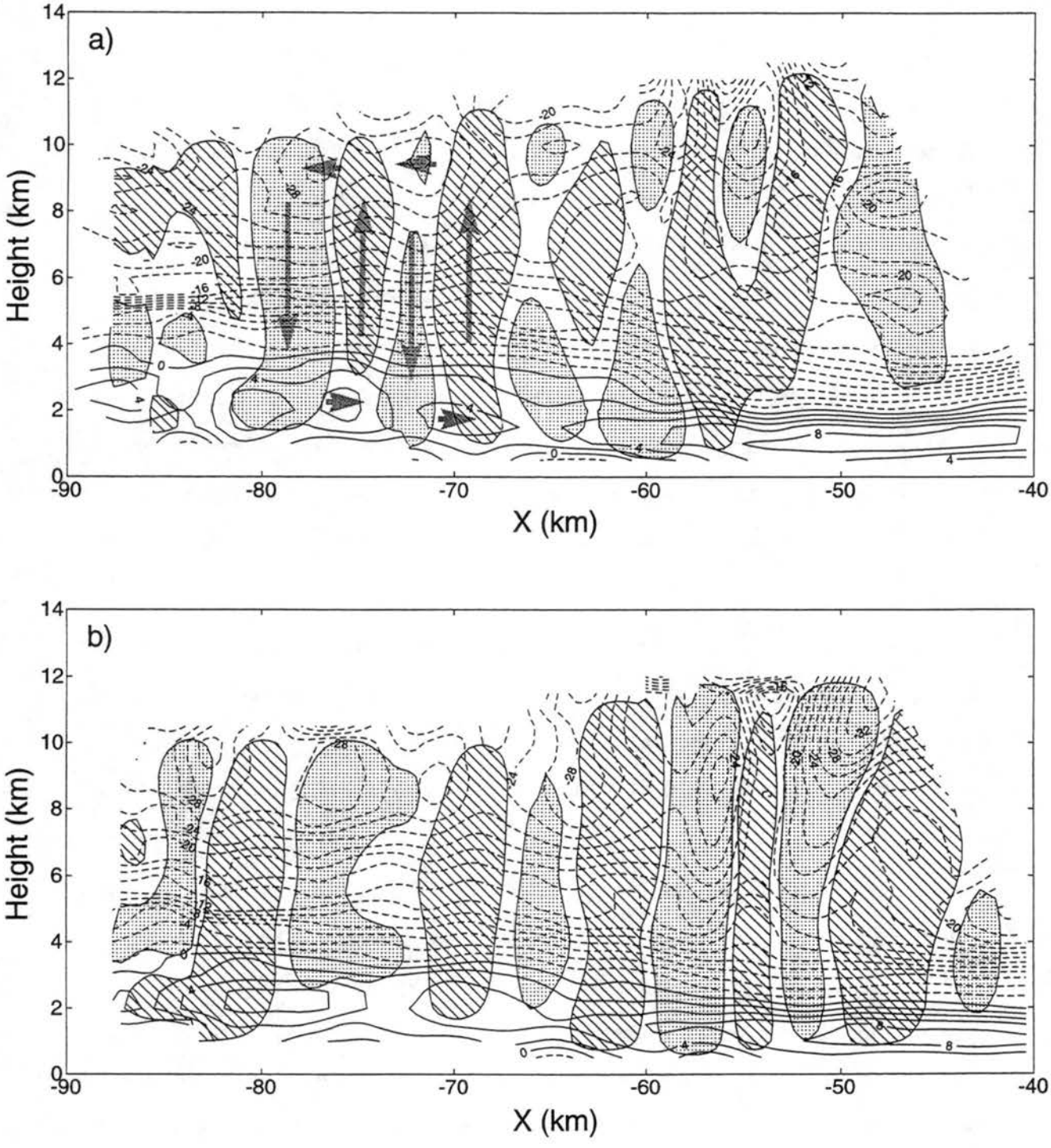

Figure 4.12: Cross section of line-perpendicular flow (U) (contoured) and vertical velocity (w) (hatched and shaded) along (a) $Y = 30$ km and (b) $Y = 41$ km. U is contoured every 2 m s^{-1} with negative contours dashed. Vertical velocity is hatched for $w > 0.8$ m s^{-1} and shaded for $w < -0.8$ m s^{-1}. Arrows in (a) highlight the quadrature relation observed within this squall line.

To highlight the correlation between vertical motion and U, a close-up on the secondary band region along cross sections centered on $Y = 30$ km (Fig. 4.12a) and $Y = 41$ km (Fig. 4.12b) are shown. U (contoured) and vertical velocity (hatched and shaded) are overlayed to better understand the correlations between these two fields. There are several updrafts here that seem to be in quadrature with maxima (below) and minima (above) in U (e.g., near $X = -70$ and -75 km in Fig. 4.12a). Arrows are superimposed over the updrafts and downdrafts and the perturbations within the U field in Fig. 4.12a to highlight the observed quadrature relationship.

These small-scale gravity wave perturbations in the secondary band region represent one of the principal findings from this work. Previous observational studies have hinted at such features (e.g., SH; Keenan and Rutledge 1992; Bluestein et al. 1993), but the ELDORA's high-resolution data have afforded the first real opportunity to observe these features in detail.

General characteristics of these gravity waves observed include wavelengths of 5-10 km and amplitudes of 2-5 m s^{-1}, which are very similar to the wavelengths and amplitudes of the gravity waves predicted in the modeling simulation (Fig. 4.10). Within these gravity waves, easterly momentum transport downward and westerly momentum transport upward are observed.

It should be noted, that the use of real data, and the inherent three-dimensionality of these gravity waves, complicates interpretation of the radar data in terms of the simple two-dimensional model represented by Fig. 4.11. In particular, rather than parallel to the convective line, the gravity wave fronts observed here are oriented at angles to the convective line (Fig. 4.19, later), thus complicating their interpretation, particularly in relation with two-dimensional modeling results. In addition, processes occurring within the secondary band which could induce vertical motions (such as CIM and rearward advected decaying convection) could be disrupting the gravity wave observations. Further evidence supporting the possible three-dimensional nature of these gravity wave features will be explored in Section 4.5.2.

4.4 Close-up on the convective-line region

In this section the three-dimensional relationship between radar reflectivity, horizontal wind and vertical motion is explored by examining both horizontal and line-parallel cross sections through the convective-line region. Outlines for these cross sections are documented in Fig. 4.1.

4.4.1 Convective-line low-level patterns

The low-level (1.5 km) reflectivity field (Fig. 4.13a) is dominated by values greater than 30 dBZ, and areas of enhanced RTF flow (Fig. 4.13b) are noted to be co-located near the highest reflectivity cores. Wide variability is present in the V field (Fig. 4.13c) with some regions of negative V present that are associated with the divergent flow from convective-scale downdrafts. Figure 4.13d shows that the 1.5 km horizontal storm-relative flow is directed mostly in an along-line direction.

4.4.2 Convective-line mid-level patterns

At $Z = 7$ km (Fig. 4.14), as noted earlier, one observes a close correlation between the maxima in reflectivity (Fig. 4.14a) and extrema in U (Fig. 4.14b) and V (Fig. 4.14c). By examining the relationships of U, V, and reflectivity, one observes that the maxima in U and V seem to be located around the edges of the high-reflectivity cores. This correlation of wind and precipitation would seem to support the idea of Bernoulli-type accelerations of the flow are occurring within the convective-line region.

The vertical velocity field (Fig. 4.14d) emphasizes the wide variability present. Many updraft/downdraft couplets are present throughout the convective-line region. There are hints of banded structures present within the convective motion field. These structures will be discussed further in conjunction with the secondary band vertical velocity field in section 4.5.2.

4.4.3 Convective-line-parallel cross sections

Figure 4.15a documents the reflectivity present along the line $X = 1$ km. Convective cells at what are likely three different stages of their evolution are shown. The most dynamic

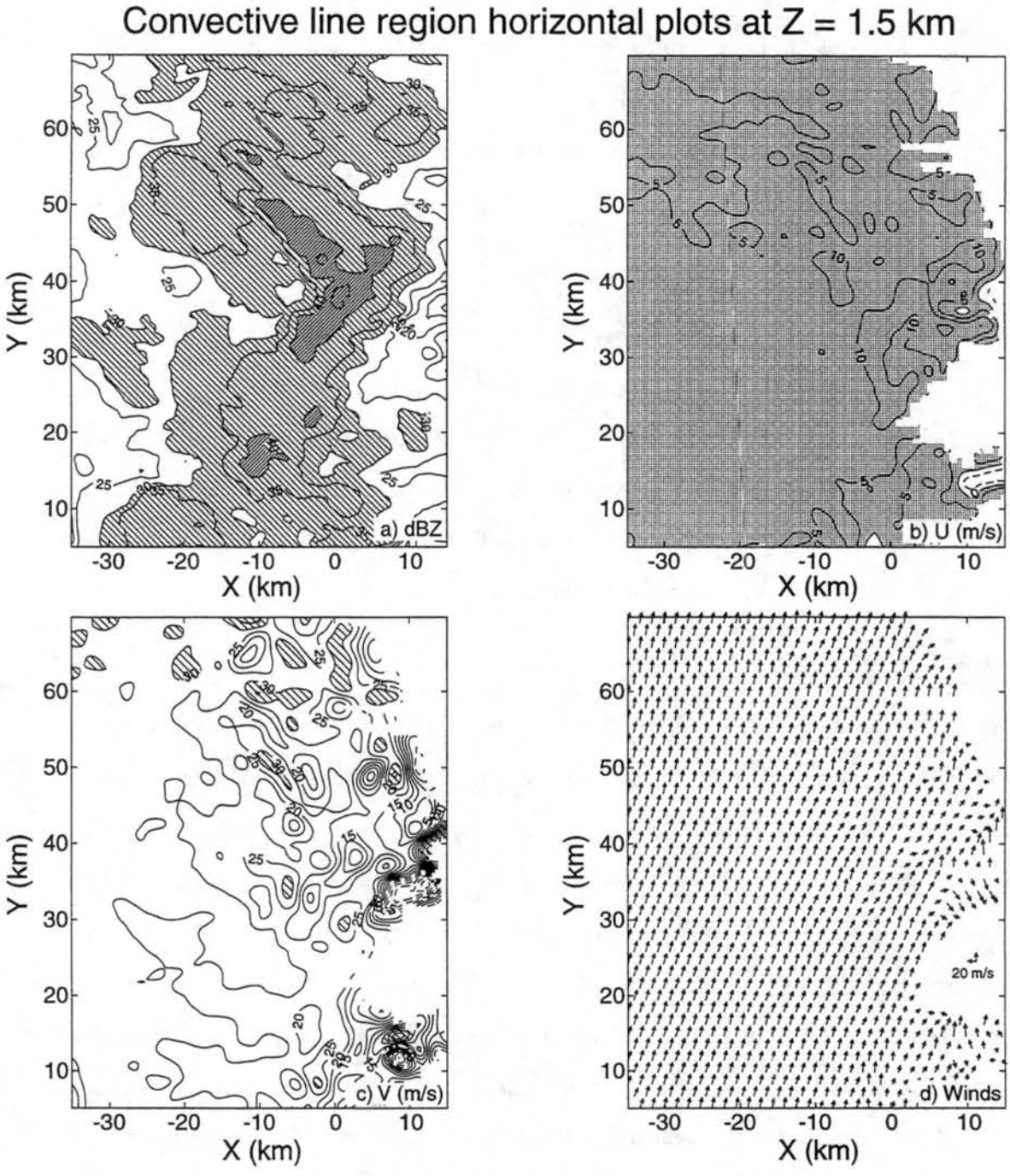

Figure 4.13: Horizontal cross sections at $Z = 1.5$ km showing (a) reflectivity (dBZ) contoured every 5 dBZ, (b) U contoured every 5 m s^{-1}, (c) V contoured every 5 m s^{-1}, and (d) horizontal system-relative winds. In (a), light hatching indicate reflectivity >30 dBZ and dark hatching indicate reflectivity >40 dBZ. In (b), negative contours are dashed, shaded regions indicate positive U (RTF) flow. In (c), negative contours are dashed and hatching indicates flow >30 m s^{-1}.

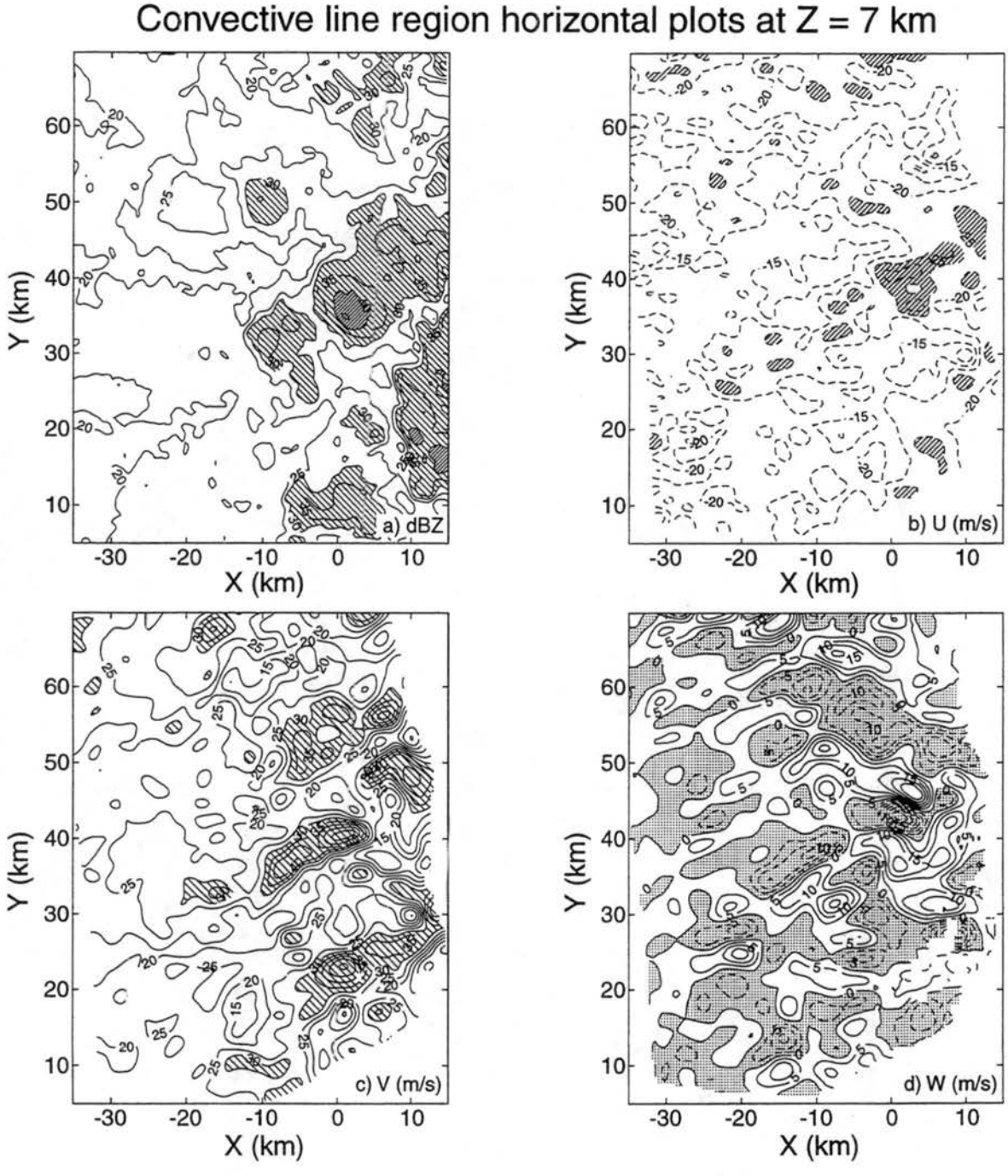

Figure 4.14: Horizontal cross sections at $Z = 7$ km showing (a) reflectivity (dBZ) contoured every 5 dBZ, (b) U contoured every 5 m s^{-1}, (c) V contoured every 5 m s^{-1}, and (d) vertical velocity contoured every 5 m s^{-1}. In (a), light hatching indicate reflectivity >30 dBZ and dark hatching indicate reflectivity >40 dBZ. In (b), negative contours are dashed, hatched regions indicate negative U (FTR) flow <25 m s^{-1}. In (c), negative contours are dashed and hatching indicates flow >30 m s^{-1}. In (d), negative contours are dashed and downdrafts are shaded.

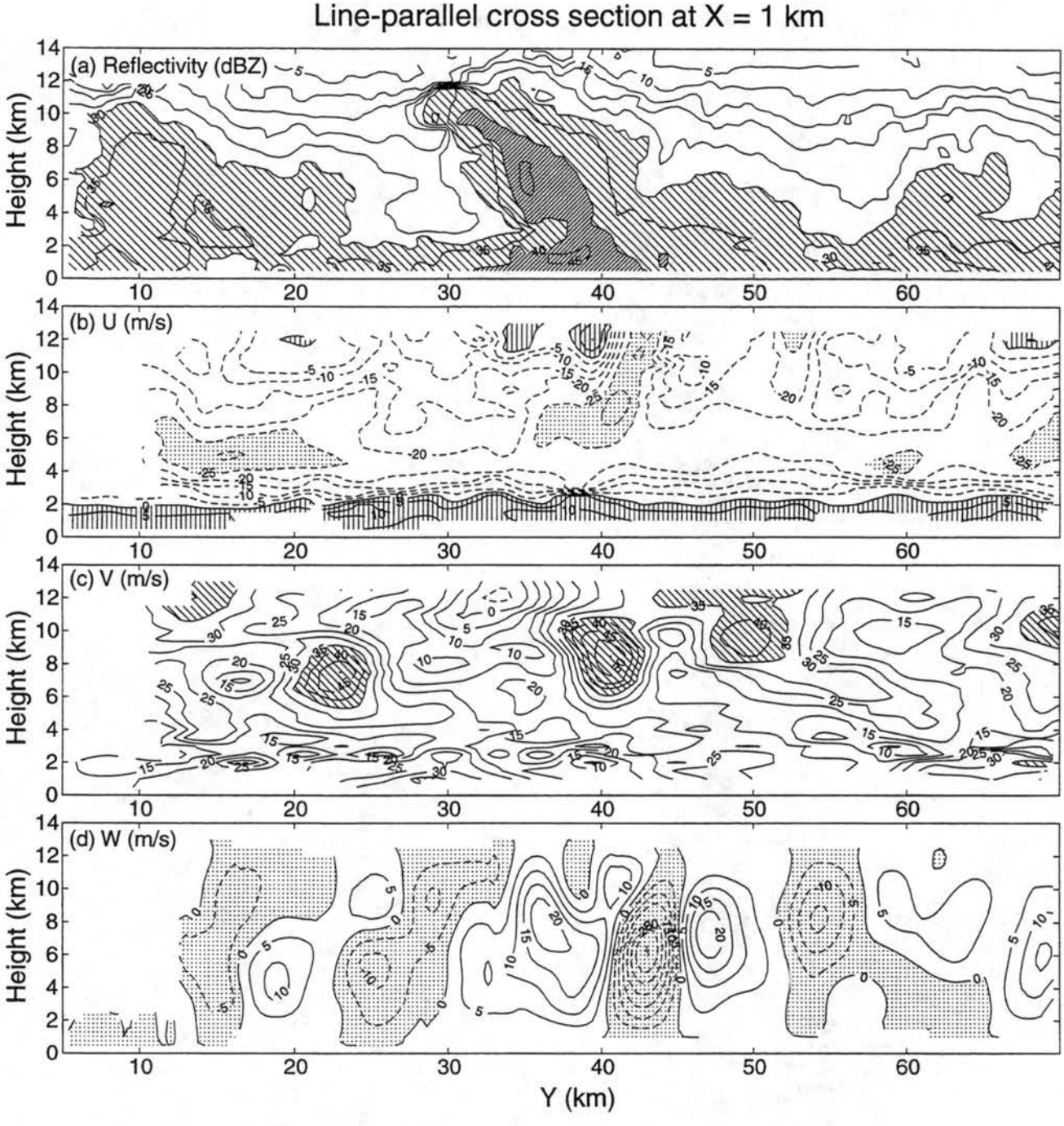

Figure 4.15: Line-parallel cross section along $X = 1$ km showing (a) reflectivity (dBZ) contoured every 5 dBZ, (b) U contoured every 5 m s^{-1}, (c) V contoured every 5 m s^{-1}, and (d) vertical velocity contoured every 5 m s^{-1}. In (a), light hatching indicate reflectivities >30 dBZ and dark hatching indicate reflectivities >40 dBZ. In (b), negative contours are dashed, vertical hatching indicates positive U (RTF) flow and shading indicates negative U (FTR) flow <-30 m s^{-1}. In (c), negative contours are dashed and hatching indicates flow >30 m s^{-1}. In (d), negative contours are dashed and downdrafts are shaded.

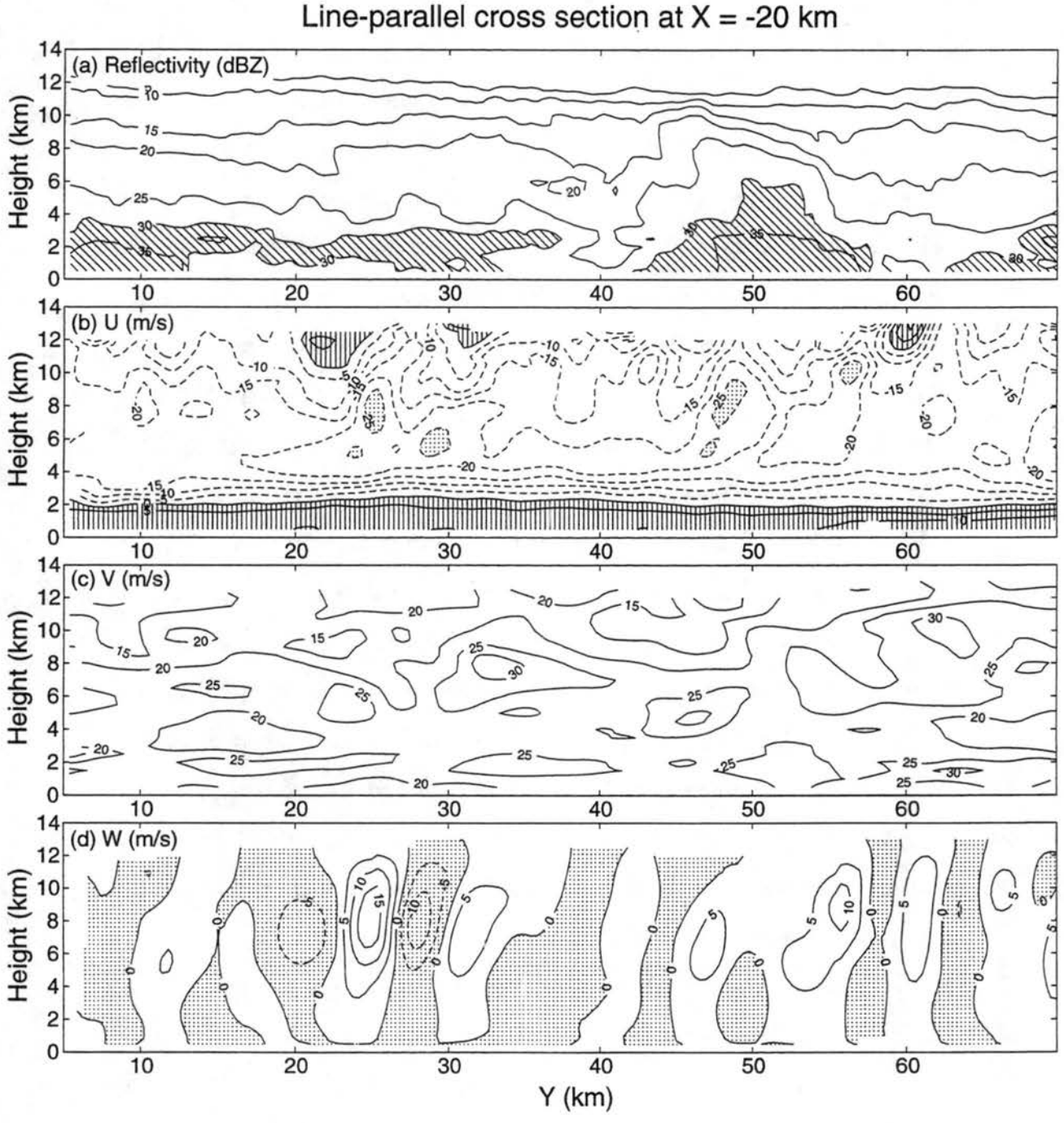

Figure 4.16: As in Fig. 4.15 except along $X = -20$ km.

cell is located near $Y = 35$ km, with an elevated region of reflectivity (>40 dBZ) extending to $Z = 10$ km. The odd tilt of this cell is due to the location of the cross section taken. Convective cells of weaker strength are located at $Y = 10$ and 63 km. Between the cells are regions of reflectivity minima (near $Y = 30$ and 55 km). The U flow (Fig. 4.15b.) emphasizes RTF flow below $Z = 2$ km, with FTR flow present above. Maxima in low-level RTF flow are generally observed to be located under convective cells (e.g., at $Y = 40$ km). Areas of enhanced FTR flow centered at mid-tropospheric levels are roughly co-located with the convective cells. Through the upper-troposphere, areas of RTF flow, associated with diverging air from convective-scale updrafts, are observed.

The cross section of the V flow (Fig. 4.15c) emphasizes an alternating pattern of maxima and minima centered at $Z = 7$ km near $Y = 20$ km ascending to $Z = 9$ km near $Y = 65$ km. These minima and maxima in V are further evidence of the Bernoulli-type perturbations to the flow present within the convective line.

The vertical velocity field (Fig. 4.15d) along this stretch of the squall line is dominated by an updraft/downdraft couplet regime. Stronger convective-scale updrafts are correlated with the convective cell in the center of the cross section ($Y = 35$ km), while weaker updrafts are correlated with the weaker cells located at $Y = 10$ and 60 km. The updraft centered near $Y = 48$ km is the rear edge of a strong updraft connected with a convective cell located closer to the leading edge of this line. Regions of deep-descending motion are observed to be correlated with the regions of reflectivity minima near $Y = 30$ and 55 km. A particularly strong downdraft is observed near $Y = 43$ km, and is an example of the intense compensating subsidence within the convective-line.

The cross section centered at $X = -20$ km (Fig. 4.16) highlights a much weaker part of the convective-line. Remnants of decaying convective cells are present in the reflectivity field (Fig. 4.16a) near $Y = 10$ and 50 km. Some enhancement of reflectivity associated with the melting level is noted along this cross section (e.g., near $Y = 50$ km). Noticeable reflectivity minima are observed near $Y = 40$ and 60 km along this cross section.

The U–component velocity field (Fig. 4.16b) emphasizes a much more homogeneous RTF and FTR flow through the lower-troposphere. The average vertical shear through this

interface is $\sim 10^{-2}$ m s^{-2}. Through the mid-troposphere, significant variability in the FTR flow is observed with minima less than -20 m s^{-1} centered near $Z = 7$ km all along this cross section. Aloft, localized regions of RTF flow are observed.

The V–component velocity (Fig. 4.16c) has a similar pattern of maxima and minima as that noted along the $X = 1$ km cross section, though the magnitudes are generally smaller.

The vertical motion field (Fig. 4.16d) shows a weaker pattern of convective-scale vertical velocities present. Though weaker in magnitude, a general pattern of downdraft/updraft couplets are noted along this segment of the squall line. Regions of descent are observed to be correlated with the reflectivity minima (e.g., near $Y = 40$ km).

4.5 Close-up on the secondary band region

Horizontal and line-parallel cross sections spanning the secondary band region are shown in this section. Outlines for these cross sections are documented in Fig. 4.1.

4.5.1 Secondary band low-level patterns

At $Z = 2.5$ km (Fig. 4.17a), the region of melting enhanced reflectivity is roughly outlined by the 30 dBZ contour (light cross-hatched region) with a line of higher reflectivity (>35 dBZ) centered along $X = -57$ km. The inhomogeneous structure associated with the secondary band region is well documented here.

Within the U field (Fig. 4.17b), it is noted that the transition from FTR to RTF flow (i.e., a region of convergence) corresponds well with the region of enhanced reflectivity associated with the bright band. This is an excellent example of melting induced convergence often observed within secondary bands of precipitation (e.g., Houze 1977; Gamache and Houze 1982; Mapes and Houze 1995)

Figure 4.17c depicts the V field at $Z = 2.5$ km and emphasizes the extent of the jet-like feature. An interesting note is that this jet has its maxima (>35 m s^{-1}) just rearward of the 35 dBZ contour, further suggesting that erosion of the secondary band by the jet is occurring (as noted earlier).

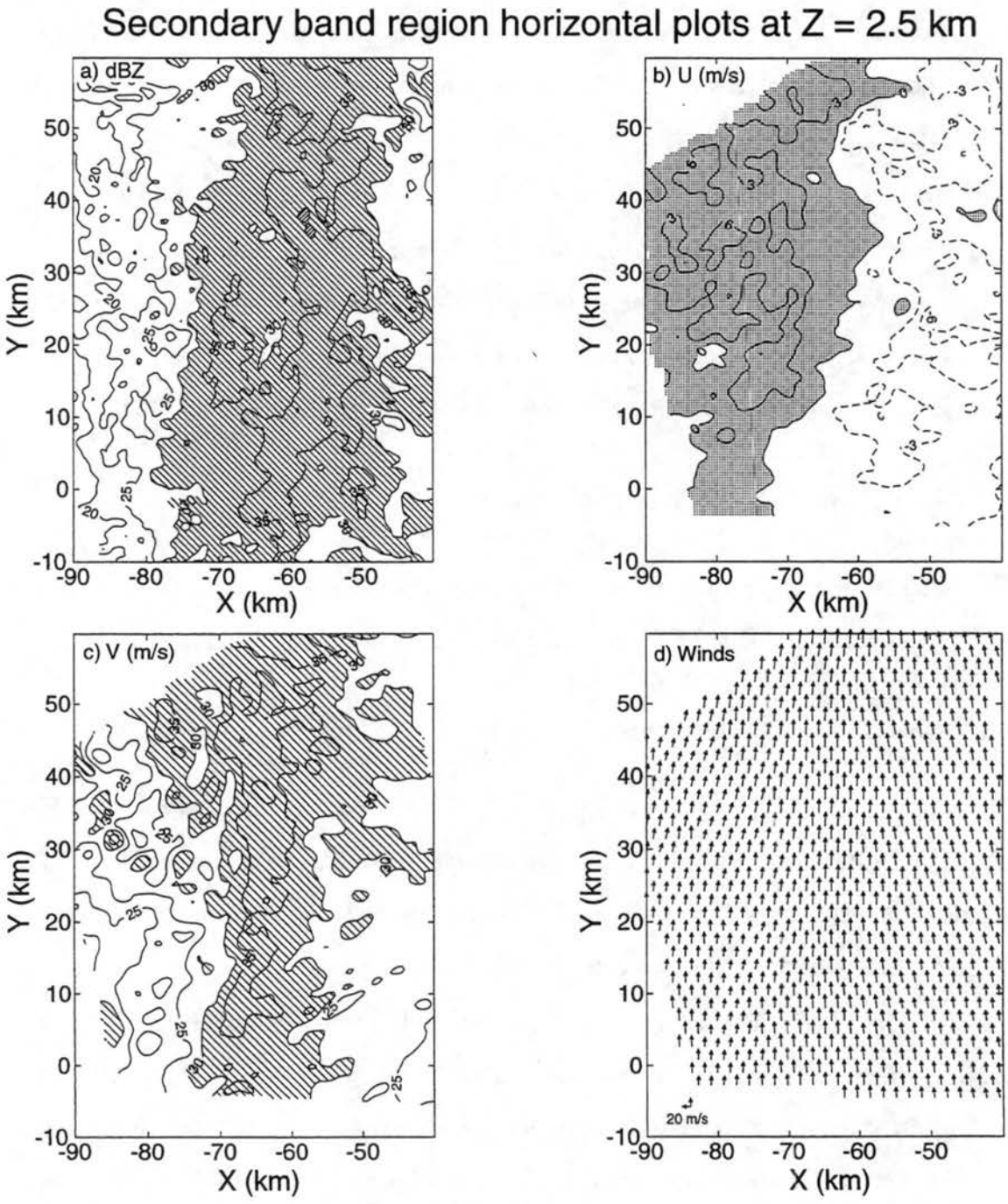

Figure 4.17: Horizontal cross sections at $Z = 2.5$ km showing (a) reflectivity (dBZ) contoured every 5 dBZ, (b) U contoured every 3 m s^{-1}, (c) V contoured every 5 m s^{-1}, and (d) horizontal system-relative winds. In (a), light hatching indicate reflectivity >30 dBZ and dark hatching indicate reflectivity >40 dBZ. In (b), negative contours are dashed, shaded regions indicate positive U (RTF) flow. In (c), hatching indicates V flow >30 m s^{-1}.

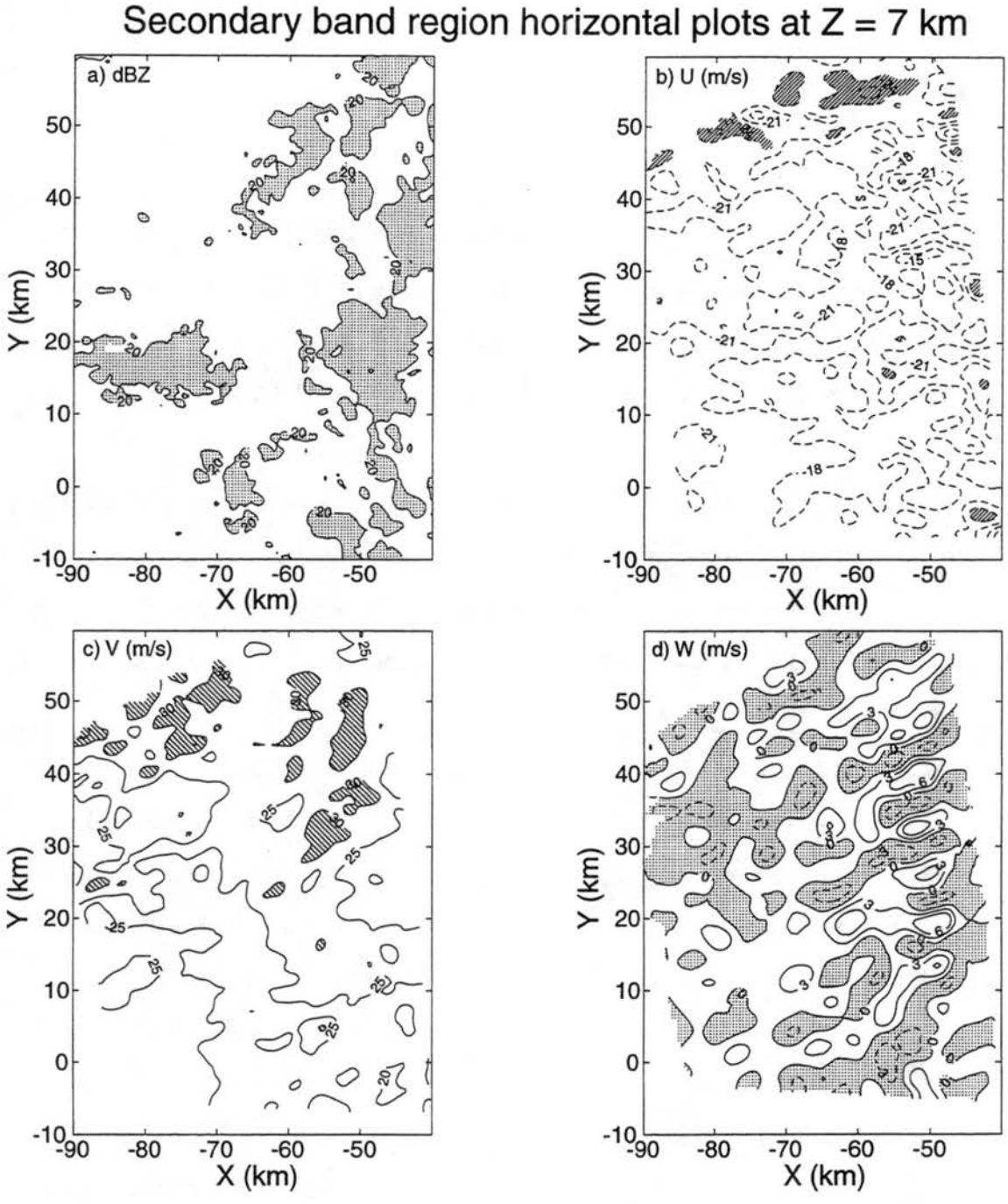

Figure 4.18: Horizontal cross sections at $Z = 7$ km showing (a) reflectivity (dBZ) contoured every 5 dBZ, (b) U contoured every 3 m s^{-1}, (c) V contoured every 5 m s^{-1}, and (d) vertical velocity contoured every 3 m s^{-1}. In (a), light shading indicates reflectivity >20 dBZ. In (b), negative contours are dashed, hatched regions indicate negative U (FTR) flow <25 m s^{-1}. In (c), hatching indicates V flow >30 m s^{-1}. In (d), negative contours are dashed and downdrafts are shaded.

Figure 4.17d shows the horizontal winds (as vectors) at $Z = 2.5$ km and emphasizes the dominance that V has on the horizontal wind field. The convergence associated with U is only slightly perceptible from this perspective.

4.5.2 Secondary band mid-level patterns

At $Z = 7$ km, only slightly variable regions of reflectivity (Fig. 4.18a) are present. The general trend is one of decreasing reflectivity with decreasing X. The U field (Fig. 4.18b) is dominated by FTR flow. Noticeable variability, that increases with increasing Y, is evident at this level. Figure 4.18c emphasizes a weaker V field than observed at $Z = 2.5$ km (Fig. 4.17c).

The vertical velocity field at $Z = 7$ km (Fig. 4.18d) reveals an interesting wave-front structure inherent to the secondary band region. The convective-line region was noted to show a similar pattern of banded features present in the vertical motion field. These patterns are similar to those observed in previous squall line studies (e.g., SH; Keenan and Rutledge 1992; Bluestein et al. 1993).

To emphasize the observed wave-front structures, Fig. 4.19 shows the system-relative horizontal flow as vectors overlayed onto the vertical motion fields for the secondary band (Fig. 4.19a) and convective-line regions (Fig. 4.19b). One can see a general wave-front pattern within the vertical velocity fields of both regions oriented perpendicular to the system-relative flow at this level. SH and Bluestein et al. (1993) observed similarly oriented wave-fronts, with respect to the mid-level flow, of vertical motion associated with squall lines. SH speculated that the wave-front structure could have developed as a response to the convective updrafts impinging upon the tropopause triggering an oscillatory response in the air at a certain equilibrium level. Another idea put forth by SH was that these wave-like features could be gravity wave responses triggered by flow ahead of the line encountering the regions of deep convectively generated cold pools.

Lin and Li (1988) modeled an elevated heat source in a sheared environment and showed that wave-fronts, consisting of thermally forced gravity waves, moved away in V-shaped patterns in the downwind direction. These V-shaped patterns of gravity waves were

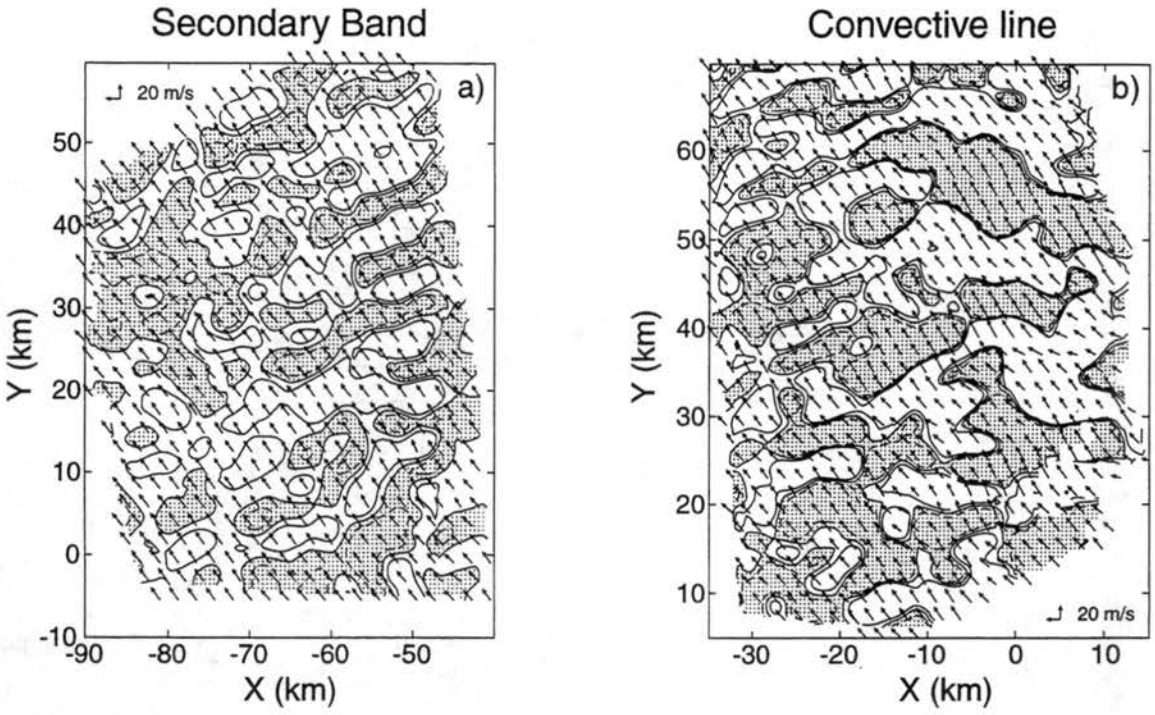

Figure 4.19: System-relative winds overlayed on the vertical motion field at $Z = 7$ km for (a) secondary band and (b) convective-line regions. Regions of downward motion are shaded. Contours shown are -2 (dashed), 0 and 2 m s^{-1}.

noted to be at 45° angles with respect to the upwind direction. Within this squall line there are many elevated heat sources (i.e. convective cells), and it is noted that these convective cells are not linearly arranged along the leading line (Fig. 4.14a). Each individual cell generates wave-fronts that move in various directions, and as these wave-fronts propagate away, they fall prey to various constructive and destructive interference processes. It is possible that the complicated shear profile within this squall line could have led to an organization of the vertical motion field into the wave-front patterns (noted to be at ~45° angles with respect to the squall line's orientation) observed.

4.5.3 Secondary band line-parallel cross sections

Figure 4.20 shows the reflectivity field through the heart of the secondary band region. Weak bright band signatures are present along this cross section centered at $Z = 2.5$ km (e.g., near $Y = 36$ km). Rearward, Fig. 4.20a shows a much weaker region of enhanced precipitation.

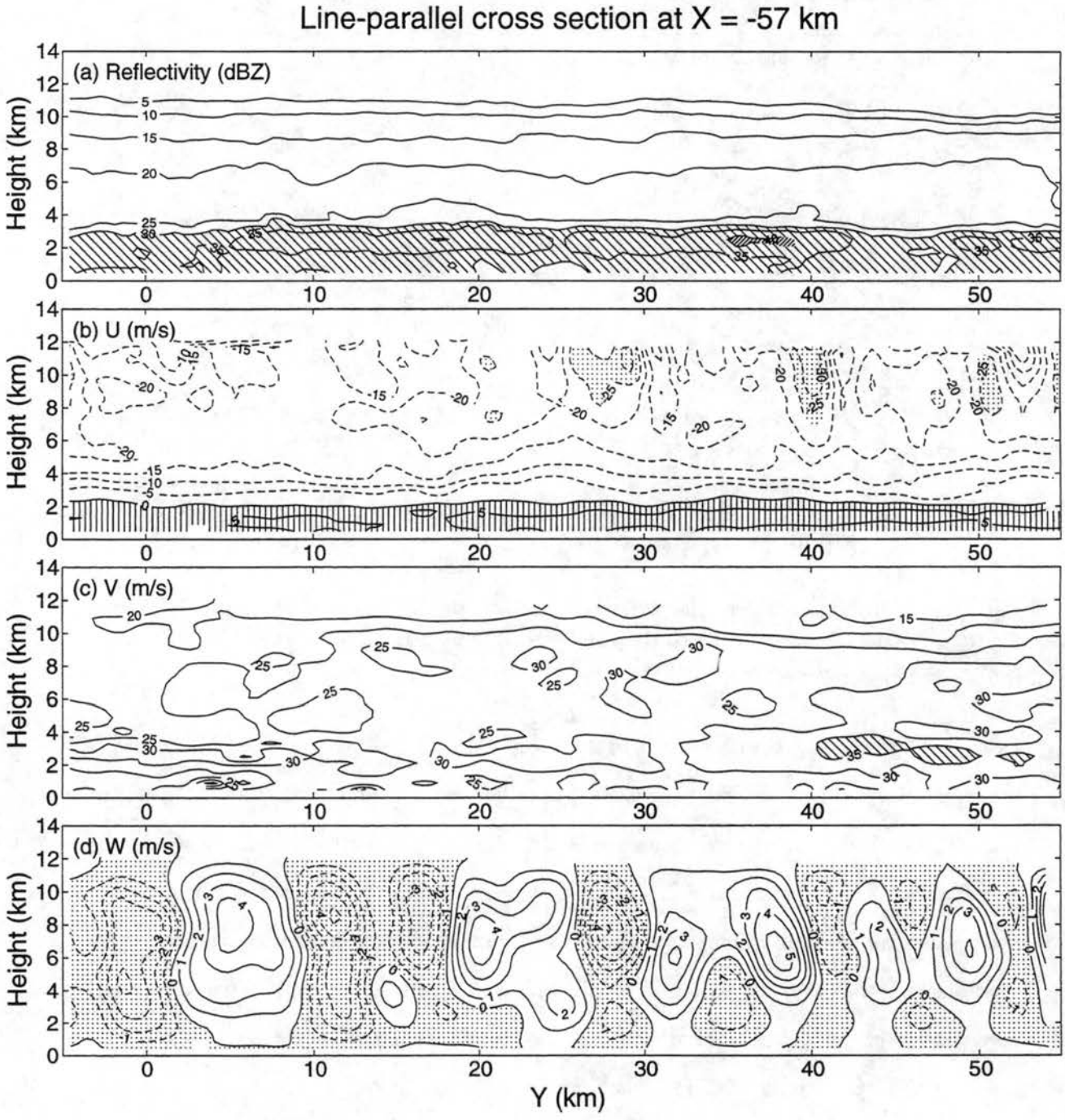

Figure 4.20: Line-parallel cross section along $X = -57$ km showing (a) reflectivity (dBZ) contoured every 5 dBZ, (b) U contoured every 5 m s^{-1}, (c) V contoured every 5 m s^{-1}, and (d) vertical velocity contoured every 1 m s^{-1}. In (a), light hatching indicate reflectivities >30 dBZ and dark hatching indicate reflectivities >40 dBZ. In (b), negative contours are dashed, vertical hatching indicates positive (RTF) flow and angled hatching indicates negative (FTR) flow <-30 m s^{-1}. In (c), negative contours are dashed and hatching indicates flow >30 m s^{-1}. In (d), negative contours are dashed and downdrafts are shaded.

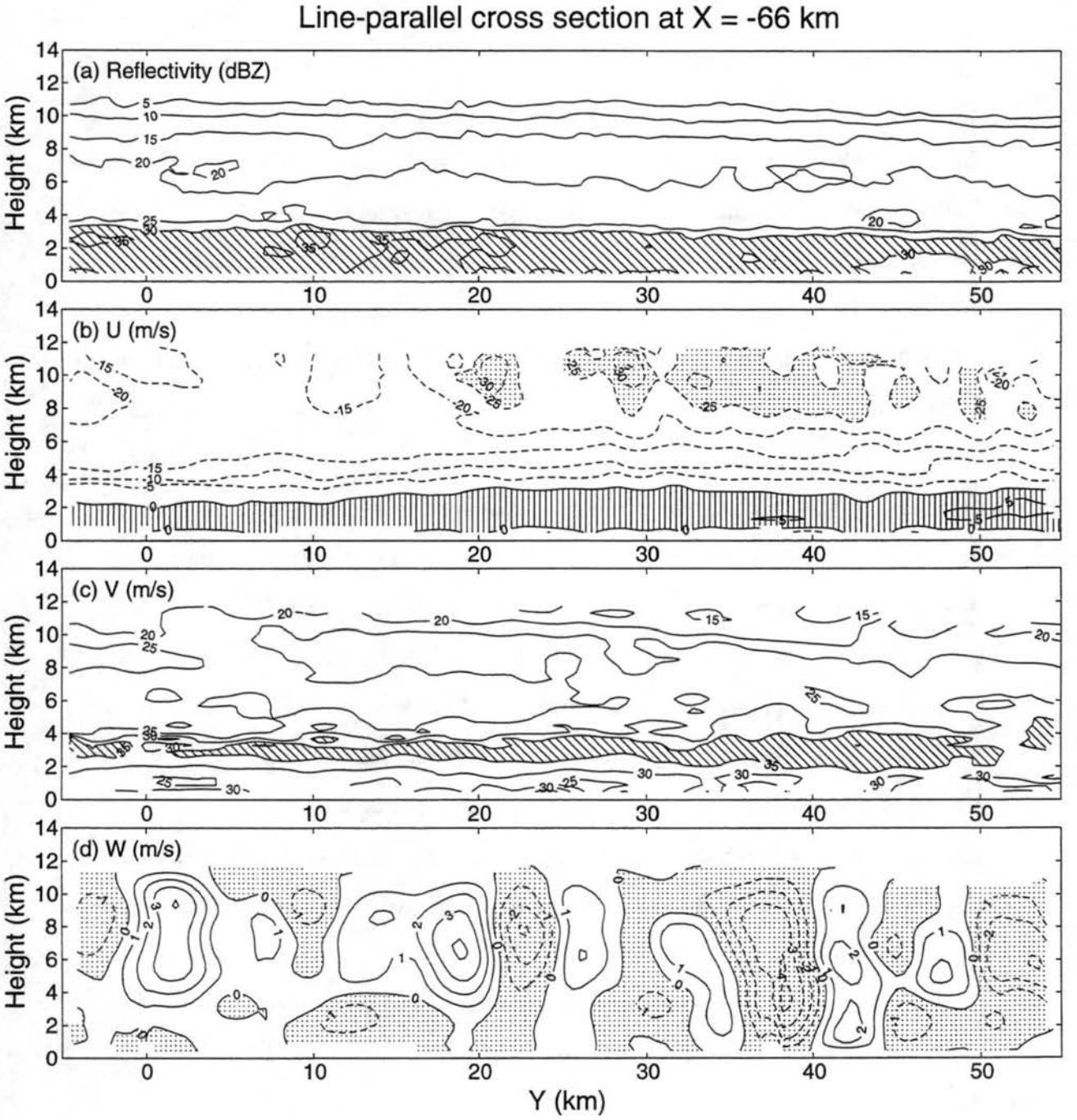

Figure 4.21: As in Fig. 4.20 except along $X = -66$ km.

The U field at $X = -57$ (Fig. 4.20b) emphasizes the RTF flow present below $Z = 2$ km. Along $X = -66$ km (Fig. 4.21b), the RTF flow is generally less than 5 m s^{-1}, while a region of weak outflow (FTR flow) can be observed below $Z = 1$ km. Significant variability in the upper-level FTR flow is observed in both of these cross sections. This variability is in part due to the gravity wave-induced circulations present above the secondary band.

The V field along $X = -57$ km (Fig. 4.20c) depicts areas of slight enhancement in the along-line flow near $Z = 3$ km. Aloft, the magnitude of V decreases to less than 20 m s^{-1}. At $X = -66$ km (Fig. 4.21c), the extent of the along-line jet is denoted by the shaded region (V >35 m s^{-1}). This region of enhanced V corresponds well with the melting layer (located below $Z = 3$ km), further suggesting that enhancement of the flow by a melting-induced stable layer is occurring.

Updrafts and downdrafts are interspersed throughout the secondary band region. Along $X = -57$ km (Fig. 4.20d) both updrafts and downdrafts of magnitude >5 m s^{-1} are present. Rearward, the $X = -66$ km cross section (Fig. 4.21d) shows similar variability to the vertical motion field. Though somewhat weaker in magnitude, the pattern of updraft/downdraft couplets is similar to that noted along the $X = -57$ km cross section. There is support for some of these vertical motions in the reflectivity field. Near $Y = 38$ km in Fig. 4.20d there is an updraft co-located above a region of enhanced precipitation, while at $Y = 15$ km in Fig. 4.21d, a downdraft is located near a fallstreak of precipitation.

These updraft/downdraft couplets observed in these two along-line cross sections are further evidence of the three-dimensional nature of the gravity wave oscillations observed within the squall line.

Because there is no time evolution of this secondary band documented, one can only speculate as to what impacts these vertical motions may be having on this region of the squall line.

Microphysically, these observed vertical motions could have an impact on the nucleation of cloud droplets, and could possibly lead to enhanced depositional growth of ice particles being advected through this region by the FTR flow. Furthermore, these vertical motions could possibly play a role in the electrification process within the secondary band (e.g.,

Rutledge and Petersen 1994). Obviously, knowledge of particle dwell time within these updrafts and downdrafts would be needed to interpret any possible microphysical and cloud-charging processes these vertical motions may induce.

4.6 Summary of the fine-scale observations of the 7-8 May squall line

The results of the fine-scale analysis show significant perturbations to the mid and upper-level horizontal flow, possibly due to Bernoulli-type accelerations near deep convection. Also, accelerations in the low- to midtroposphere line-perpendicular flow appeared to be related to the LeMone (1983) low to the rear of the convective line. Within the secondary band, enhancement (possibly due to a melting-induced stable layer) of an along-line jet were noted.

The observed convective-line tilted-updraft structure and secondary band mesoscale updraft/downdraft couplet were both shown to be results of compositing the complicated small-scale updraft and downdraft structure observed within this squall line.

Upon closer inspection, the vertical motion field was shown to contain high-frequency gravity wave oscillations within the secondary band. Evidence for these waves came by way of an observed quadrature phase relationship the vertical motion field had with perturbations in the line-perpendicular flow. Wave-fronts in the vertical motion field (oriented perpendicular to the mid-level system-relative flow) were noted to be possible three-dimensional manifestations of these observed gravity wave features.

Chapter 5

VOLUME STATISTICS FOR THE CONVECTIVE-LINE AND SECONDARY BAND REGIONS

5.1 Volume-averaged statistics

The previous Chapter dealt with the 7–8 May squall line from both a two and three-dimensional perspective. In this Chapter, volume-averaged mean profiles and Contoured Frequency by Altitude Diagrams (CFADs) of the dual-Doppler data are employed to provide further insight into the precipitation and kinematic structures associated with the convective-line (CL) and secondary band (SB) volumes of this squall line. In addition, vertical mass transport within these two volumes will be explored in an attempt to further understand the precipitation processes inherent to both the CL and SB regions of the squall line.

The horizontal outlines for the two volumes that are examined in this Chapter are shown in Fig. 4.1 (dashed rectangles). Both of these volumes encompass 1900 km^2 of their respective regions of this squall line.

5.1.1 Volume-averaged vertical profiles

The vertical profiles of reflectivity for these two volumes (Fig. 5.1a) are similar to those reported for other midlatitude squall lines (e.g., Srivastava et al. 1986; Smull and Houze 1987a; Rutledge et al. 1988). The CL profile has a peak of ~33 dBZ near 1.5 km due to intense low-level precipitation from mature and decaying convection. In contrast, the reflectivity profile within the SB volume has a distinct maximum near 2.5 km (i.e. the bright band; Battan 1973) due to melting of ice through this layer. Above 4 km, both the CL and SB reflectivity profiles are similar differing only by a constant (~8 dBZ). This difference is explained by the rapid fallout of large precipitation-sized particles transported aloft within the CL region (e.g., Rutledge and Houze 1987; Smull and Houze 1987a).

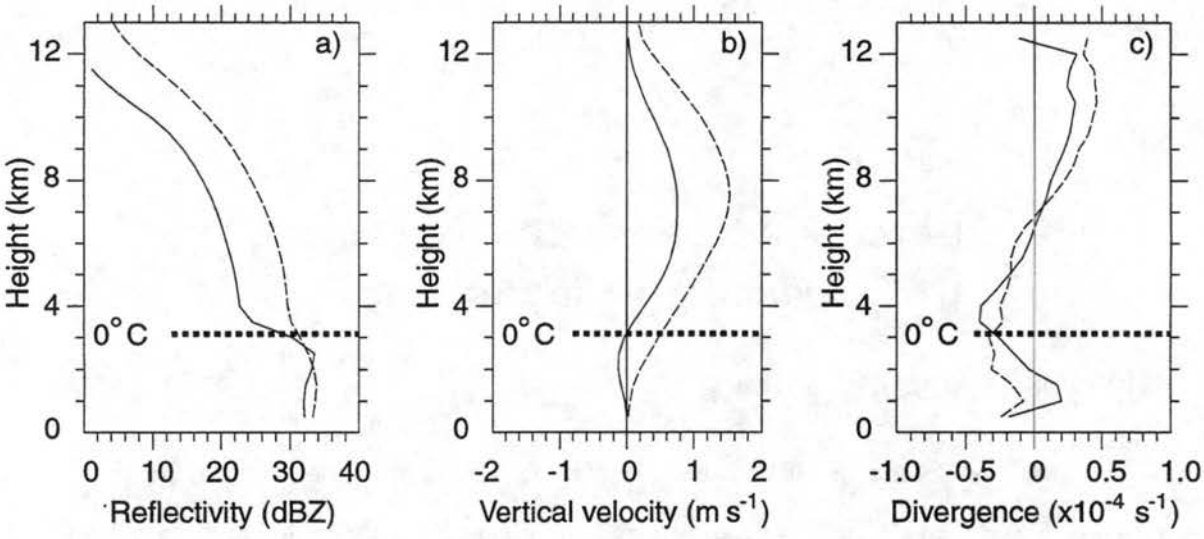

Figure 5.1: Volume-averaged profiles of (a) reflectivity, (b) vertical velocity, and (c) divergence within the secondary band (solid lines) and the convective-line (dashed lines) regions of the 7–8 May squall line. The horizontal dashed line indicates the approximate location of the 0°C level.

As observed in the NEXRAD overview of this squall line (Section 3.3), this secondary band region is in the pre-mature phase of its life-cycle. To further illustrate this point, a comparison of the 7–8 May squall line's SB reflectivity profile is made with those from three other squall lines' mature SBs (22 May 1976; 10–11 June 1985; and 24 May 1991) in Fig. 5.2. Compared to that of the 7–8 May SB region (solid line), the other squall lines, which are in their mature stages, show much sharper and more intense maxima in reflectivity associated with melting.

The mean profiles of vertical motion (Fig. 5.1b) further illustrate distinctions between the CL and SB. The CL profile is entirely positive (due to the deep convection that dominates this region), while the SB profile of vertical motion shows that a mesoscale updraft/downdraft couplet has formed by this time. The peaks in the upward motion are 1.75 m s^{-1} and 1 m s^{-1} for the CL and SB, respectively. The downdraft located below the reflectivity bright band has a maximum magnitude of 0.25 m s^{-1} for the SB volume.

These profiles of vertical motion are similar to those observed in previous squall line studies (e.g., Heymsfield and Schotz 1985; Srivastava et al. 1986; Smull and Houze 1987a;

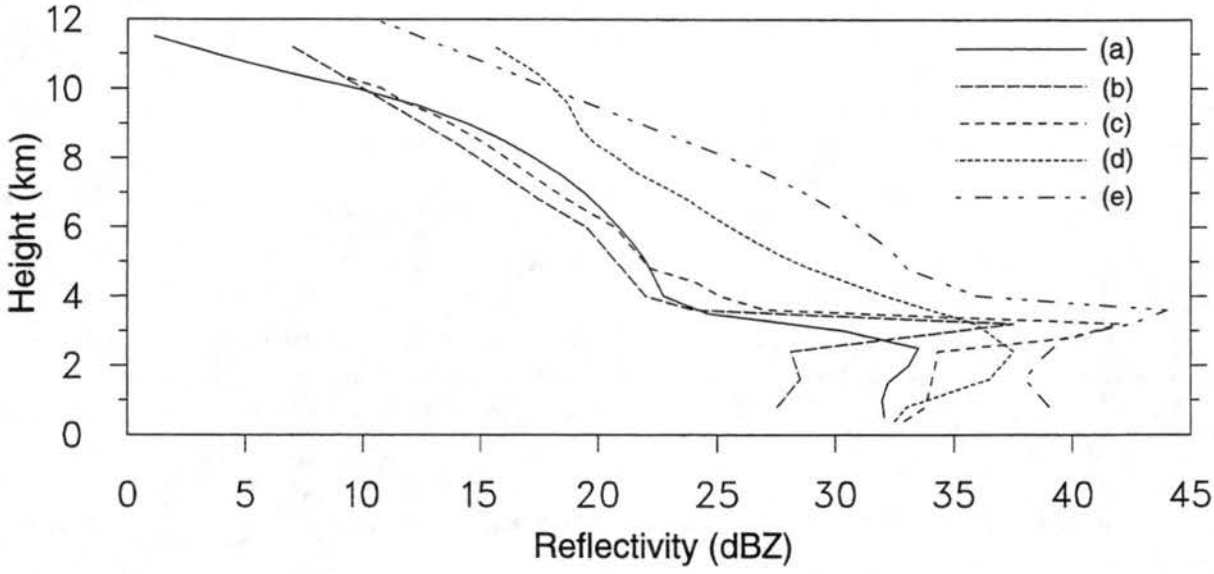

Figure 5.2: Comparison of mean profiles of SB reflectivity from (a) this line, (b) 10–11 June 1985 squall line CP-3 EVAD profile, (c) 10–11 June 1985 squall line CP-4 EVAD profile, (d) 22 May 1976 squall line, (e) 24 May 1991 squall line. The data for profiles (b) and (c) were adapted from Rutledge et al. 1988, while data for profile (d) was adapted from Smull and Houze 1987a. The data for profile (e) was provided by Dr. Terry Schuur.

Rutledge et al. 1988; Biggerstaff and Houze 1991a), except that the SB downdraft is not well developed at this early stage. Figure 5.3 documents the vertical velocity profile for a CL volume (solid line) and a mature SB volume (dashed line) associated with the 10–11 June 1985 squall line. The CL profile is almost identical to that observed within the 7–8 May CL volume (Fig. 5.1b). The SB profile of the 10–11 June squall line matches up well through mid and upper levels. However, at lower levels, the strength of the mesoscale downdraft of the 10–11 June SB is twice that observed within the 7–8 May SB volume.

The divergence profiles (Fig. 5.1c) show strong mid-level convergence in the SB, consistent with other studies documenting the melting-layer convergence within stratiform-type precipitation (Mapes and Houze 1995). This mid-level convergence would seem to be supporting the mesoscale updraft present (due to the weak mesoscale downdraft present at this time). In the CL profile there exists a much deeper layer of convergence than in the SB profile. Convergence through the bottom half of the profile, with divergence above, corresponds well with the updraft-dominated vertical velocity profile for the CL (Fig. 5.1b), and

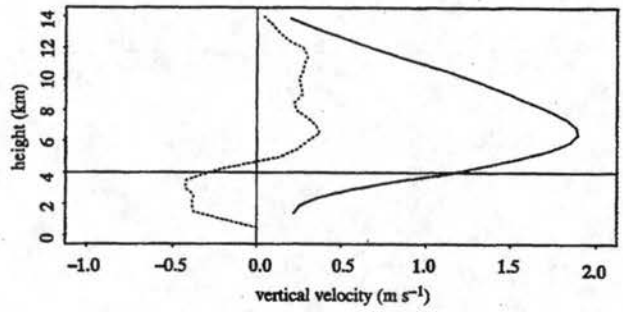

Figure 5.3: Characteristic mean profiles of vertical velocity in convective (solid lines) and secondary band regions of the 10–11 June 1985 mesoscale convective system. The horizontal line at 4 km indicates the 0°C level (from Yuter and Houze 1995b).

is consistent with previous studies of convective region divergence profiles (e.g., Ogura and Liou 1980). There is a curious increase in the convergence in the convective profile at lower levels (below $Z = 1$ km) that could be due to converging outflows from downdrafts produced by decaying convective cells. Both the CL and SB regions exhibit divergent outflow aloft.

5.1.2 Horizontal winds

The mean profile of U (line-perpendicular flow) (Fig. 5.4a) shows the RTF flow weakening as it transitions from the CL to the SB regions, similar to that reported for a developing squall line observed by Klimowski (1994). The rearward acceleration of U observed here at mid-levels has been documented in tropical squall lines (LeMone 1983) and also in mid-latitude squall lines (Smull and Houze 1987a; Kessinger et al. 1987; Rutledge et al. 1988). Comparison with the pre-squall sounding at Purcell, OK (PUR) shows a strong increase in the line-perpendicular shear associated with an up-gradient transport of line-perpendicular momentum (e.g., LeMone 1983; LeMone and Moncrieff 1993). This effect is maximized in the convective line creating the greatest vertical shear there. In the convective line the strongest FTR flow is located near 5 km. In the SB this peak in FTR flow shifts upward to near 8 km. Ascending FTR flow has been documented in previous squall line studies (e.g., Smull and Houze 1987a; Rutledge et al. 1988). Comparison of the CL and SB U profiles reveals divergence of the low-level RTF flow, convergence of mid-level FTR flow, and divergence of FTR flow aloft, consistent with the SB divergence field shown in Fig.

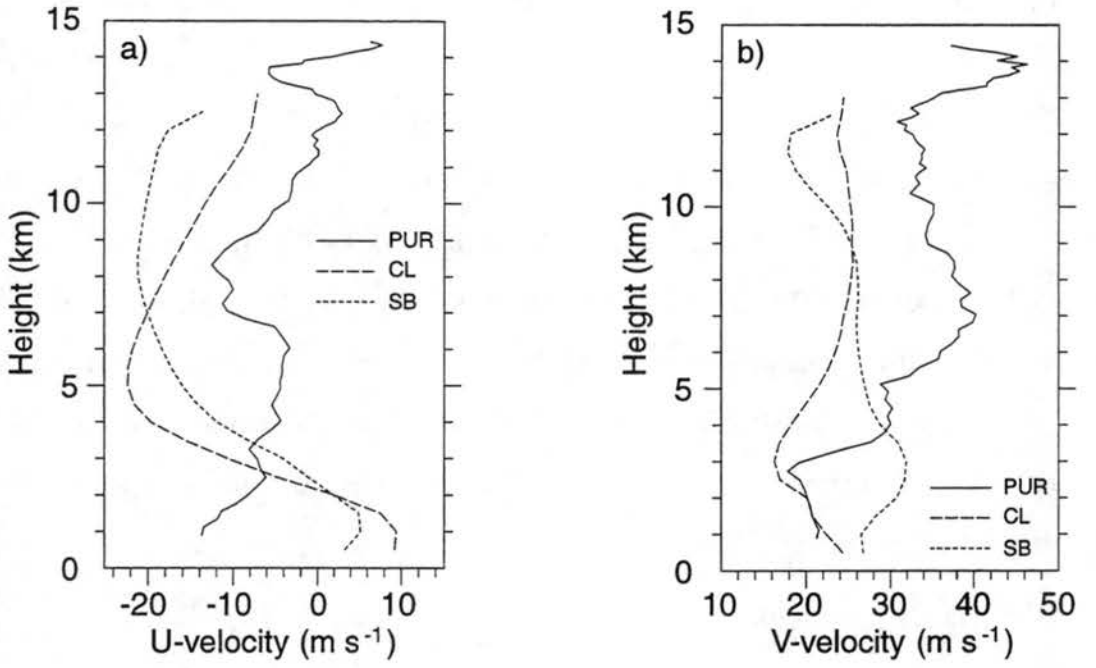

Figure 5.4: Comparisons of the 0000 UTC Purcell, OK sounding derived winds (PUR) and (a) (U) components of the CL, SB and (b) V components from the CL, SB. These sounding-derived winds have been translated to the squall line's reference frame (see Section 2.2.1).

5.1c. This similarity suggests that the primary contribution to the horizontal divergence lies in the line-perpendicular component of the flow.

Generally, the CL V profile (Fig. 5.4b) shows a reduction in the line-parallel component of the flow aloft, consistent with a down-gradient transport that is expected for V (LeMone and Moncrieff 1993). That is, the mid- and upper-tropospheric decrease in V is likely due to the vertical transport of weaker momentum air within the convective region. An exception occurs at low levels in the SB, where a low-level jet up to $\sim$32 m s^{-1} near 3 km appears, nearly double the value of V associated with the convective line. An explanation for this jet-like feature is not immediately obvious, but as mentioned Chapter 4, it may have developed within the stable layer produced by melting in the SB region (Harrold and Browning 1967; Atlas et al. 1969; Szeto et al. 1988a,b; Marwitz and Toth 1993).

5.2 Volume statistics via CFADs

To emphasize the fine-scale variability that ELDORA has sampled during this pass along the 7–8 May squall line, Contoured Frequency by Altitude Diagrams (CFADs) are employed. Yuter and Houze (1995b,c) (hereafter referred to as YH) used CFADs to look at the high-resolution characteristics of a line of cumulonimbi that formed in Florida during the Convective and Precipitation/Electrification Experiment (CaPE) on 15 August 1991. The use of CFADs allowed YH to document and interpret many of the fine-scale variations that occurred while of this complex of cumulonimbi evolved from a cluster of convective cells to a cluster dominated by stratiform-like precipitation. While the convection documented by YH occurred in a tropical-like environment, there are some gross similarities to the two volumes that are analyzed here.

5.2.1 CFAD methodology

The CFADs used in the analysis of this squall line are slightly different from those used by YH. The methodology for the CFADs in this study is identical to that used by Schubert et al. (1995) in their analysis of the tropical inversion layer. At a particular level in the volume, data (say reflectivity) are placed into a series of consecutive bins. The number of grids points that fall into a particular bin are then converted to a percentage of the total number of grid points at that level. This percentage is then contoured as a frequency distribution for each level in the vertical spanning the particular field along the horizontal axis. The advantage of producing the CFADs by this method is that at any given level, the summation of the frequencies associated with all the bins will give 100%. The CFAD frequency contours used here differ from those used by YH only by a constant. So a general comparison between the structure of the CFADs produced here and ones that YH constructed will be possible.

5.2.2 Reflectivity and vertical velocity CFADs

One observes a wide distribution of reflectivity in the CL CFAD (Fig. 5.5a) associated with the deep convection present. The SB reflectivity CFAD (Fig. 5.5b) exhibits a much narrower distribution of reflectivity (through mid and upper levels) due to more stratiform-like precipitation present. Through the lower levels, the SB reflectivity CFAD depicts

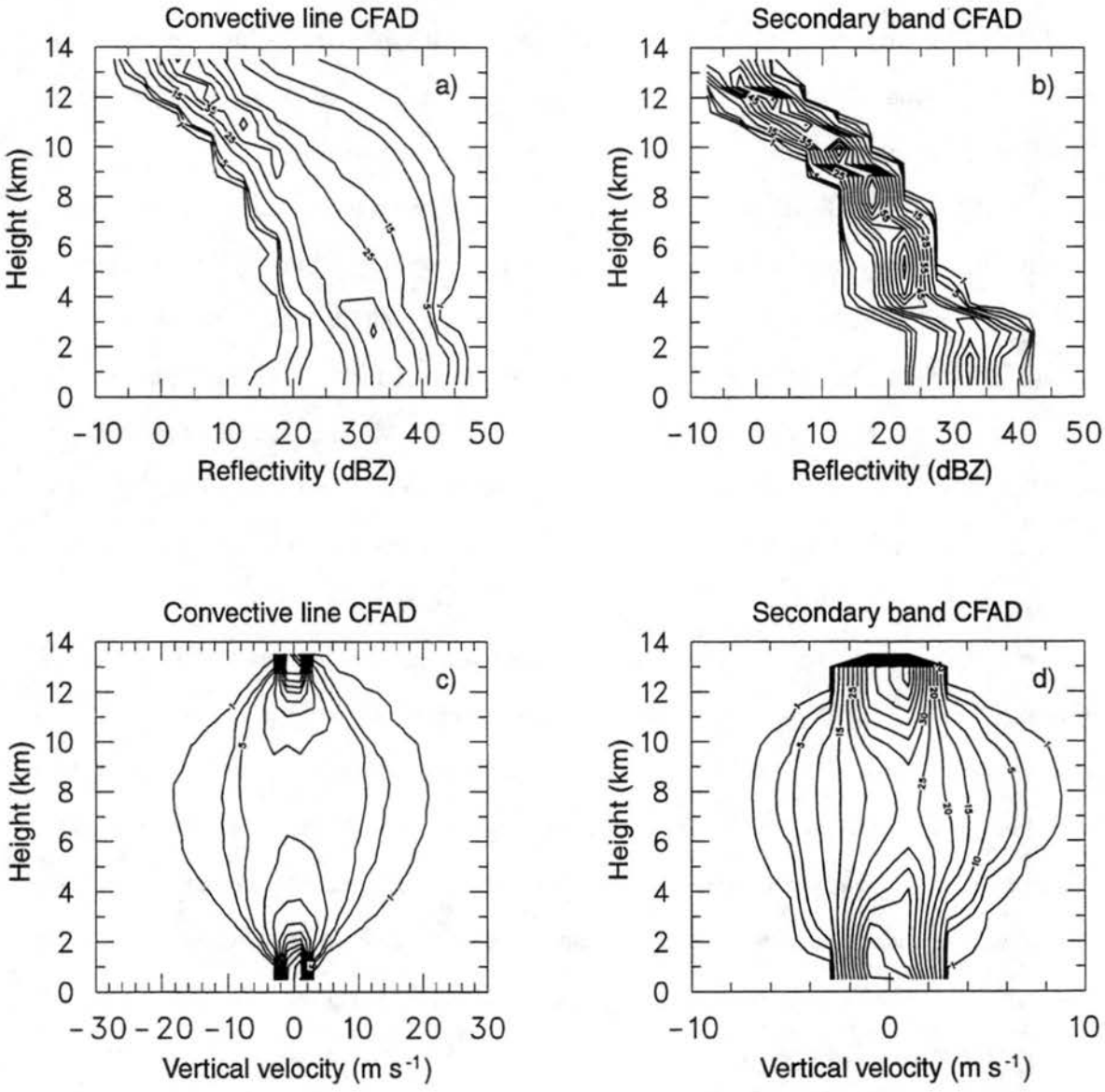

Figure 5.5: Contoured Frequency by Altitude Diagrams (CFADs) depicting: (a) convective reflectivity, (b) SB reflectivity, (c) convective vertical velocity and (d) SB vertical velocity. For the reflectivity CFADS the bin size is 5 dBZ and the vertical velocity CFADs have a corresponding bin size of 2 m s^{-1}. The CFADs are all contoured at 1%, 3%, 5% and every 10% interval after the 5% frequency contour. Note that the abscissa scale is different for (d).

a widening of the frequency distribution through and below the bright band level. The structure of the reflectivity CFADs is very similar to the mean vertical profiles of reflectivity shown in Fig. 5.1a.

When compared to results derived from other squall lines, the issue of maturity of the 7–8 May squall line's SB region again comes to the forefront. Figure 5.6 shows a set of CFADs computed from a mature stratiform volume connected with the 10–11 June 1985 squall line. The CFAD of reflectivity (Fig. 5.6a) shows a narrowing of the frequency distribution above the bright band level similar to that observed in the 7–8 May SB region. Also observed is a widening of the distribution below the melting level. The distribution through the bright band level of the mature SB structure of the 10–11 June squall line is skewed to a higher range of reflectivity than that of the 7–8 May squall line's SB. It is the skewing of the distribution (through the melting level) to a higher range of reflectivity that signifies the strength of the bright band (and therefore the level of SB maturity).

The wide distribution of vertical velocities observed in the CL CFAD (Fig. 5.5c) is a reflection of the convective-scale vertical motions present. The overall distribution of vertical velocity is slightly skewed to that of positive vertical velocity (which is consistent with the mean profile shown in Fig. 5.1b). The distribution of vertical velocity through the SB volume (Fig. 5.5d) is much narrower (note change in abscissa scale) due to the weaker range of vertical velocities present. Above 3 km the distribution is skewed to positive vertical velocity, while at lower levels the majority of vertical velocities are negative, as the mean vertical profile (Fig. 5.1b) suggests. It turns out that the mesoscale updraft/downdraft couplet, observed to be present in the secondary band volume (Fig. 5.2b), is only present in a volume-averaged sense. There are both updrafts and downdrafts present at all levels within the SB volume. A similar conclusion was noted by YH in their work.

Within both the CL and SB volumes a wide range of vertical velocities are observed. Rather than being a region of weak ascent and decent, the vertical velocity CFAD shows that half of the mid-level updrafts and downdrafts occurring in the secondary band are of magnitude $\geq$2 m s^{-1}. Within the CL volume 50% of the mid-level updrafts are $\geq$6 m s^{-1}, while 42% of the mid-level downdrafts are ≤ -6 m s^{-1}. The implications of this wide range

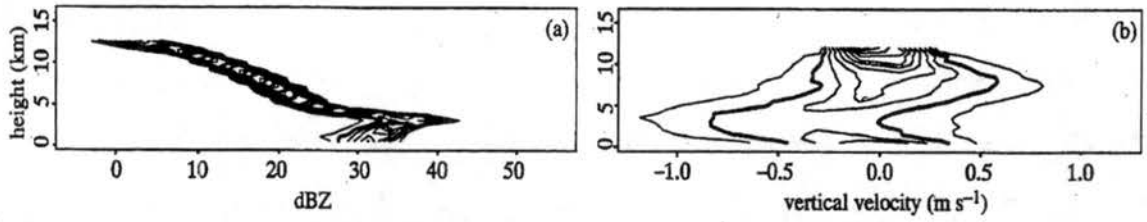

Figure 5.6: CFADs of radar reflectivity (left) and vertical velocity frequency (right) from a stratiform volume behind a Kansas squall line at 0345 UTC 11 June 1985 during PRE-STORM. (a) Radar reflectivity CFAD bin size is 2.5 dBZ, contoured at 5% dBZ^{-1} km^{-1} intervals, (b) vertical velocity CFAD bin size is 0.2 m s^{-1}, with 50% ms^{-1} km^{-1} contour intervals and the 100% ms^{-1} km^{-1} contour highlighted (from Yuter and Houze 1995b).

of vertical velocities in both the CL and SB regions will be addressed in the upcoming vertical mass transport section of this Chapter.

The 10–11 June CFAD of vertical velocity (Fig. 5.6b) shows the frequency distribution associated with a mature stratiform region. At upper levels the distribution is skewed towards the updraft side; while at lower levels the distribution is skewed to the downdraft side of the spectrum. Again one observes both updrafts and downdrafts at all levels within the SB volume; however, the strengths of the drafts are much weaker than those observed within the 7–8 May SB. A possible explanation for the observed difference in vertical motion magnitudes could be the sampling of a more mature SB (i.e. less volatile) within the 10–11 June squall line. Another explanation could be the difference in data resolution used to observe the 10–11 June and 7–8 May squall lines. The higher-resolution data used here is resolving kilometer-scale drafts that were not resolvable within the lower-resolution 10–11 June data set.

5.2.3 Comparisons with the Yuter and Houze CFADs.

A set of CFADs for reflectivity and vertical velocity that YH calculated for five dual-Doppler volume scans are shown in Fig. 5.7. These CFADs document the evolution of a line of cumulonimbi over South Florida as it transitioned from a convective stage to a stratiform stage. Motivation for comparing the YH series of CFADs to those of the CL and SB volumes of the 7–8 May squall line is to compare similar high-resolution dual-Doppler data sets from

subtropical and midlatitude squall lines. The YH data volumes that are most similar to those volumes within the 7–8 May squall line are the 2155 UTC (Figs. 5.7g and 5.7h) for the CL volume observed here and 2237 UTC (Figs. 5.7i and 5.7j) for the SB volume.

The CL reflectivity CFAD (Fig. 5.5a) has a similar profile to the 2155 UTC YH reflectivity CFAD (Fig. 5.7g). Other than being shifted to a lower range of reflectivity, the only other difference seems to be the large area of high reflectivity frequencies that are occurring at mid and upper levels of the 7–8 May CL CFAD. This difference can be traced to the few intense updraft cores that are being sampled while in this volume (Fig. 5.5a). Elevated reflectivity maxima were observed during earlier YH reflectivity CFADs (e.g., 5.7c) when more vigorous convection dominated the volumes.

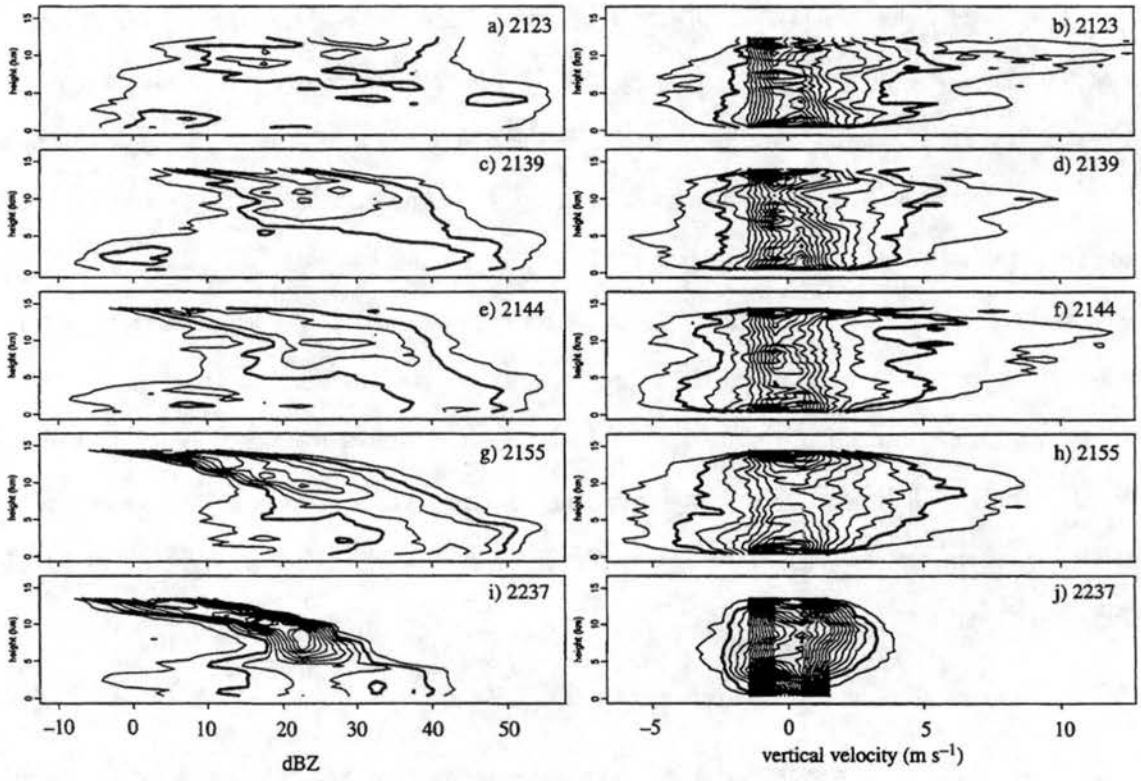

Figure 5.7: Time series of CFADs of radar reflectivity (left column) and vertical velocity frequency (right column) corresponding to five different dual-Doppler volume scans taken from Yuter and Houze (1995b). Radar reflectivity CFAD bin sizes are 2.5 dBZ, contoured every 2.5% dBZ^{-1} km^{-1} interval with the 5% dBZ^{-1} km^{-1} contour highlighted. The vertical velocity CFAD bin sizes are 1.0 m s^{-1}, with 5% ms^{-1} km^{-1} contour intervals and the 10% dBZ^{-1} km^{-1} contour highlighted.

The 7–8 May SB reflectivity CFAD (Fig. 5.5b) compares well with the YH stratiform-like CFAD (Fig. 5.7i) through the upper-levels. At lower levels one observes a much wider distribution of reflectivity in the YH reflectivity CFAD. This wider distribution is likely due to the volume that YH used which encompassed areas of weaker reflectivity not associated with enhanced stratiform precipitation.

The major difference between the 7–8 May squall line and the line of cumulonimbi observed by YH pertains to the vertical velocity CFADs within regions of convection. One observes a much higher range in the magnitude of updrafts within the CL of the 7–8 May squall line to that observed within any of the YH vertical velocity CFADs. This difference is due to the different environments that these two cases occurred in. The Convective Available Potential Energy (CAPE) over Oklahoma was approximately three times higher than that of South Florida, which explains the more energetic updrafts present within the CL region of the 7–8 May squall line. The mid- and upper-tropospheric downdrafts within the CL volume are much more numerous and energetic than in any of the YH volume series of vertical velocity CFADs. The vigorous updrafts within the 7–8 May squall line are likely forcing intense upper and mid-level downdrafts observed within the CL (examples of which were noted in Chapter 4) (Heymsfield and Schotz 1995; Smull and Houze 1987a).

The vertical velocity distribution within the YH observed stratiform region (Fig. 5.7j) is very similar to that of the 7–8 May squall line's SB volume (Fig. 5.5d). Because YH used comparable high-resolution data to analyze their stratiform region, the similarities in the two vertical velocity CFAD structures would seem to support the idea that higher-resolution data sampling (which resolves kilometer-scale drafts) is the reason for the wider range of vertical motions observed.

5.3 The reflectivity structure of the transition zone.

Though volumes have been chosen representing the CL and SB regions of this squall line, there obviously exists a transition zone (TZ) of weaker reflectivity between these two regions. A TZ associated with the 10–11 June 1985 PRE-STORM squall line was documented by Biggerstaff and Houze (1993) and shown to be region of the squall line

that was dominated by descending motion. Because of limitations of the dual-Doppler analysis, it is not possible to retrieve the kinematic fields through most of this region, although reflectivity fields can be determined. The region analyzed here is between the two rectangles shown on Fig. 4.1 and spans the Y direction from Y = 20 to 85 km and covers 1600 km^2 of the TZ.

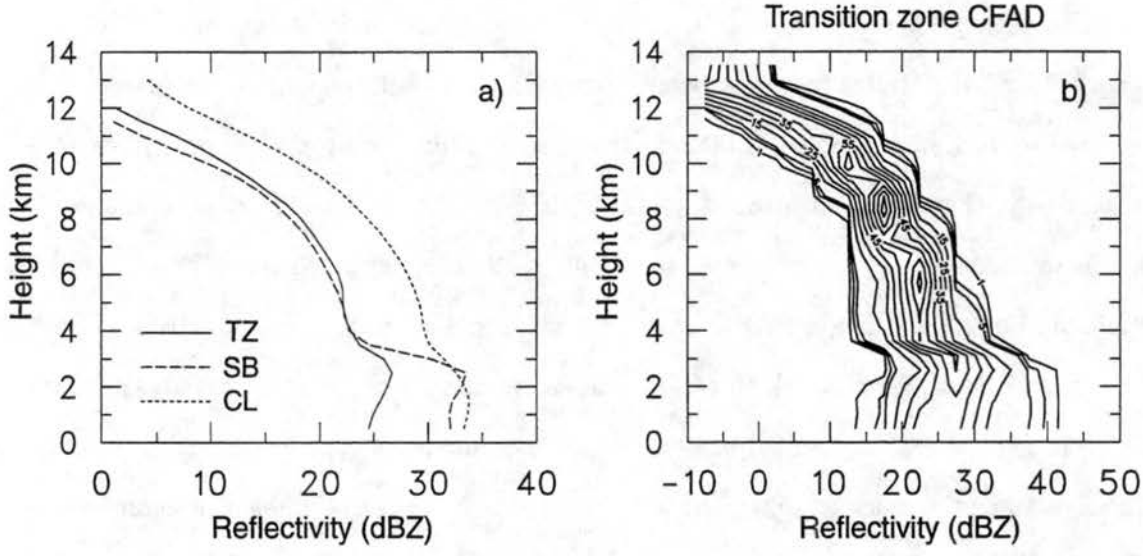

Figure 5.8: (a) A comparison of the vertical profiles of reflectivity for the three regions of this squall line and (b) CFAD of the transition zone reflectivity. (TZ) the transition zone, (SB) the secondary band, and (CL) the convective line. The reflectivity CFAD used here is constructed identically to those in Fig. 5.5.

Mean vertical profiles for the TZ, SB and CL are shown in Fig. 5.8a and a reflectivity CFAD for the TZ is shown in Fig. 5.8b. Figure 5.8a shows that the distribution of reflectivity at upper levels is similar for the TZ and SB except that the TZ has slightly higher values. Higher reflectivities at upper levels in the TZ are expected due to larger ice particles present that have not had a chance to settle out of the trailing anvil region yet. Smull and Houze (1987a) showed a similar decrease between the upper level mean profiles of reflectivity for the TZ and SB regions of the 22 May 1976 squall line.

The peak in the TZ vertical profile of reflectivity near the bright band is much less prominent than in the SB reflectivity profile. This underscores the enhancement of reflectivity due to melting associated with the bright band. Below 2 km the TZ reflectivity profile is ~7 dBZ lower in value than that of the SB volume. The TZ reflectivity CFAD (Fig.

5.8b) confirms that there is a shift in the peak frequencies from the melting level downward when compared to the SB reflectivity CFAD (Fig. 5.5b). Though significant variability exists below the bright band, the overall magnitude has shifted to smaller reflectivity values and encompasses a lower range of reflectivity. This reduction in low-level reflectivity is consistent with previous studies of squall line TZs (Smull and Houze 1987a; Kessinger et al. 1987; Biggerstaff and Houze 1993; Schuur 1997).

5.3.1 Horizontal velocity CFADs

The CL U–component velocity CFAD (Fig. 5.9a) documents a peak in RTF flow of $\sim$10 m s^{-1} with significant variation in U at the lowest levels (likely due to precipitation-induced outflow). There is a general transition from RTF to FTR flow near 2 km with the peak in FTR flow located near 5 km centered on the -20 to -25 m s^{-1} bin. Ninety-five percent of the velocity distribution at 5 km is located between -35 m s^{-1} and -10 m s^{-1}, indicating the large variability associated with FTR flow. Small-scale effects, including vertical momentum transport, gravity wave-induced circulations, and decaying cell-induced circulations are likely broadening the distribution of U near 5 km. Above this peak, the FTR flow gradually decreases in magnitude, although there is still considerable variability due to the divergent outflow associated with deep convective cells.

The SB appears to have a wider distribution of U through the middle of the volume than that of the CL (Fig. 5.5a); however, the two distributions are actually very similar. The greater vertical shear in the CL creates this deception. At upper levels, the FTR flow is not as sharply peaked as that observed in the CL. The shaper peak in the CL is due to areas of RTF flow at upper levels in the CL. The general trend in the SB is a widening of the frequency distributions with the largest peak in FTR flow located near 9 km. Above 9 km there is a noticeable broadening of the distribution of U. The region near 13 km encompassed by the outline of the 5% contour is similar in width to that observed in the CL. Low-level outflow increases the distribution through the lowest levels, while gravity wave-induced perturbations enhance the distributions through the lower and upper levels within the SB (as noted in Chapter 4).

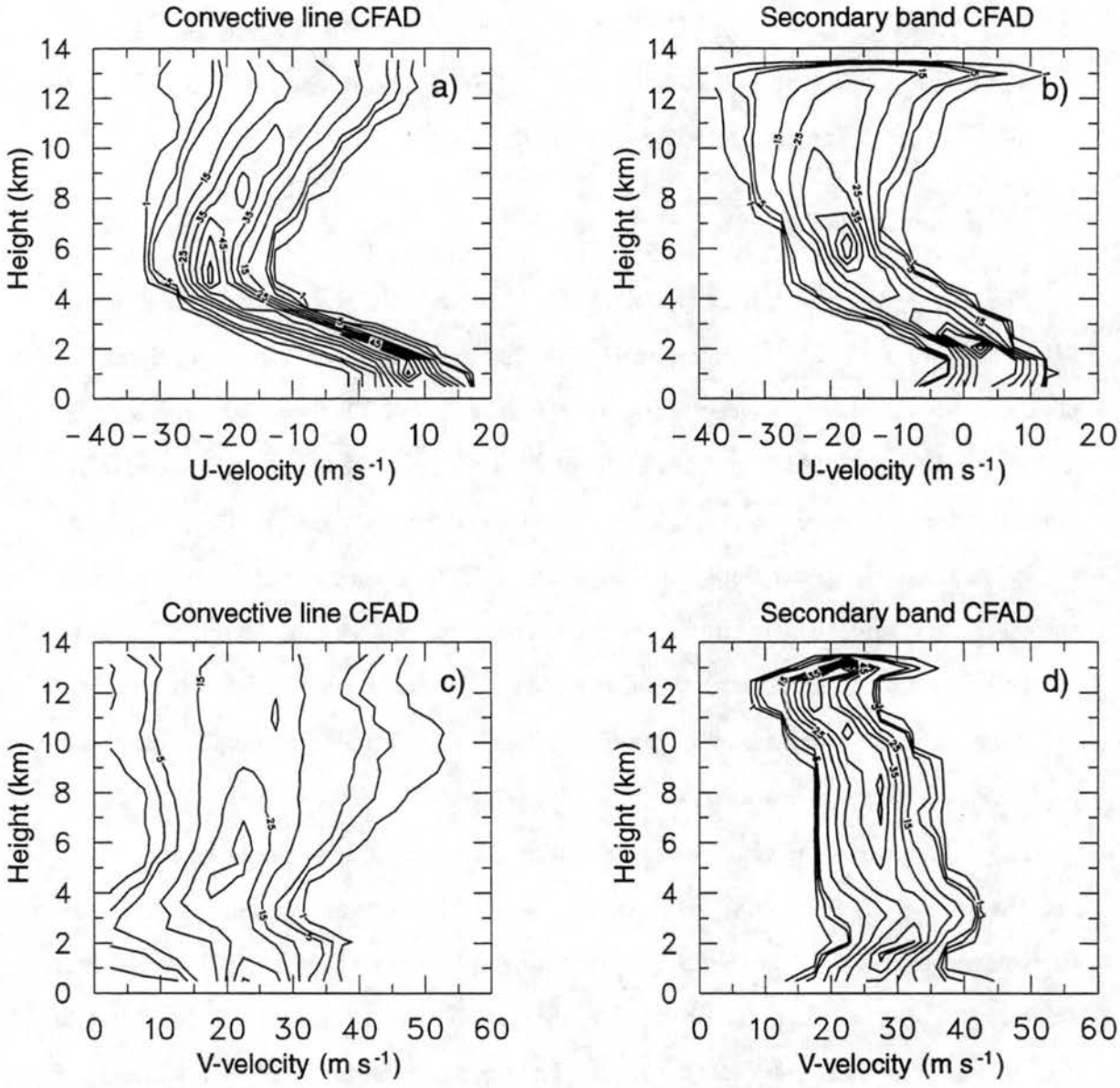

Figure 5.9: Contoured Frequency by Altitude Diagrams (CFADs) depicting system-relative: (a) convective U–component velocity, (b) secondary band V–component velocity, (c) convective U–component velocity and (d) secondary band V–component velocity. A 5 m s^{-1} bin size is used for these CFADs. These CFADs are contoured identically to those in Fig. 5.5.

The CFADs of the V–component velocity for the CL (Fig. 5.9c) and SB (Fig. 5.9d) contrast sharply. The CL V CFAD has a wide distribution at all levels. The narrowest part of the distribution is located near 5 km while the broadest part is located near 10 km. Contributions to the broadening of the distribution through upper-levels include: vertical momentum transport within the CL (which would disrupt the dominant along-line flow present), possible Bernoulli-type accelerations of the line-parallel flow that may exist near strong convective cells (Newton 1969), and divergent outflow from the convective cells. These contributions to the upper-level frequency broadening of V may also play a role in the broadening observed in U (Fig. 5.9a) at upper levels.

The SB V CFAD (Fig. 5.9d) has a much narrower distribution throughout the volume. This CFAD illustrates well the peak in V near 3 km (the approximate height of the 0°C isotherm), which supports the notion that an acceleration of the V is occurring near the melting level as hypothesized in Section 4.3.

5.4 Vertical mass transport

A number of previous studies have examined the distribution of the mass flux within squall lines (e.g., Houze 1977, Gamache and Houze 1982; Heymsfield and Schotz 1985). As pointed out by YH, it is the amount of air moved, which is related to the amount of water condensed, that is a fundamental part of interpreting the precipitation that is present.

5.4.1 Mass transport methodology

The CFADs of mass-transport-weighted vertical velocity (mass CFADs for short) that are presented here are very similar in construction to those used by YH. The contours are the sum of the mass transport that fall inside the bins of vertical velocity occurring across the horizontal and then plotted at each level in the vertical. Also presented here are vertical profiles of the total upward and downward mass flux (summed at each level in the vertical). Mass CFADs provide further insight into the net mass flux by distinguishing which vertical velocities are responsible for the mass transport at a given level in the vertical. Because both of these quantities are dependent on the volumes being analyzed, a direct comparison

of previously documented mass transports is not possible. But the general profiles observed can be compared to previous studies.

5.4.2 Convective-line and secondary band mass transport

The net upward mass transport within the CL (Fig. 5.10a) has a maxima centered near 7 km and is consistent in shape to that reported in previous studies (Gamache and Houze 1982; Heymsfield and Schotz 1985). The CL mass CFAD (Fig. 5.10b) has a distribution of the upward mass transport centered on small vertical velocities at low levels (near $Z = 2$ km), with a general widening in distribution of the mass transport observed through the mid-levels of the CL volume. The shape of the upward mass flux distribution is explained in terms of a parcel's ascent. Initially, there is little differentiation between parcel updraft velocities as they begin rise in the CL. Hence, the narrow distribution of upward mass transport observed through the lower levels. It is through the mid-levels that the opportunistic nature of each parcel is fulfilled. Different characteristics (i.e. entrainment rates, buoyancy, etc...) are realized by each parcel and lead to the observed broadening of the upward mass transport through the mid-troposphere. At mid-levels the peak in the upward mass transport (roughly outlined by the 400×10^7 kg s^{-1} interval) is centered on the 8-10 m s^{-1} bin. Fifty percent of the upward vertical mass transport is occurring with vertical velocities greater than 12 m s^{-1} which only occupy 25% of the positive vertical velocities within the CL volume. A substantial portion of the vertical mass transport (and therefore condensation) is occurring near, or within, moderate to strong updrafts.

Yuter and Houze (1995c) observed that vertical mass transport within the convective region of a Southern Florida cumulonimbi ensemble was dominated by weak and moderate-strength upward velocities (Fig. 5.11). The results observed here suggest that this is not the case for convection associated with the 7–8 May squall line. The convection documented by YH was not observed to contain many large updrafts ($\geq$10 m s^{-1}) (Fig. 5.7). In contrast, convection observed here has much more vigorous updrafts present that contribute significantly to the vertical mass transport. As observed earlier, the environmental setting

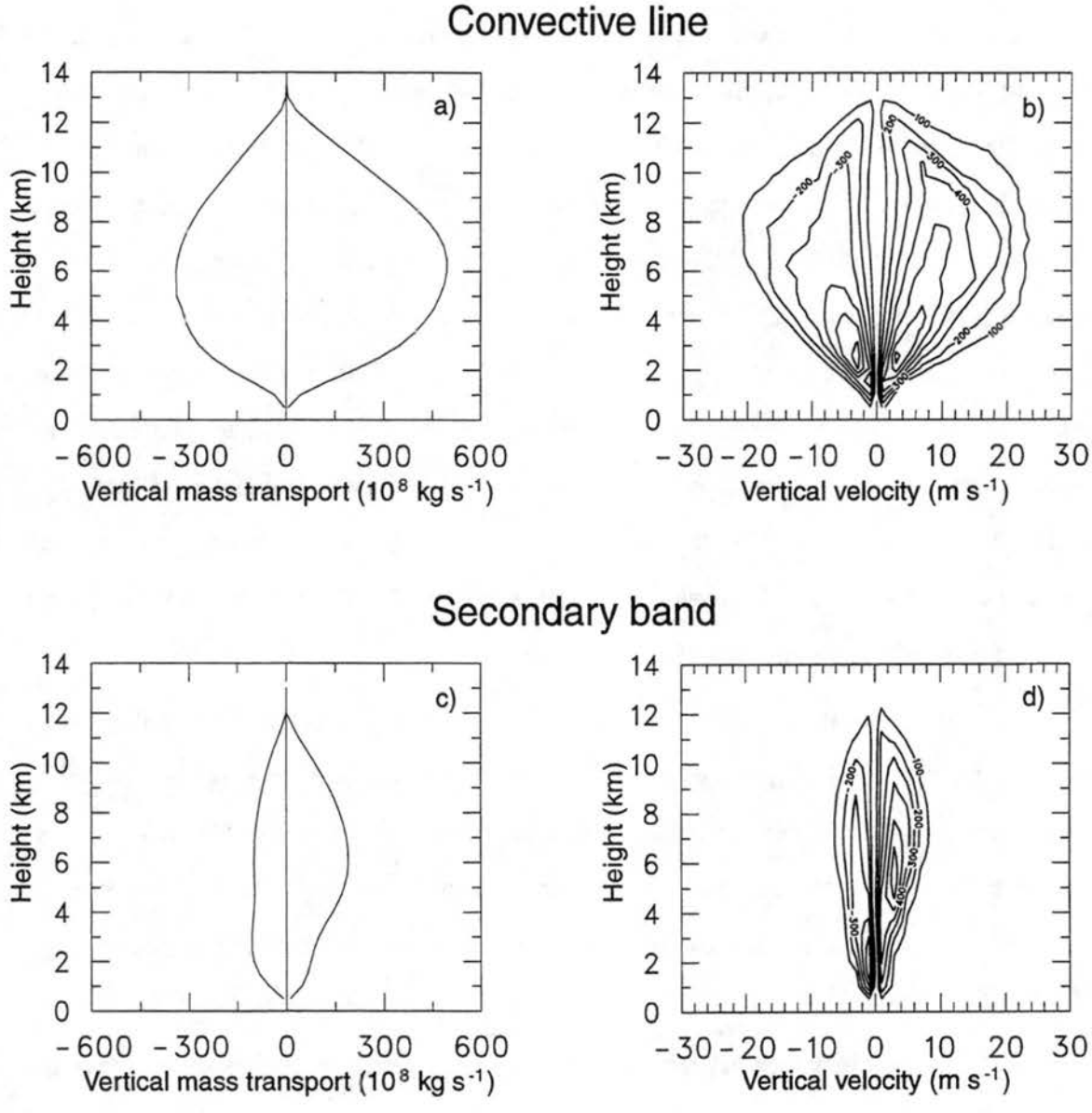

Figure 5.10: Vertical-mass-transport-weighted CFADs of vertical motion (left) and net vertical mass transport upward and downward (right). Vertical mass transport is contoured in the CFADs at 100×10^7 kg s^{-1} intervals. The corresponding bin size for the CFADs is 2 m s^{-1}. Convective-line data are used for (a) and (b), with secondary band data used for (c) and (d).

(i.e. CAPE) most likely plays a role in the greater magnitude of updrafts associated with the 7–8 May convection, which then directly impacts the vertical mass transport.

The downward mass transport (Fig. 5.10a) associated with the CL has a maximum at mid-levels, and is similar in shape to previous observations of convective volume transport by Heymsfield and Schotz (1985). The CL mass CFAD (Fig. 5.10b) shows that at lower-levels the mass transport is centered on weaker velocities, presumably related to precipitation downdrafts present. However, there is still strong downward transport in the mid-troposphere, in part due to frequent upper-level downdrafts present (e.g., Heymsfield and Schotz 1985; Knupp 1987; Smull and Houze 1987a). This mid-level downward mass transport is almost two-thirds that of the upward net mass flux, and is much greater than that shown in studies by Heymsfield and Schotz (1985) and Yuter and Houze (1995c) (Fig. 5.11). Examination of the 7–8 May downward mass transport reveals that 50% of the transport is being done by negative velocities less than -6 m s^{-1} which account for 50% of the total number of mid-level downdrafts within the CL.

For the SB volume one observes a maximum in upward mass flux (Fig. 5.10c) near 6 km. The mass CFAD (Fig. 5.10d) indicates that this maximum in mass flux is centered on the 2-4 m s^{-1} vertical velocity bin indicating that the bulk of the upward mass transport through this layer is being performed by vertical velocities between 2-4 m s^{-1}, which is not surprising considering the distribution of updrafts observed within the SB vertical velocity CFAD (Fig. 5.5d).

It is the apparent lack of transport by downward vertical velocities that stands out in the SB vertical mass flux. The downward mass flux is nearly constant from $Z = 2$ to 8 km, with only a slight increase at low-levels due to the mesoscale downdraft. The downward mass transport differs greatly from that observed within the SB region of the 10–11 June 1985 squall line (Fig. 5.12a) which was documented to have a sizeable maximum in the downward mass flux at low-levels. This downward mass transport deficiency is due to the lack of a strong mesoscale downdraft within the SB volume of this young squall line. The stratiform-like volume observed by YH (Figs. 5.11i and 5.11j) has a similar low-

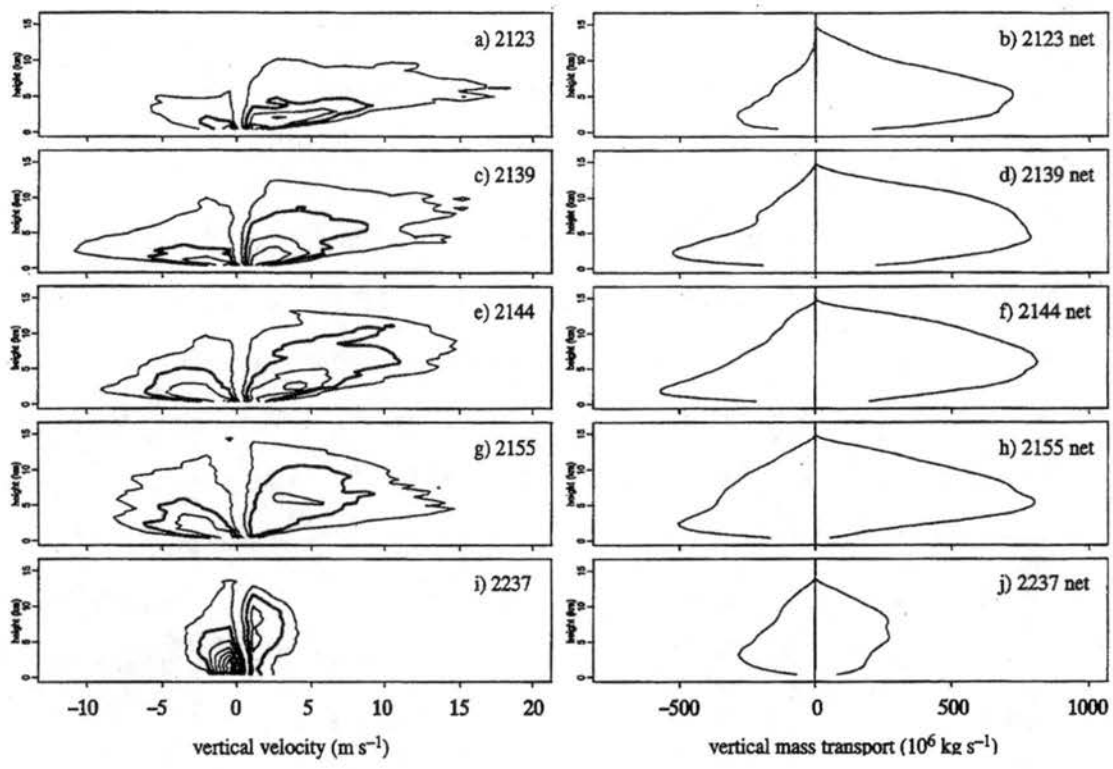

Figure 5.11: Time series of CFADs of vertical-mass-weighted CFADs of vertical velocity (left column) and net vertical mass transport upward and downward (right column) corresponding to five different dual-Doppler volume scans taken from Yuter and Houze (1995c). Vertical mass transport is contoured in the CFADs at 25×10^6 kg s^{-1} intervals and the $\pm 50 \times 10^6$ kg s^{-1} contours are highlighted. One-meter-per-second bins are used in the construction of the CFADs.

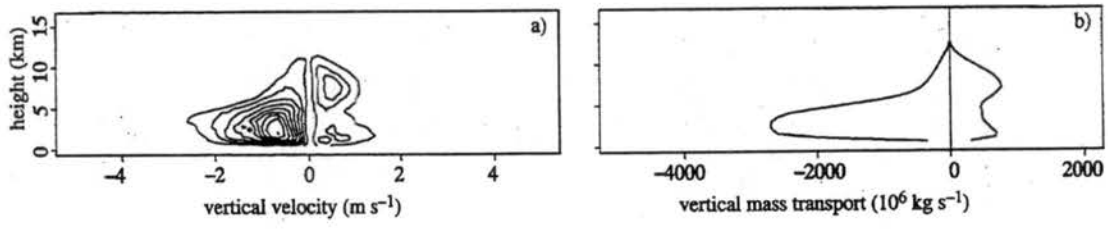

Figure 5.12: Vertical-mass-transport-weighted CFAD of vertical velocity (a) and the net vertical mass transport upward and downward from a stratiform volume behind a Kansas squall line at 0345 UTC 11 June 1985 during PRE-STORM. CFAD bin size for $w = 0.2$ m s^{-1}, contoured at 50×10^6 kg s^{-1} intervals (from Yuter and Houze 1995c).

level maximum in the downward mass flux associated with the downward vertical motions present.

5.5 Summary of the statistical view of the 7–8 May squall line

Mean vertical profiles of reflectivity and kinematic fields from the CL region of the 7–8 May squall line have been computed and found to compare favorably with similar statistics from previous convection studies. In contrast, the SB volume was shown to differ from many previously studied squall line SB regions. The major differences included: a weakened bright band structure, and a weak mesoscale downdraft. The mesoscale updraft was observed to be similar to that noted in previous studies.

Further insight into these two regions of this squall line was obtained through the use of CFADs. CFAD analyses revealed there to be much more variability in vertical motions in both the CL and SB than noted in previous studies. The mesoscale updraft/downdraft couplet observed in the SB was shown to be a residual of many smaller-scale updrafts and downdrafts.

The vertical mass transport statistics for the CL region showed that the majority of the mid-level mass transport (and therefore the condensation) was dominated by areas of intense upward motion. This finding is in disagreement with Yuter and Houze (1995c) who documented that most of the vertical mass transport occurred outside of strong updraft cores. Significant downward mass transport was also observed within the CL region.

Chapter 6

SUMMARY AND DISCUSSION

6.1 Summary

The 7–8 May squall line grossly exhibited many features similar to those observed in previous squall line studies. A leading line of convection, a transition zone, and a trailing secondary band of precipitation were part of the precipitation structure of this squall line. Descending rear-to-front flow and ascending front-to-rear flow predominated in the line-perpendicular flow, while strong along-line flow was observed throughout the squall line. Rearward of the transition zone, an intense along-line flow jet was noted. Along-line averaging of reduced-resolution data showed the convective line to contain a rearwardly tilted updraft, behind which the secondary band contained a mesoscale ($\sim$15 km wide) updraft/downdraft couplet. At low levels, precipitation-driven downdrafts were noted within the convective line.

It is on the fine scale that ELDORA has provided new insight into the inner workings of a maturing linear squall line. Within the convective line was a highly variable horizontal flow, with possible Bernoulli-type accelerations of the flow near deep convection. Also, accelerations in the lower- to midtroposphere line-perpendicular flow appeared to be related to the LeMone (1983) low to the rear of the convective line. Flow rearward of the convective line was much less perturbed. Within the secondary band, the jet-like feature in the along-line flow was possibly enhanced within a melting-induced stable layer.

The fine-scale analysis of convective-line vertical velocities revealed updrafts to be upright and centered at increasing elevations behind the leading edge of the line. The lower-resolution along-line compositing smoothed this complicated draft pattern into the tilted updraft structure noted earlier.

The vertical motion field within the secondary band comprised many small-scale updrafts and downdrafts at all levels. The mesoscale updraft/downdraft couplet depicted in the coarse view turned out to be the residual of these small-scale drafts.

Further analysis of the vertical velocity field within this squall line revealed high-frequency gravity wave oscillations. Evidence for these gravity waves came by way of an observed quadrature relationship between the vertical motion field and the perturbations of the line-perpendicular flow. This is the first observational corroboration of recent modeling studies in which high-frequency gravity waves were predicted (Fovell et al. 1992; Alexander et al. 1995; Yang and Houze 1995; Fovell and Tan 1998).

Complicating the gravity wave interpretation, though, was the three-dimensional nature of these features. Wave-fronts of vertical motion (oriented perpendicular to the midtropospheric system-relative flow) existed within both the convective line and the secondary band. These wave-fronts were similar to those observed in previous squall line studies (Smull and Houze 1987a; Keenan and Rutledge 1992; Bluestein et al. 1993) and may be due to a V-shaped pattern of gravity waves emanating from numerous cells in the convective line. Processes such as constructive and destructive interference and shear-related organization of these emanating gravity waves could have led to the observed wave-fronts of vertical motion.

From a statistical perspective, mean vertical profiles of reflectivity and kinematic fields from the convective line were similar to those from previous studies. In contrast, the secondary band volume profiles differed from those of many previously studied squall lines. The major differences included a weakened bright band and a weak mesoscale downdraft. The mesoscale updraft was similar to those noted in previous studies.

Contoured Frequency by Altitude Diagrams (CFADs) revealed a much wider range of vertical motions in the secondary band than that observed by previous studies. When compared to similarly resolved data within a subtropical stratiform region, a comparably wide range of vertical motions was observed, which supports the idea that these data resolved previously unresolvable intense kilometer-scale drafts within the secondary band.

Mass-weighting of the vertical velocity CFADs revealed that the majority of the midtropospheric mass transport was via areas of intense upward motion. This is in contrast to work by Yuter and Houze (1995c), in which they documented that weak to moderate updrafts were responsible for most of the upward mass transport within a line of Florida cumulonimbi. The work shown here suggests that the results obtained by Yuter and Houze may not be universally applicable. Environmental conditions (such as CAPE) were most likely the reasons for the difference in observed vertical mass fluxes.

The significant midtropospheric downward mass transport by downdrafts (roughly two-thirds of the upward mass transport) indicated that significant subsidence occurred close to the leading line of convection.

6.2 Future work

The most obvious limitation to this research is the temporally limited data of the features observed within this squall line. Even so, just one pass of high-resolution data taken through this squall line revealed many significant fine-scale, and previously unobserved, phenomena.

To better characterize gravity waves within squall lines, future modeling efforts should emphasize high-resolution three-dimensional squall line simulations. Future observational research should concentrate on both in situ and dual-Doppler observations for the study of these gravity waves. The ELDORA has shown that it is suited for such fine-scale observations.

Work currently is being done on the portion of the *Electra* flight that took place along the front side of the 7–8 May squall line. The author is examining the squall line's gust front, the formation of new cells, and the pre-squall environment. In addition, the line's initiation and evolution is also being studied by the author. As noted in Chapter 3, this squall line was dominated by supercell-type convection during the first three to four hours of its existence. It then became a multi-cellular dominated squall line. Details of this change in convective structure exists within ELDORA, NEXRAD, cloud-to-ground lightning, and mesonet data. However, due to time constraints, the author omitted from this paper these

other topics of study. The transition zone data (presented in this paper), along with the front-side and evolutionary data are all important to the understanding of the the 7–8 May squall line, and are the subject of future work.

REFERENCES

Alexander, M. J., J. R. Holton, and D. R. Durran, 1995: The gravity wave response above deep convection in a squall line simulation. *J. Atmos. Sci.*, **52**, 2212–2226.

Atlas, D., R. Tatehira, R. C. Srivastava, W. Marker, and R. E. Carbone, 1969: Precipitation-induced mesoscale wind perturbations in the melting layer. *Quart. J. Roy. Meteor. Soc.*, **95**, 544–560.

Augustine, J. A., and E. J. Zipser, 1987: The use of wind profilers in a mesoscale experiment. *Bull. Amer. Meteor. Soc.*, **68**, 4–14.

Austin, P. M., and A. Bemis, 1950: A quantitative study of the bright band in radar precipitation echoes. *J. Meteor.*, **7**, 165–171.

Battan, L. J., 1973: *Radar Observation of the Atmosphere.* University of Chicago Press, 324 pages.

Bélair, S., and D.-L. Zhang, 1996: A numerical study of the along-line variability of a frontal squall line during PRE-STORM. *Mon. Wea. Rev.*, **125**, 2544-2561.

Biggerstaff, M. I., and R. A. Houze, Jr., 1991a: Kinematic and precipitation structure of the 10–11 June 1985 squall line. *Mon. Wea. Rev.*, **119**, 3034–3065.

Biggerstaff, M. I., and R. A. Houze, Jr., 1993: Kinematics and microphysics of the transition zone of the 10–11 June 1985 squall line. *J. Atmos. Sci.*, **50**, 3091–3110.

Biggerstaff, M. I., and R. A. Houze, Jr., 1991b: Midlevel vorticity of the 10–11 June 1985 squall line. *Mon. Wea. Rev.*, **119**, 3066–3079.

Blackadar, A. K., 1957: Boundary layer wind maxima and their significance for the growth of nocturnal inversions. *Bull. Amer. Meteor. Soc.*, **38**, 283–290.

Bluestein, H. B., 1992: *Synoptic-Dynamic Meteorology in Midlatitudes. Volume 1: Principles of Kinematics and Dynamics.* Oxford University Press, New York, New York, 431 pages.

Bluestein, H. B., S. D. Hrebenach, and C. -F. Chong, 1993: Synthetic dual-Doppler analysis of mesoscale convective systems. *Mon. Wea. Rev.*, **122**, 2105–2124.

Bluestein, H. B., and M. H. Jain, 1985: Formation of mesoscale lines of precipitation: severe squall lines in Oklahoma during the spring. *J. Atmos. Sci.*, **42**, 1711–1732.

Brandes, E. A., 1990: Evolution and structure of the 6–7 May 1985 mesoscale convective system and associated vortex. *Mon. Wea. Rev.*, **118**, 109–127.

Braun, S. A., and R. A. Houze, Jr., 1994: The transition zone and secondary maximum of radar reflectivity behind a midlatitude squall line. *J. Atmos. Sci.*, **51**, 2733–2755.

Braun, S. A., and R. A. Houze, Jr., 1995: Melting and freezing in a mesoscale convective system. *Quart. J. Roy. Meteor. Soc.* **115**, 425–461.

Braun, S. A., and R. A. Houze, Jr., 1995: On the evolution of the 10–11 June PRE-STORM squall line: initiation, development of the rear inflow, and dissipation. *Mon. Wea. Rev.*, **125**, 478-504.

Bresch, J. F., 1994: Numerical simulation and analysis of a series mesoscale convective systems. Ph. D. Dissertation, Colorado State University, 286 pages.

Brock, F. D., and Coauthors, 1995: The Oklahoma mesonet: A technical overview. *J. Atmos. Oceanic Technol.*, **11**, 5–19.

Brown, H. A., 1963: On the low-level structure of a squall line. Mesometeorology Research Paper No. 21, University of Chicago, 19 pages.

Brown, J. M., 1979: Mesoscale unsaturated downdrafts driven by rainfall evaporation: a numerical study. *J. Atmos. Sci.*, **36**, 313–338.

Browning, K. A., 1977: The structure and mechanisms of hailstorms. *Hail: A Review of Hail Science and Hail Suppression*, G. B. Foote and C. A. Knight, Eds., American Meteorological Society, 1–43.

Browning, K. A., and R. Wexler, 1968: The determination of kinematic properties of a wind field using Doppler radar. *J. Appl. Meteor.*, **7**, 105–113.

Brunk, I. W., 1953: Squall lines. *Bull. Amer. Meteor. Soc.*, **34**, 1–9.

Buell, C. E., 1943: The determination of vertical velocities in thunderstorms. *Bull. Amer. Meteor. Soc.*, **24**, 94–95.

Byers, H. R., and R. R. Braham, 1949: *The Thunderstorm.* U. S. Department of Commerce, U. S. Weather Bureau, Washington, D. C., 287 pages.

Cotton, W. R., M. S. Lin, R. L. McAnelly, and C. J. Tremback, 1989: A composite model of mesoscale convective complexes. *Mon. Wea. Rev.*, **117**, 765–783.

Cram, J. M., R. A. Pielke, and W. R. Cotton, 1992: Numerical simulations and analysis of a prefrontal squall line. Part II: Propagation of the squall line as an internal gravity wave. *J. Atmos. Sci.*, **49**, 209–225.

Cressman, G. P., 1959: An operational objective analysis system. *Mon. Wea. Rev.*, **87**, 367-374.

Crum, T. D., and R. L. Alberty, 1993: The WSR-88D and the WSR-88D support facility. *Bull. Amer. Meteor. Soc.*, **74**, 1669–1687.

Cunning, J. B., 1986: The Oklahoma-Kansas Preliminary Regional Experiment for STORM Central. *Bull. Amer. Meteor. Soc.*, **67**, 1478–1486.

Das, P., 1964: Role of condensed water in the life cycle of a convective cloud. *J. Atmos. Sci.*, **21**, 404–418.

Foote, G. B., and P. S. du Toit, 1969: Terminal velocity of raindrops aloft. *J. Appl. Meteor.*, **8**, 249–253.

Foster D. S., 1958: Thunderstorm gust compared with computed downdraft speeds. *Mon. Wea. Rev.*, **89**, 91–94.

Fovell, R. G., D. Durran, and J. R. Holton 1992: Numerical simulations of convectively generated stratospheric waves. *J. Atmos. Sci.*, **49**, 1427–1442.

Fovell, R. G., and P. S. Dailey, 1995: The temporal behavior of numerically simulated multicell-type storms. Part I: Modes of behavior. *J. Atmos. Sci.*, **52**, 3144–3176.

Fovell, R. G., and Y. Ogura, 1988: Numerical simulation of a midlatitude squall line in two dimensions. *J. Atmos. Sci.*, **45**, 3846–3879.

Fovell, R. G., and P. -H. Tan, 1998: The temporal behavior of numerically simulated multicell-type storms. Part I: The convective cell life cycle and cell generation. *Mon. Wea. Rev.*, **126**, 551–577.

Fujita, T. T., 1955: Results of detailed synoptic studies of squall lines. *Tellus*, **7**, 405–436.

Fujita, T. T., 1959: Precipitation and cold air production in mesoscale thunderstorm systems. *J. Meteor.*, **16**, 454–466.

Fujita, T. T., 1963: Analytical mesometeorology: a review. *Meteor. Monographs*, **5**, 77–125.

Gallus, W. A., Jr., 1993: The dynamics of circulations within the stratiform regions of squall lines. Ph. D. Dissertation, Colorado State University, 290 pages.

Gallus, W. A., Jr., and R. H. Johnson, 1992: The momentum budget of an intense midlatitude squall line. *J. Atmos. Sci.*, **49**, 422–450.

Gallus, W. A., Jr., and R. H. Johnson, 1995a: The dynamics of circulations within the trailing stratiform regions of squall lines. Part I: The 10–11 June PRE-STORM System. *J. Atmos. Sci.*, **52**, 2161–2187.

Gallus, W. A., Jr., and R. H. Johnson, 1995b: The dynamics of circulations within the trailing stratiform regions of squall lines. Part II: Influence of the convective line and ambient environment. *J. Atmos. Sci.*, **52**, 2188–2211.

Gamache, J. F., and R. A. Houze, Jr., 1982: Mesoscale air motions associated with a tropical squall line. *Mon. Wea. Rev.*, **110**, 118–135.

Gao, K., D.-L. Zhang, M. W. Moncrieff, and H.-R. Cho, 1990: Mesoscale momentum budget in a midlatitude squall line: a numerical case study. *Mon. Wea. Rev.*, **118**, 1011–1028.

Gray, W. M., 1973: Cumulus convection and larger scale circulations: I. Broadscale and mesoscale considerations. *Mon. Wea. Rev.*, **101**, 839–855.

Hane, C. E., and D. P. Jorgensen, 1995: Dynamic aspects of a distinctly three-dimensional mesoscale convective system. *Mon. Wea. Rev.*, **121**, 3194–3214.

Harrold, T. W., and K. A. Browning, 1967: Mesoscale wind fluctuations below 1,500 meters. *Met. Mag.*, London, **96**, 367–376.

Heymsfield, G. M., and S. Schotz, 1985: Structure and evolution of a severe squall line over Oklahoma. *Mon. Wea. Rev.*, **113**, 1563–1589.

Hildebrand, P. H., C. A. Walther, C. L. Frush, J. Testud, and F. Baudin, 1994: The ELDORA/ASTRIA airborne Doppler weather radar. Goals, design, and first field tests. *Proc. IEEE*, **82**, 1873–1890.

Hildebrand, P. H., and Coauthors, 1996: The The ELDORA/ASTRIA airborne Doppler weather radar: High resolution observations from TOGA COARE. *Bull. Amer. Meteor. Soc.*, **77**, 213–232.

Hobbs, P. V., and J. D. Locatelli, 1978: Rainbands, precipitation cores, and generating cells in a cyclonic storm. *J. Atmos. Sci.*, **35**, 230–241.

Holle, R. L., A. I. Watson, R. Ortiz, and R. E. Lopez, 1990: Spatial patterns of lightning, radar echoes, and severe weather in mesoscale convective systems. Preprints, *16th Conf. on Severe Local Storms*, Kananaskis, Alberta, Amer. Meteor. Soc., 721-726.

Houze, R. A., Jr., 1977: Structure and dynamics of a tropical squall-line system observed during GATE. *Mon. Wea. Rev.*, **105**, 1540–1567.

Houze, R. A., Jr., 1989: Observed structure of mesoscale convective systems and implication for large-scale heating. *Quart. J. Roy. Meteor. Soc.* **115**, 425–461.

Houze, R. A., Jr., 1993: *Cloud Dynamics*. Academic Press, San Diego, California, 573 pages.

Houze, R. A., Jr., 1997: Stratiform precipitation in regions of convection: A meteorological paradox? *Bull. Amer. Meteor. Soc.*, **78**, 2179–2196.

Houze, R. A., Jr., and E. N. Rappaport, 1984: Air motions and precipitation structure of an early summer squall line over the eastern tropical Atlantic. *J. Atmos. Sci.*, **41**, 553-574.

Houze, R. A., Jr., S. A. Rutledge, M. I. Biggerstaff, and B. F. Smull, 1988: Interpretation of Doppler weather radar displays of midlatitude mesoscale convective systems. *Bull. Amer. Meteor. Soc.*, **70**, 608–619.

Houze, R. A., Jr., B. F. Smull, and P. Dodge, 1990: Mesoscale organization of springtime rainstorms in Oklahoma. *Mon. Wea. Rev.*, **118**, 613–654.

Johnson, R. H., 1976: The role of convective-scale precipitation downdrafts in cumulus and synoptic-scale interactions. *J. Atmos. Sci.*, **33**, 1890–1910.

Johnson, R. H., 1993: Midlatitude convective systems. Notes for NCAR Colloquium on *Clouds and Climate.* 41 pages.

Johnson, R. H., 1993: Dynamical effects of mesoscale convective systems. Notes for *International Workshop on Mesoscale Meteorology and TAMEX Program Review*, Taiwan, 8 pages.

Johnson, R. H., and D. L. Bartels, 1992: Circulations associated with a mature-to-decaying midlatitude mesoscale convective system. Part II: Upper-level features. *Mon. Wea. Rev.*, **120**, 1201–1320.

Johnson, R. H., and P. J. Hamilton, 1988: The relationship of surface pressure features to the precipitation and airflow structure of an intense midlatitude squall line. *Mon. Wea. Rev.*, **116**, 1444–1472.

Johnson, R. H., and D. C. Kriete 1982: Thermodynamic and circulation characteristics of winter monsoon tropical mesoscale convection *Mon. Wea. Rev.*, **110**, 1898–1911.

Johnson, R. H., and B. D. Miner, 1994: Interacting flows between mesoscale convective systems along a cold front. *Mon. Wea. Rev.*, **123**, 585–599.

Johnson, R. H., and M. E. Nicholls, 1983: A composite analysis of the boundary layer accompanying a tropical squall line. *Mon. Wea. Rev.*, **111**, 308–319.

Joss, J., and D. Waldvogel, 1970: Raindrop size distribution and Doppler velocities. Preprints, *24th Conf. on Radar Meteor.*, Tucson, AZ, Amer. Meteor. Soc., 153–156.

Keenan, T. D., and S. A. Rutledge, 1992: Mesoscale characteristics of monsoonal convection and associated stratiform precipitation. *Mon. Wea. Rev.*, **121**, 352–374.

Kessinger, C. J., P. S. Ray, and C. E. Hane, 1987: The 19 May 1977 Oklahoma squall line. Part I: A multiple Doppler analysis of convective and stratiform structure. *J. Atmos. Sci.*, **44**, 2840–2864.

Kingsmill, D. E., and R. M. Wakimoto, 1991: Kinematic, dynamic and thermodynamic analysis of a weakly sheared severe thunderstorm over northern Alabama. *Mon. Wea. Rev.*, **119**, 262–297.

Klimowski, B. A., 1994: Initiation and development of rear inflow within the 28–29 June 1989 North Dakota mesoconvective system. *Mon. Wea. Rev.*, **122**, 765–779.

Klemp, J. B., and R. B. Wilhelmson, 1978: The simulation of three-dimensional convective storm dynamics. *J. Atmos. Sci.*, **35**, 1070–1096.

Knupp, K. R., 1987: Downdrafts within high plains cumulonimbi: Part I: General kinematic structure. *J. Atmos. Sci.*, **44**, 987–1008.

Knupp, K. R., and W. R. Cotton, 1987: Internal structure of a small mesoscale convective system. *Mon. Wea. Rev.*, **115**, 629–645.

Lafore, J.-P., and M. W. Moncrieff, 1989: A numerical investigation of the organization and interaction of the convective and stratiform regions of tropical squall lines. *J. Atmos. Sci.*, **46**, 521–544.

Larsen, M. F., W. E. Swartz, and R. F. Woodman, 1982: Gravity-wave generation by thunderstorms observed with a vertically-pointing 403 MHz radar. *Geophys. Res. Lett.* **9**, 571–574.

Leary, C. A., and R. A. Houze, Jr., 1979: Melting and evaporation of hydrometeors in precipitation from the anvil clouds of deep tropical convection. *J. Atmos. Sci.*, **36**, 669–679.

Leary, C. A., and E. N. Rappaport, 1987: The life cycle and internal structure of a mesoscale convective complex. *Mon. Wea. Rev.*, **115**, 1503–1527.

Lee, W. -C., and R. M. Wakimoto, 1997: Fine scale structure of a squall line observed by the NCAR ELDORA and NOAA P-3 during Vortex-95. Preprints, *28th Conf. on Radar Meteor.*, Austin, TX, Amer. Meteor. Soc., 520–521.

Leise, J. A., 1982: A multidimensional scale-telescoped filter and data extension package. NOAA Tech. Memo. ERL WPL-82, 19 pages. [Available from NOAA ERL, 325 Broadway, Boulder, Colorado, 80303.]

LeMone, M. A., 1983: Momentum transport by a line of cumulonimbus [sic]. *J. Atmos. Sci.*, **40**, 1815–1834.

LeMone, M. A., G. M. Barnes, and E. J. Zipser, 1984: Momentum flux by lines of cumulonimbus [sic] over the tropical oceans. *J. Atmos. Sci.*, **41**, 1914–1932.

LeMone, M. A., and M. W. Moncrieff 1993: Momentum transport by convective bands: Comparisons of highly idealized dynamic models to observations. *Meteor. Monographs*, **24**, 75–92.

Levine, J., 1942: The effect of vertical accelerations of pressure during thunderstorms. *Bull. Amer. Meteor. Soc.*, **23**, 52–61.

Ligda, M. G. H., 1951: Radar storm observations. In *Compendium of Meteorology*. American Meteorological Society, Boston, Massachusetts, 1265–1282.

Ligda, M. G. H., 1956: The radar observations of mature prefrontal squall lines in the midwestern United States. *VI Congress of Organisation Scientifique et Technique Internationale du Vol a Voile (OSTIV)*, Aeronautical International Federation, St-Yan, France, 1–3.

Lin, Y. -L., and S. Li, 1988: Three-dimensional response of a shear flow to elevated heating. *J. Atmos. Sci.*, **45**, 2987–3002.

Loehrer, S. M., 1992: The surface pressure features and precipitation structure of PRE-STORM mesoscale convective systems. M. S. Thesis, Colorado State University, 296 pages.

Loehrer, S. M., and R. H. Johnson, 1995: Surface pressure and precipitation life cycle characteristics of PRE-STORM mesoscale convective systems. *Mon. Wea. Rev.*, **123**, 600–621.

Maddox, R. A., 1980: Mesoscale convective complexes. *Bull. Amer. Meteor. Soc.*, **61**, 1374–1387.

Malkus, J. S., and R. S. Scorer, 1955: The erosion of cumulus towers. *J. Meteor.*, **12**, 43–57.

Mapes, B. E., 1993: Gregarious tropical convection. *J. Atmos. Sci.*, **50**, 2026–2037.

Mapes, B. E., and R. A. Houze, Jr., 1995: Diabatic divergence profiles in Western Pacific mesoscale convective systems. *J. Atmos. Sci.*, **52**, 1807–1828.

Marwitz, J., and J. Toth, 1993: The Front Range blizzard of 1990. Part II: Melting effects in a convective band. *Mon. Wea. Rev.*, **124**, 2469–2482.

Matejka, T., and T. J. Schuur, 1991: The relation between vertical air motions and the precipitation band in the stratiform region of a squall line. Preprints, *25th Conf. on Radar Meteor.*, Paris, France, Amer. Meteor. Soc., 501–504.

McAnelly, R. L., and W. R. Cotton, 1986: Meso-β-scale characteristics of an episode of meso-α-scale convective complexes. *Mon. Wea. Rev.*, **114**, 1740–1770.

McAnelly, R. L., and W. R. Cotton, 1989: The precipitation life cycle of mesoscale convective complexes over the Central United States. *Mon. Wea. Rev.*, **117**, 784–808.

McAnelly, R. L., and W. R. Cotton, 1992: Early growth of mesoscale convective complexes: a meso-β-scale cycle of convective precipitation? *Mon. Wea. Rev.*, **120**, 1851–1877.

McFarlane, N. A., 1987: The effect of orographically excited gravity wave drag on the general circulation of the lower stratosphere and troposphere. *J. Atmos. Sci.*, **44**, 1775–1800.

Meitín, J. G., and J. B. Cunning, 1985: The Oklahoma-Kansas preliminary regional experiment for STORM-Central (OK PRE-STORM), Volume I. Daily operations summary. NOAA Tech. Memo. ERL ESG-20, Dept. of Commerce, Weather Research Program, Boulder, Colorado, 313 pages.

Mohr, C. G., L. J. Miller, R. L. Vaughn, and H. W. Frank, 1986: The merger of mesoscale datasets into a common Cartesian format for efficient and systematic analysis. *J. Atmos. Oceanic Technol.*, **3**, 143–161.

Moncrieff, M. W., and M. J. Miller, 1976: The dynamics and simulation of tropical cumulonimbus [sic] and squall lines. *Quart. J. Roy. Meteor. Soc.*, **102**, 373–394.

Nachamkin, J. E., 1992: The upscale evolution of a midlatitude mesoscale convective complex. M. S. Thesis, Colorado State University, 122 pages.

Nachamkin, J. E., 1998: Observational and numerical analysis of the genesis of a mesoscale convective system. Ph. D. Dissertation, Colorado State University, 219 pages.

Newton, C. W., 1950: Structure and mechanism of the pre-frontal squall line. *J. Meteor.*, **7**, 210–222.

Newton, C. W., 1966: Circulations in large sheared cumulonimbus [sic]. *Tellus*, **18**, 699-712.

Nicholls, M. E., 1987: A comparison of the results of a two-dimensional numerical simulation of a tropical squall line with observations. *Mon. Wea. Rev.*, **115**, 3055–3077.

Nicholls, M. E., R. H. Johnson, and W. R. Cotton, 1988: The sensitivity of two-dimensional simulations of tropical squall lines to environmental profiles. *J. Atmos. Sci.*, **45**, 3625–3649.

Ogura, Y., and M. T. Liou, 1980: The structure of the midlatitude squall line: a case study. *J. Atmos. Sci.*, **37**, 553–567.

Ooyama, K., 1971: A theory on the parameterization of cumulous convection. *J. Meteorol. Soc. Japan.* **56 (special issue)**, 744–756.

Orlanski, I., 1975: A rational subdivision of scales for atmospheric processes. *Bull. Amer. Meteor. Soc.*, **56**, 527–530.

Orville, R. E., R. W. Henderson, and L. F. Bosart, 1988: Bipole patterns revealed by lightning locations in mesoscale storm systems. *Geophys. Res. Lett.*, **15**, 129–132.

Oye, R., 1988: REORDER: A program for gridding radar data. NCAR Field Observing Facility, Boulder, CO, 15 pages. [Available from NCAR, P. O. Box 3000, Boulder, Colorado 80307.]

Oye, R., and R. E. Carbone, 1981: Interactive Doppler editing software. Preprints, *20th Conf. on Radar Meteor.*, Boston, MA Amer. Meteor. Soc., 683–689.

Oye, R., C. Mueller, and S. Smith, 1995: Software for radar translation, visualization, editing, and interpolation. Preprints, *24th Conf. on Radar Meteor.*, Vail, CO, Amer. Meteor. Soc., 359–361.

Palmer, T. N., G. J. Shutts, and R. Swinbank, 1986: Alleviation of a systematic westerly bias in general circulation and weather prediction models through an orographic gravity wave drag parameterization. *Quart. J. Roy. Meteor. Soc.*, **112**, 1869–1884.

Pandya, R.E., and D.R. Durran, 1996: The influence of generated thermal forcing on the mesoscale circulation around squall lines. *J. Atmos. Sci.*, **53**, 2924-2951.

Pedgley, D. E., 1962: A meso-synoptic analysis of the thunderstorms on 28 August 1958. Brit. Meteor. Off. Geophys. Mem. No. 106, 74 pages.

Pfister, L., 1986: Small-scale motions observed by aircraft in the lower stratosphere: Evidence for mixing and its relation to large-scale flows. *J. Atmos. Sci.*, **43**, 3210–3225.

Pfister, L., S. Scott, M. Loewenstein, S. Bowen, and M. Legg, 1993: Mesoscale disturbances in the tropical stratosphere excited by convection: Observations and effects on the stratosphere momentum budget. *J. Atmos. Sci.*, **50**, 1058–1075.

Ralph, F. M., M. Crochet, S. V. Venkateswaran, 1993: Observations of a mesoscale ducted gravity wave. *J. Atmos. Sci.*, **50**, 3277-3291.

Ralph, F. M., P. J. Neiman, D. W. van de Kamp, and D. C. Law. 1995: Using spectral moment data from NOAA's 404-MHz radar wind profilers to observe precipitation. *Bull. Amer. Meteor. Soc.*, **76**, 1717–1739.

Rasmussen, E. N., J. M. Straka, R. Davies-Jones, C. A. Doswell, III, F. H. Carr, M. D. Eilts, and D. R. MacGorman, 1994: Verification of the Origins of Rotation in Tornadoes Experiment: VORTEX. *Bull. Amer. Meteor. Soc.*, **75**, 995–1006.

Raymond, D. J., R. Solomon, and A. M. Blyth, 1991: Mass fluxes in New Mexico mountain thunderstorms from radar and aircraft measurements. *Quart. J. Roy. Meteor. Soc.*, **117**, 587–621.

Redelsperger, J.-L., and J.-P. Lafore, 1988: A three-dimensional simulations of a tropical squall line: convective organization and thermodynamic transport. *J. Atmos. Sci.*, **45**, 1334–1356.

Riehl, H., 1968: Some aspects of cumulus-scale downdrafts. Atmospheric Science Paper No. 126, Part 1, Colorado State University, 32 pages.

Rind, D., R. Suozzo, N. K. Balachandran, A. Lacis, and G. Russel, 1988: The GISS global climate–middle atmosphere model. Part I: Model structure and climatology. *J. Atmos. Sci.*, **45**, 329–370.

Rotunno, R., J. B. Klemp, 1982: Influence of the shear-induced pressure gradient on thunderstorm motion. *Mon. Wea. Rev.*, **110**, 136–151.

Rotunno, R., J. B. Klemp, and M. L. Weisman, 1988: A theory for strong, long-lived squall lines. *J. Atmos. Sci.*, **45**, 463–485.

Roux, F., 1988: The West African squall line observed on 23 June 1981 during COPT 81: kinematics and thermodynamics of the convective region. *J. Atmos. Sci.*, **44**, 406–426.

Roux, F., J. Testud, M. Payen, and B. Pinty, 1984: West African squall line thermodynamic structure retrieved from dual-Doppler radar observations. *J. Atmos. Sci.*, **41**, 3104–3120.

Rutledge, S. A., and R. A. Houze, Jr., 1987: A diagnostic modeling study of the trailing stratiform region of a midlatitude squall line. *J. Atmos. Sci.*, **44**, 2640–2656.

Rutledge, S. A., D. R. MacGorman, 1988: Cloud-to-ground lightning activity in the 10-11 June 1985 mesoscale convective system observed during the Oklahoma-Kansas PRE-STORM Project. *Mon. Wea. Rev.*, **116**, 1393–1408.

Rutledge, S. A., R. A. Houze, Jr., M. I. Biggerstaff, and T. Matejka, 1988: The Oklahoma-Kansas mesoscale convective system of 10-11 June 1985: precipitation structure and single-Doppler radar analysis. *Mon. Wea. Rev.*, **116**, 1409–1430.

Rutledge, S. A., and D. R. MacGorman, 1988: Cloud-to-ground lightning activity in the 10-11 June 1985 mesoscale convective system observed during OK PRE-STORM. *Mon. Wea. Rev.*, **116**, 1393–1408.

Rutledge, S. A., L. Chungu, and D. R. MacGorman, 1990: Positive cloud-to-ground lightning in mesoscale convective systems. *J. Atmos. Sci.*, **47**, 2085–2100.

Rutledge, S. A., and W. A. Petersen, 1994: Vertical radar reflectivity structure and cloud-to-ground lightning in the stratiform region of MCSs: Further evidence for in-situ charging in the stratiform region. *Mon. Wea. Rev.*, **122**, 1760–1776.

Sanders, F., and K. A. Emanuel, 1977: The momentum budget and temporal evolution of a mesoscale convective system. *J. Atmos. Sci.*, **34**, 322–330.

Sato, K., 1993: Small-scale wind disturbances observed by the MU radar during the passage of Typhoon Kelly. *J. Atmos. Sci.*, **50**, 518–537.

Sawyer, J. S., 1946: Cooling by rain as the cause of the pressure rise in convective squalls. *Quart. J. Roy. Meteor. Soc.*, **72**, 168.

Schmidt, J. M., and W. R. Cotton, 1990: Interactions between upper and lower tropospheric gravity waves on squall line structure and maintenance. *J. Atmos. Sci.*, **47**, 1205–1222.

Schubert, W. H., P. E. Ciesielski, C. Lu, and R. H./ Johnson, 1995: Dynamical adjustment of the trade wind inversion layer. *J. Atmos. Sci.*, **52**, 2941–2952.

Schuur, T. J., 1997: An observational study of mesoscale convective system electrification. Ph. D. Dissertation, Colorado State University, 301 pages.

Schuur, T. J., B. F. Smull, W. D. Rust, and T. C. Marshall, 1991: Electrical and Kinematic structure of the trailing stratiform region trailing an Oklahoma squall line. *J. Atmos. Sci.*, **48**, 825–841.

Scott, J. D., and S. A. Rutledge, 1995: Doppler radar observations of an asymmetric MCS and associated vortex couplet. *Mon. Wea. Rev.*, in press.

Skamarock, W. C., M. L. Weisman, and J. B. Klemp, 1994: Three-dimensional evolution of simulated long-lived squall lines. *J. Atmos. Sci.*, **51**, 2563–2584.

Smull, B. F., and J. A. Augustine, 1993: Multiscale analysis of a mature mesoscale convective complex. *Mon. Wea. Rev.*, **121**, 103–132.

Smull, B. F., and R. A. Houze, Jr., 1985: A midlatitude squall line with a trailing region of stratiform rain: radar and satellite observations. *Mon. Wea. Rev.*, **113**, 117–133.

Smull, B. F., and R. A. Houze, Jr., 1987a: Dual-Doppler radar analysis of a midlatitude squall line with a trailing region of stratiform rain. *J. Atmos. Sci.*, **44**, 2128–2148.

Smull, B. F., and R. A. Houze, Jr., 1987b: Rear inflow in squall lines with trailing stratiform precipitation. *Mon. Wea. Rev.*, **115**, 2869–2889.

Srivastava, R. C., T. J. Matejka, and T. J. Lorello, 1986: Doppler radar study of the trailing anvil region associated with a squall line. *J. Atmos. Sci.*, **43**, 356–377.

Stewart, R. E., J. D. Marwitz, J. C. Pace, and R. E. Carbone, 1984: Characteristics through the melting layer of stratiform clouds. *J. Atmos. Sci.*, **41**, 3227–3237.

Stensrud, D. J., R. A. Maddox, and C. L. Ziegler, 1991: A sublimation-initiated mesoscale downdraft and its relation to the wind field below a precipitating anvil cloud. *Mon. Wea. Rev.*, **119**, 2124–2139.

Stolzenburg, M., 1994: Observations of high ground flash densities of positive lightning in summertime thunderstorms. *Mon. Wea. Rev.*, **122**, 1740-1750.

Szeto, K. K., R. E. Stewart, and C. A. Lin, 1988a: Mesoscale circulations forced by melting snow. Part I: Basic simulations and dynamics. *J. Atmos. Sci.*, **45**, 1629–1641.

Szeto, K. K., R. E. Stewart, and C. A. Lin, 1988b: Mesoscale circulations forced by melting snow. Part II: Application to meteorological features. *J. Atmos. Sci.*, **45**, 1642–1650.

Takahashi, M., and B. A. Bolville, 1992: A three-dimensional simulation of the equatorial quasi-biennial oscillation. *J. Atmos. Sci.*, **49**, 1020–1035.

Thorpe, A. J., M. J. Miller, and M. W. Moncrieff, 1982: Two-dimensional convection in non-constant shear: A model of midlatitude squall lines. *Quart. J. Roy. Meteor. Soc.*, **108**, 739–762.

Tripoli, G., and W. R. Cotton, 1989a: A numerical study of an observed orogenic mesoscale convective system. Part I. Simulated genesis and comparison with observations. *Mon. Wea. Rev.*, **117**, 273–304.

Tripoli, G., and W. R. Cotton, 1989b: A numerical study of an observed orogenic mesoscale convective system. Part II. Analysis and governing dynamics. *Mon. Wea. Rev.*, **117**, 305–328.

Wakimoto, R. M., 1982: The life cycle of thunderstorm gust fronts viewed with Doppler radar and rawinsonde data. *Mon. Wea. Rev.*, **110**, 1060–1082.

Wakimoto, R. M., W. -C. Lee., H. B. Bluestein, C. -H. Liu, and P. H. Hildebrand, 1996: ELDORA observations during VORTEX 95 *Bull. Amer. Meteor. Soc.*, **77**, 1465–1481.

Webster, P., and R, Lukas, 1992: TOGA COARE: The Coupled Ocean-Atmosphere Response Experiment. *Bull. Amer. Meteor. Soc.*, **73**, 1377–1416.

Weisman, M. L., 1992: The role of convectively generated rear-inflow jets in the evolution of long-lived mesoconvective systems. *J. Atmos. Sci.*, **49**, 1826–1847.

Weisman, M. L., J. B. Klemp., and R. Rotunno, 1988: Structure and evolution of numerically simulated squall lines. *J. Atmos. Sci.*, **45**, 1990–2012.

Xue, M., K. K. Droegenmeier, V. Wong, A. Shapiro, and K. Brewster, 1995: ARPS version 4.0 user's guide. Center for Analysis and Prediction of Storms, Univ. of Oklahoma, 380 pages. [Available from CAPS, 100 E. Boyed st., Norman, OK 73019.]

Yang, M.J., and R. A. Houze, Jr., 1995: Multicell squall-line structure as a manifestation of vertically trapped gravity waves. *Mon. Wea. Rev.*, **123**, 641–660.

Yuter, S. E., and R. A. Houze, Jr., 1995a: Three-dimensional kinematic and microphysical evolution if Florida cumulonimbus. Part I: Spatial distribution of updrafts, downdrafts, and precipitation. *Mon. Wea. Rev.*, **123**, 1921–1940.

Yuter, S. E., and R. A. Houze, Jr., 1995b: Three-dimensional kinematic and microphysical evolution if Florida cumulonimbus. Part II: Frequency distributions of vertical velocity, reflectivity, and differential reflectivity. *Mon. Wea. Rev.*, **123**, 1941–1963.

Yuter, S. E., and R. A. Houze, Jr., 1995c: Three-dimensional kinematic and microphysical evolution if Florida cumulonimbus. Part III: Vertical mass transport, mass divergence, and synthesis. *Mon. Wea. Rev.*, **123**, 1964–1983.

Yuter, S. E., and R. A. Houze, Jr., 1997: Measurements of raindrop size distributions over the Pacific warm pool and implications for Z-R relations. *J. Appl. Meteor.*, **36**, 847–867.

Zhang, D.L., and K. Gao, 1989: Numerical simulation of an intense squall line during 10–11 June 1985 PRE-STORM. Part II: Rear inflow, surface pressure perturbations, and stratiform precipitation. *Mon. Wea. Rev.*, **117**, 2067–2094.

Zhang, D.L., and K. Gao, and D. B. Parsons, 1989: Numerical simulation of an intense squall line during 10–11 June 1985 PRE-STORM. Part I: Model verification. *Mon. Wea. Rev.*, **117**, 960–994.

Zipser, E. J., 1969: The role of organized unsaturated convective downdrafts in the structure and rapid decay of an equatorial disturbance. *J. Appl. Meteor.*, **8**, 799–814.

Zipser, E. J., 1977: Mesoscale and convective scale downdrafts as distinct components of squall-line structure. *Mon. Wea. Rev.*, **105**, 1568–1589.

Zipser, E. J., 1982: Use of a conceptual model of the life cycle of mesoscale convective systems to improve very-short-range forecasts. *Nowcasting*, K. Browning, Ed., Academic Press, San Diego, California, pages 191–204.